Advanced Current-limiting Control of Inverter-interfaced Distributed Energy Resources to Develop Self-Protected Microgrids

by

Alexandros G. Paspatis

Thesis submitted in partial fulfillment of the requirements for the Doctor of Philosophy degree

The University of Sheffield

Faculty of Engineering

Department of Automatic Control and Systems Engineering

August 2020

To my family

Acknowledgments

First of all, I would like to thank my supervisor Dr. George Konstantopoulos for giving me the opportunity to study at this leading institution and for the supervision and his efforts during the last four years. Under his lead, I managed to push myself to the limits and deepen my knowledge. Apart from the academic support, his words at times of struggle encouraged me and kept me on track. I would also like to thank my second supervisor Prof. Martin Mayfield for the mentoring and the advice that he has given me throughout my PhD studies. Also, a big "thank you" to my fellow group members Andrei, Shlomo, Seyfullah, Pablo, Fernando, Grigoris and Panos for their friendship and support.

This thesis would not have been completed without the endless support of my family. Words can not describe how grateful I am to my parents Grigoris and Suzana for always being by my side and keeping me strong. Furthermore, a big "thank you" to my sister Michaela, who accompanied me in this 4-year period in UK and motivated me with her commitment to her goals.

Last but not least, a warm "thank you" to my friends in UK and those back in Crete. Especially to those in Crete, who never stopped caring and always made me feel like we are together, despite the thousands of miles between us.

A "thank you" would not be enough for Nora, for her unconditional love and support, which made the completion of this thesis possible.

Finally, as this challenging academic journey comes to the end, let me quote those words from Nikos Kazantzakis:

"If they were to ask me what road leads to heaven, I would answer them: the most difficult!"

Abstract

In the upcoming "smart grid" era, advanced control schemes are required for inverter-interfaced DERs to guarantee stability of inverter-dominated feeders and microgrids. Nevertheless, in many of the recently proposed methods, the safe and stable operation of inverters can not be analytically guaranteed under normal and abnormal grid conditions.

In this thesis, single-phase grid-connected inverters are initially considered and an enhanced Current-Limiting Droop (CLD) controller is proposed. In contrast to the original CLD, which limits the inverter current under a lower value than its maximum during faults, the proposed controller fully utilizes the inverter capacity. An inherent current limitation is proven through nonlinear ultimate boundedness theory and is shown to facilitate the operation of Fault-Ride-Through (FRT) schemes. Furthermore, conditions for asymptotic stability of the closed-loop system are derived. Additionally, a new CLD scheme is proposed, which operates without the need of a PLL and introduces a virtual inertia property to DERs. In the sequel, three-phase grid-connected inverters are investigated and a new controller in the dq-frame is proposed to deal with FRT in three-phase systems. Initially, a novel method to divide the current into its symmetrical components during unbalanced faults is proposed. Hence, based on an adaptive bounded integral controller, the proposed scheme provides voltage support to both positive and negative sequences, while ensuring the current boundedness and asymptotic stability of the closed-loop system. In the final part of this thesis, the safe and stable operation of three-phase inverter-based microgrids is investigated. Particularly, an advanced controller is proposed to deal with extreme load conditions. Through the proposed scheme, the limitation of the inverter current during transients is guaranteed, without the need of online adaptation techniques. Furthermore, the proposed approach significantly simplifies the stability analysis of microgrids, since it can be investigated through a Jacobian matrix of reduced size.

Validation methods: The proposed controllers are verified through extended simulation, real-time simulation and experimental results.

Keywords: Nonlinear control systems, Power systems analysis, Stability analysis, Inverters, Distributed energy resources, Microgrids, Power system dynamics, Grid faults.

Contents

List of Figures

List of Tables

1 Introduction

Renewable energy sources (RESs) have evolved into a crucial component of power systems. From the theoretical aspects, RESs are a highly desired energy source since they are environmental friendly. In particular, photovoltaic systems, wind turbines, tidal energy systems and other RESs help in decreasing the share of power production from fossil fuels and decarbonize the power sector, which is one of the biggest CO_2 emitters globally at the moment. From a technical point of view, RESs represent today the majority of distributed energy resources (DERs) connected to power grids. For decades, renewable energy sources were being used for electrical power production, however, their capacities were insignificant compared to the coal, gas and the nuclear power plants. As the years went by, a need for more electrical energy production from RESs came up due to their aforementioned environmental advantages, while certain targets were set regarding their utilization around the world. European 2020 package was a significant action of the EU leaders in 2007, that targeted to achieve by 2020, a 20% (or even 30%) reduction in CO_2 emissions compared to the 1990 levels, a 20% of the consumed energy to be coming from RESs and a 20% increase in energy efficiency. Similar targets are now under agreement in the EU energy strategies for 2030 and 2050.

Power systems structure has undergone significant changes over the years. In particular, the apparatus and the adopted technologies have faced a continuous transformation over the years to deal with different requirements and raised issues. However, the fact that "changed the paradigm" in the power system structure and operation, is the massive interconnection of DERs, which either consist from RESs connected to the grid through power electronics devices (i.e. inverters) or from synchronous machine-based units, such as hydroelectric plants. When the DERs penetration level was raised significantly at the transmission and distribution levels, power flow changed from unidirectional (which was the case under the conventional centralized generation topology) to bidirectional. Moreover, the inverter-interfaced DERs exhibit a different dynamic behavior than that of synchronous generators. As a result, a need for new control and protection approaches came up while eventually, a totally different operation principle will be required to locally exploit the capabilities of DERs. The power grid that would host a high capacity of distributed energy resources to increase the renewable energy sources utilization and that would further ensure a smart, reliable, safe and economical operation, would be called the "smart grid." Among other advancements, this smartness also refers to the smart grid's ability to act on its own under variations in the grid conditions or during grid faults. Hence, the control philosophy of the smart grid becomes a crucial aspect. This au-

tonomy in decisions, in combination with the local utilization of DERs, is believed to be a solution to some of the technical issues that arise from the high penetration of DERs, from the dynamic behavior of inverter-interfaced DERs or from the new technologies that are getting connected to the grid (e.g. electric vehicles and energy storage devices). In the same context, with the increased power production from DERs, the microgrid structure was also proposed to locally utilize the DERs capabilities in a more reliable way. Specifically, the local production and consumption of electric power is expected to help in hosting higher capacities of DERs and in achieving a more reliable, efficient and economical operation of the power system, since microgrids are able to operate either connected to the main (smart) power grid or in the islanded mode. Therefore, a microgrid corresponds to the structural unit of the smart grid, which can continue operating normally when faults appear in the upstream network. Since the smart grid and microgrid concepts are pretty broad at the moment, a direct transformation from the current power system structure to the smart grid is not possible, but gradually all the new technologies and infrastructure aim to this concept.

In the context of control of power generation units, the schemes that are used today for the synchronous generators are considered advanced enough to deal with most of the disturbances that may come up in power systems, even in the case of distributed synchronous generators of low power rating. On the other hand, a vast amount of the DERs interconnected to the power grid are RESs which interfere with the grid through power electronic devices. However, the massive integration of these inverter-interfaced units raises issues such as fluctuations in the grid voltage and the limitation of the system's inertia, due to the dynamics of the power electronic devices. Hence, significant restrictions apply today to the grid integration of inverter-interfaced DERs and in order to overcome some of these limitations, advanced control systems are required for the inverter devices of those DER units. Among other tasks, there is a need for advanced control schemes that can accomplish the proportional power sharing between inverter-interfaced DERs and the load voltage and frequency regulation, while ensuring the protection of the inverter equipment during transients and the stability of the power system. This particular PhD thesis aims to tackle the aforementioned challenge.

1.1 Aim, Objectives and Potential Impact

The aim of this thesis is to develop novel control methods to be applied to the inverters of inverter-interfaced DERs. Firstly, the grid-connected operation of inverter-interfaced DERs will be taken into consideration and then, the challenging concept of inverter-based microgrids will be investigated as well. The proposed controllers should be capable to operate in the same (unified) structure under both normal and abnormal grid conditions. Furthermore, the proposed control schemes will desirably provide an assured stability to the plant, while the relevant modeling and analysis

will be mathematically shown.

The objectives, needed, to meet the stated aim are:

• Obtain the mathematical model of the inverter-interfaced DERs and the rest of the power components under consideration.

• Develop advanced control schemes based on the upon stated models in order to meet the requirements coming out from the Grid Codes and in order for the control systems to become more reliable and simpler to implement.

• Mathematically, ensure the safe and stable operation under normal and abnormal grid conditions.

• Test the proposed controllers in order to validate their operation.

Validation methods: The controller verification can be performed through i) numerical simulation results, using well-known software environments, ii) real-time simulation results, which employ a digital simulator to test the system under consideration under the real-world clock rate and iii) hardware experimental results, using power electronics laboratory setups.

Potential impact of this thesis to the scientific community: Nowadays, the large-scale utilization of DERs cannot be achieved due to technical and safety concerns. Hence, the share of renewable energy in energy consumption ranges today from 10% to 40%, in most of the countries. It is a common belief but not fully proven yet, that with the development of advanced control methods for the power inverters interfering with the grid, the large-scale utilization of distributed energy resources can be addressed and therefore larger amounts of electric power coming from RESs can be utilized, paving the way to zero carbon emissions power networks. This offers advantages in terms of sustainability, a better environmental outcome and in practice, the set energy targets by each state to be met. Inherent current limitation, voltage support under grid faults, virtual inertia introduction, self-synchronization capability, communication-less safe inverter operation in microgrids are tasks that if completed and implemented in unified control schemes, the safety and operation issues discussed above could be overcome and thus, the control system of inverters could significantly contribute in the transition to the smart grid.

1.2 Thesis organization

The rest of this thesis is organized as follows: In chapter 2, a literature review of the research topic of this thesis is presented. The required background knowledge is highlighted and the state-of-the-art research is being critically discussed. In chapter 3, important theorems and stability tools utilized throughout this thesis are presented. In chapter 4, the case of single-phase grid-connected inverters is considered. Advanced control schemes are proposed to guarantee the safe and stable

operation of the grid-connected inverter-interfaced DERs, while their response under grid faults is also tackled, according to the recent Grid Code requirements. In chapter 5, three-phase grid-connected inverter applications are taken into consideration. In particular, their safe and stable operation under grid faults is investigated. Focus is especially given in the unbalanced grid faults case, where advanced schemes are required to deal with voltage support in both positive and negative symmetrical component sequences. In chapter 6, the operation of inverter-based microgrids is investigated. Advanced control schemes that guarantee the proportional power sharing and at the same time ensure an inherent inverter current limitation are proposed, while the stability of the entire microgrid is also assessed. In chapter 7, the derived conclusions from this thesis are outlined and future work directions are given. In the Appendix, supplementary analysis and proofs are presented, while the list of publications is given in the end of the thesis.

2 Literature review

2.1 Interfacing DERs to the power grid

The majority of the distributed energy resources (DERs) require power electronic devices for their connection to the grid [1], as depicted in Fig. 2.1. This is due to the fact, that nearly all of the renewable energy sources (RESs) units require power inverters to interfere with the grid. At the same time, the grid operators impose certain requirements for the connection of those DER units to the power system. These requirements are most of the times defined in each country's Grid Code and continuously get updated as the share of DERs is increasing [2]. Apart from the requirements that focus on the operation of DERs under normal grid conditions, methodologies regarding how these units should respond to grid faults (or other emergency conditions) are also given from the operators. A vast amount of these ancillary services, can be satisfied from the DERs through the appropriate design of the inverter control system and this is the reason that power inverters' control is researched - among other topics- from both power and control engineers in order to establish a "smart" future power system, also named as a "smart grid". Hence, concurrently with the modern grid requirements and technologies that pave the way to the smart grid era, the inverters should accomplish specific tasks in order to switch to their smart era as well. In this context, the "smart inverter" concept is introduced based on the features of: self-awareness (e.g. monitoring, diagnostics, fail-safe), adaptability (e.g. self-tuning, fault-tolerant), autonomy (e.g. load sharing, limited communication), cooperativeness (e.g. optimization, stability enhancement) and plug-and-play techniques (e.g. operate without technical configuration) [3].

2.2 Grid Code requirements for DERs

2.2.1 Low and zero inertia power networks

The interconnection of DERs to the power grid is performed under specific guidelines, given from the grid operators. With every new guideline release, new control techniques may appear as a recommended or required practice for DERs. Instructions are given regarding the desired response of DERs, not only in each country's Grid Code [2], but also in the ENTSO-E guidelines for the European supergrid [4]. Moreover, specific ancillary services are usually required from the DERs, under

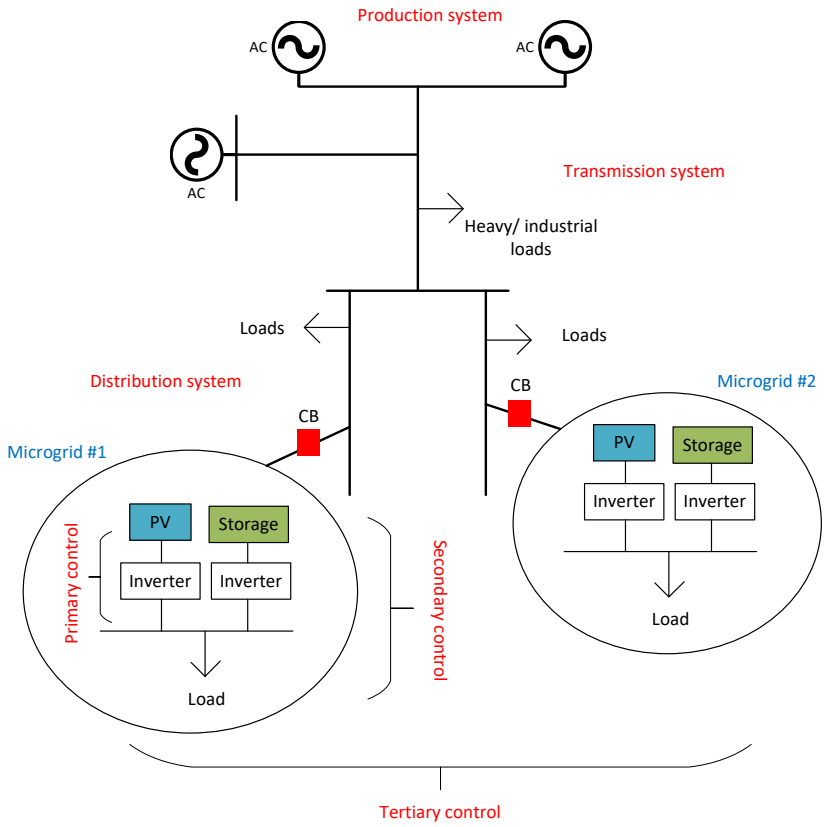

Figure 2.1: Transition of the power system into its "smart" era

abnormal grid conditions. The main reason that these instructions and required services continuously get updated nowadays, is the "paradigm shift" that power systems face due to the increasing penetration of DERs. In particular, the massive interconnection of DERs at the distribution system allowed bidirectional power flow at the feeders, while due to the dynamic response of inverter-interfaced DERs, the inertia constant started getting limited [5, 6]. However, this lack of inertia may lead to undesirable events during transients. To highlight this trend, National Grid in United Kingdom has presented a diagram, depicted in Fig. 2.2, that predicts how system's inertia will be limited in the following years [7]. Hence, new control and protection techniques are required for power networks with increased share of inverter-interfaced DERs [8].

In the special scenario of inverter-dominated systems which arise in the case of feeders where inverter-interfaced DERs supply a critical part of the the load (feeders with high penetration level) or in the case of islanded microgrids without synchronous machine-based DERs, the zero inertia may lead to catastrophic events. Soon enough, it is expected that new requirements will come up regarding low and zero inertia power networks. As a matter of fact, an IEEE task force is at the moment active and investigates this issue [9]. In light of these concerns, the relaxation

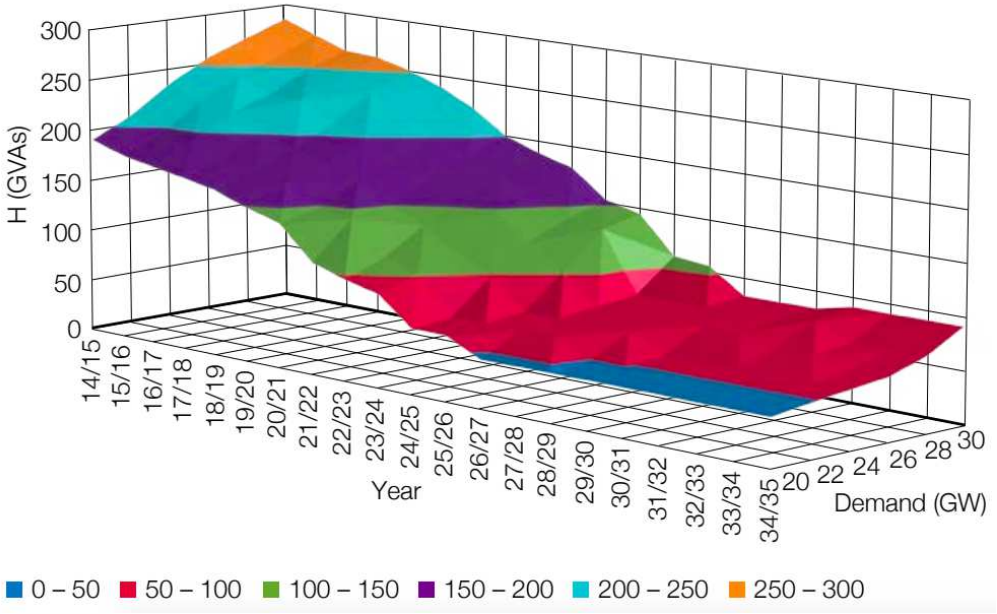

Figure 2.2: Inertia estimation by National Grid [7]

of the Grid Code requirements, the use of stand-by synchronous generators to provide inertia and the virtual inertia provision by inverter-interfaced DERs have been proposed [10, 11]. Regarding the latter case, control techniques have been proposed to virtually introduce inertia to the DER units, through the inverter control system [12, 13, 14, 15, 16]. In practice, these techniques govern the frequency response of DERs, thus mimicking the inertia constant of synchronous machines. Nevertheless, most of the renewable DERs do not have a rotating mass to inject or absorb (store) energy during transients. To tackle this issue, solutions have been proposed based on supercapacitors at the inverter DC link [17, 18]. The virtual inertia introduction through the control system of inverter-interfaced DERs has shown satisfactory preliminary results and it represents a possible requirement of the future Grid Codes.

As it was already mentioned, different techniques have been proposed to inherit a virtual inertia property to DER units through their control system. However, limited research has focused on how virtual inertia should be placed in the power grid. In [19], the problem of optimal placement of virtual inertia in power systems is investigated and a solution based on an optimization problem is proposed. The results of the proposed optimal placement method are highlighted through a case study that considers a three-region power system. Another study that addresses the same problem can be found in [20], where initially the grid is modeled through the swing equations and then, for the optimal placement of virtual inertia, inertia and damping at each node are optimized such that the frequency transient behavior is acceptable. It should be highlighted that one of the conclusions in [19], is that the resilience of the power system mostly depends on the location of the possible

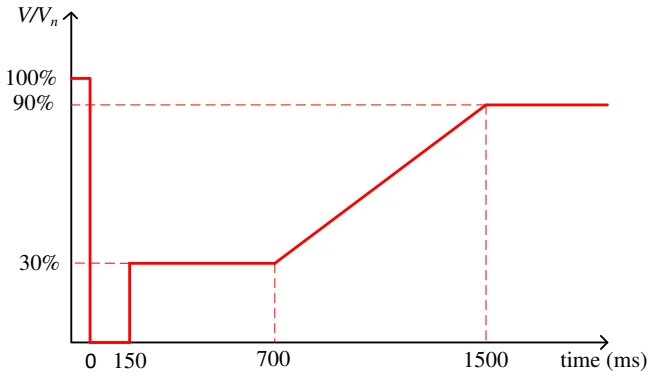

Figure 2.3: FRT Curve

disturbance and the inertia placement in the grid, rather than the total inertia of the system. The latter result may be of great interest for the future Grid Codes.

2.2.2 Operation under voltage drops

One of the most recent Grid Code requirements for DERs, is the Fault-Ride-Through (FRT) scheme. According to the FRT scheme, DERs should remain connected to the grid and support the point of common coupling (PCC) voltage, when grid faults occur. The idea behind this scheme lies on the fact that with the increased share of DERs, the power system could be benefited through ancillary services that the DERs can provide. Moreover, since the DERs nowadays supply a critical share of the load of power networks, disconnections during minor grid faults would reduce the reliability of the power system. From the technical point of view, this requirement usually consists of voltage/ time tripping curves that both synchronous machine-based DERs and inverter-interfaced DERs should follow. As an example, the desired operation under faulty grid conditions, according to the German BDEW curve [2], is depicted in Fig. 2.3. One can notice in this figure that when the voltage at the PCC is greater than 0.9 p.u., each DER should continue its normal operation. However, under more severe voltage drops, a minimum time during which the DER should remain connected to the grid is defined. During this time period, each DER should supply reactive power to support the grid voltage, based on the predominantly inductive nature of the power system lines. The amount of reactive power to be injected, most of the times, depends on the voltage drop. As an example, in [21], it is stated that the reactive current component i_q is selected as

$$i_q = k\Delta V, \tag{2.1}$$

where k is defined as the FRT gain and ΔV is the PCC voltage drop. Even if each Grid Code usually defines exactly how the DERs should operate during faults, from the control perspective, different FRT schemes that aim to optimize the voltage support operation have been proposed in the literature. Furthermore, even though

the original FRT scheme was proposed for faults in the transmission system, recent applications of FRT schemes have emphasized on faults in the distribution system as well [22]. The application of FRT schemes during voltage drops, is also met in the literature as the Low-Voltage-Ride-Through (LVRT) scheme [22, 23].

A significant number of lately published works, has proposed different control schemes with FRT capability for inverter-interfaced DERs. In [24], a control scheme to support PCC voltages during grid faults is presented. This technique has the ability to determine the amount of reactive power that needs to be injected in order for the faulty voltages to be lifted inside an acceptable range, according to the Grid Codes. This work though is limited to symmetric faults and this is the reason that in [25], the same controller is redesigned such that to define the reactive power injection through positive and negative sequence components control, to extend its application to asymmetric and time varying grid faults. Experimental results verified the operation of both control schemes. In [26], the FRT gain k, shown in Eq. (2.1), is investigated for its impact to the inverter operation during grid faults. Moreover, a technique that injects reactive power during grid faults according to the German FRT requirement and concurrently reduces the real power to avoid overloading, is proposed. Then, it is highlighted that a new kind of instability (namely "current angle instability") occurs due to the difference between the angle of the reference current and the angle of the output impedance, which can lead to loss of synchronization. This instability stresses the system when severe voltage drops occur, close to the PCC of each DER. In order to analyze this kind of instability, some assumptions are made; specifically, i) the consideration of the PCC voltage to be equal to the voltage drop at the inverter output impedance and ii) the consideration of the DER as a current source converter due to the fast inner current controller. As a solution to this instability, the locking of the synchronization unit under severe voltage drops is proposed. In [27], an adaptive control technique is proposed, which utilizes an online gain tuning during disturbances to familiarize grid-connected photovoltaic systems with the Low-Voltage-Ride-Through requirement. Finally, in [28], a LVRT control technique is proposed that ensures the full exploitation of the power capabilities of a photovoltaic DER, when voltage drops occur. The proposed scheme is based on modifying the current reference values, to inject real and reactive power to the grid through positive and negative sequence components control, in a way that fully utilizes the plant capabilities for the LVRT. Hence, through this control scheme, two objectives are fulfilled during voltage sags: i) maximum available current is injected independently of the voltage sag magnitude, ii) real power oscillations are avoided. However, the employed current-limiting technique is based on limiting the reference current values, i.e. the current limitation is ensured only at the steady state. Note that for every FRT or LVRT technique, the considered current-limiting technique is of crucial importance and hence, it will be extensively investigated in the sequel. Furthermore, it should be highlighted that most of the control schemes that deal with FRT techniques, do not investigate the operation during normal grid conditions. Nevertheless, the control system of inverters in power systems with high

share of DERs should be capable to operate in a unified way under both normal and abnormal grid conditions, while ancillary services may be required from the DERs during the normal grid operation as well. Finally, the closed-loop system stability is rarely investigated under the control schemes with FRT capability.

As it is clear in the previous review, research regarding the response of inverter-interfaced DERs during grid faults, is not limited to balanced faults. Thus, when negative sequence components come up in the power system, the control system should act in way that ensures the safe inverter operation and the grid support provision. In this context, different control objectives are met in the literature:

1) Avoiding the power oscillations that occur from the interaction of positive and negative sequence components, as in [28, 29]

2) Provision of balanced current and hence, only positive sequence power injection to the grid, as in [30, 31]

3) Provision of voltage support through increasing positive sequence voltage and reducing negative sequence voltage, as in [32, 33].

Regarding the 3rd objective, recently, guidelines for negative sequence voltage reduction have been proposed [34]. The wider concept of adopting voltage support schemes for both the positive sequence voltage (FRT & LVRT) and the negative sequence voltage, is commonly denoted as the "voltage support concept" [35]. This constitutes in DERs supporting (increasing) the positive sequence voltage and eliminating (decreasing) the negative sequence voltage, which comes up when unbalanced grid faults occur. Nevertheless, this concept has an increased complexity regarding the required current-limiting technique, as it will be discussed in the sequel.

As it can be understood from this section, the desired response of inverter-interfaced DERs during transients can be guaranteed through advanced control schemes. Similarly, the response of inverters during normal grid conditions can be optimized through their control system. Finally, it should be noted that inverter-interfaced DERs correspond to the majority of DER devices and this is the reason that this thesis focuses on the control of inverter-interfaced DERs, to enable large scale utilization of DERs and RESs. Hence, in the sequel, a thorough review of control schemes of inverter-interfaced DERs will be presented, both for the grid-connected mode and the islanded microgrid operation.

2.3 Control of grid-connected inverter-interfaced DERs

As it is stated in [36], the fundamental requirements for a power system are "i) to uninterruptedly feed the loads with the required powers, ii) to feed the loads in the minimum cost and with minimum environmental impact and iii) to follow certain guidelines regarding the quality of the power supply." In order to meet

these requirements, different control techniques in more than one control levels are used today for the bulky generation units, while methodologies for optimizing the operation of the generation system are still under research. Similarly, in the context of inverter-interfaced DERs, the control system can guarantee the safe and reliable operation of inverter-dominated power networks. In [37], a review is presented regarding control schemes that have been proposed for grid-connected inverters. The main differences between these control schemes arise from the adopted control technique, the reference frame transformation (which will be discussed later), the feedback loops used (single or cascaded), the output filter design and the modulation method used. In the end, the major characteristics of each control system under investigation are listed on a table.

The control techniques applied to the large synchronous generators are nowadays considered well established, since their operation is based on the governor and automatic voltage regulator (AVR) devices [36]. Apart from optimizing the operation during normal grid conditions, the settings of these devices can also define the transient response of the synchronous generators under any faults in the power grid. On the one hand, by assuming that the large synchronous generators are able to guarantee power system stability (in terms of voltage and frequency regulation), control of inverter-interfaced DERs has been based for years on current-controlled inverters, using PI or PR controllers. In these control schemes, the current references are generated such that the maximum available power of the prime mover is injected to the grid and that the DC bus voltage is kept inside its limits. Based on this technique, the concept of grid-following inverters was defined. However, since recently the share of DERs has vastly increased, power system stability can not be governed solely from the bulky synchronous generators [16]. Inspired by the electromechanical characteristics of the synchronous generators and the corresponding governor and AVR-based control techniques, there is a trend in inverter-interfaced DERs control, to mimic the response of the synchronous generators through sophisticated power controllers. In this context, the droop controller [38], the virtual synchronous generator (VSG) [39], the synchronverter [16], the virtual synchronous machine (VISMA) [40] and the synchronous power control (SPC) [41] concepts have been proposed among others to mimic the synchronous generator response, both in the steady state and during transients. The common property of all these techniques, is the inclusion of the droop control characteristics for the voltage and frequency regulation. The droop control concept mimics the behavior of the governor and the AVR of the synchronous generators, by modifying the power injection such that to regulate the voltage and the frequency close to their set points. The VSG is actually the combination of the droop control technique and virtual inertia introduction in the control system. The synchronverter, apart from the virtual inertia, virtually introduces the friction coefficient and the field and mutual inductances in order to faithfully mimic the dynamic behavior of a synchronous generator. The SPC introduces into the inverter operation both the electrical and the mechanical characteristics of synchronous generators and on top of that, it manages to overcome some of the limitations of synchronous

generators. In these cases, the droop-controlled inverter-interfaced DERs are not classified any more as grid-following, but as grid-forming units, since they take part in the regulation of the load voltage and frequency. It should be highlighted that the above methodologies are met both in grid-connected and in islanded microgrid applications. However, more challenging control tasks are met in the islanded inverter-based microgrid operation and this is why control in microgrids is going to be reviewed separately in the sequel.

The aforementioned advanced grid-forming droop-based control schemes correspond to the power controller part of the inverter control scheme. Apart from the droop-based schemes, PQ regulation control (it can be met as $PQ-$set control as well) or unity power factor control (where $Q = 0$) are commonly adopted at the power control stage as well. Note that when the power controller adopts the PQ-set or unity power factor control schemes, the inverter is classified as grid-following while when the power is regulated according to droop control schemes, the inverter is classified as grid-forming, as it was already mentioned. Since grid-forming controllers are expected to pave the way towards large-scale utilization of inverter-interfaced DERs, a variety of enhanced grid-forming power control schemes have been proposed in the literature. The majority of the proposed techniques aim to enhance the functionalities of the inverter and to optimize the DER behavior under different grid conditions. As an example, in [42], the impact of grid fluctuations to the the power flow in a grid-connected inverter is analyzed. Then, an enhanced droop control scheme is proposed which mitigates the power flow control issues, by feed-forwarding the grid voltage and frequency into the droop control law. Finally, the proposed control scheme is further modified to guarantee closed-loop system stability.

The appropriate control technique to be used each time, depends on the characteristics of the setup under investigation and the ancillary services that are required from the inverter-interfaced DER. Even if the grid-following single-loop current control structure [25] is widely used today in real-world grid-connected inverter-interfaced DER applications, multi-loop controllers [6] have gained popularity due to the raised stability concerns in the upcoming smart grid era [8]. These multi-loop schemes have extra capabilities such as voltage regulation and smooth synchronization, while they can adopt both grid-forming and grid-following power control schemes. In order to better understand the structure of a typical multi-loop (cascaded) controller used for grid-connected inverters, the most commonly used units will be summarized in the sequel.

Common controller units for grid-connected inverter-interfaced DERs:

• Phase Locked Loop: The phase locked loop (PLL) unit is used to measure the frequency and the angle at the PCC of the inverter-interfaced DER and it is usually required for the safe synchronization of the inverter with the grid.

• Power Calculation block: The power calculation block uses the current and voltage measurements to calculate the output real and reactive powers. These calculations are required for the power controller operation.

• Power Controller: The power control stage is usually the slowest control action (has the lowest bandwidth) and performs the real and reactive power regulation according to a variety of different methods (e.g. grid-forming droop control or grid-following reference power regulation control), through PI controllers or statically.

• Virtual inductance/ resistance: In some cases, a virtual inductance or resistance may be introduced at the power controller stage to accomplish different tasks such as current limitation [43] or output impedance shaping [1].

• Voltage Controller: The voltage controller regulates through PI or PR controllers the inverter output voltage to a reference value which is usually defined by the power controller. A better power quality is guaranteed with the voltage controller while pre-synchronization issues are coordinated through this control loop as well [1].

• Current Controller: The inner current control loop is usually the fastest loop (has the highest bandwidth) and regulates through PI or PR controllers the inverter current to its reference value, which is usually defined by the voltage controller. In cases where the inverter parameters are accurately known and there are no uncertainties, a P controller may be enough for the inverter current regulation. However, in realistic systems, uncertainties are commonly present and that is why PI and PR controllers are usually preferred. The current controller significantly enhances the quality of the output current [1].

• PWM Generator: The PWM generator is the final stage of the controller and transforms the desired inverter voltage into the required pulses to control the inverter semiconductor switches.

The typical multi-loop control structure for grid-connected inverter-interfaced DERs is depicted in Fig. 2.4.

Note that as discussed in [15], power controllers with inherited synchronization and voltage regulation capabilities, have been proposed to replace the cascaded controller structure [30, 44, 45]. Furthermore, according to the requirements of each application, a variety of other units may also be introduced in the control system, e.g. saturation units to limit reference values of voltage or current, communication channels for the implementation of hierarchical control structures or switches to switch between different controllers [46, 47]. Moreover, in three-phase inverters, a useful technique that simplifies the control implementation and the controller analysis is the adoption of reference frame transformations [48, 49]. Instead of the natural reference frame (NF or *abc* frame), the stationary reference frame (SF or $\alpha\beta$ frame) and the synchronous reference frame (SRF or dq frame) are commonly employed. The $\alpha\beta$ frame transforms a three-phase sinusoidal signal into a new frame with two sinusoidal components, thus simplifying the control design, while the dq synchronous reference frame, utilizes a rotational transformation, which translates a three-phase sinusoidal signal into DC components (at the steady state) and hence, enables the use of traditional integral control schemes. Thus, reference frame transformation blocks may also be met in the control implementation.

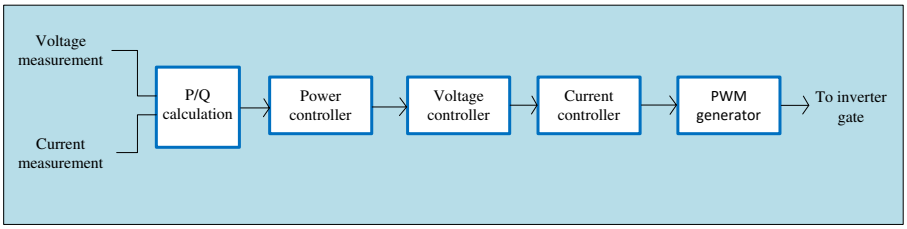

Figure 2.4: Typical structure of the control system of inverter-interfaced DERs

Finally, it should be noted that the described controller structure is subject to improvements, such as:

• Removing the PLL: Research is conducted on how the PLL can be removed from the controller since it is inherently nonlinear and moreover, the inverter performance may be degraded from oscillations at the measured frequency, due to possible DC offsets in the PLL input. In response to this issue, self-synchronization techniques have been proposed for grid-connected inverters [15, 43, 50].

• Avoiding the integrator wind-up phenomenon: Another issue, commonly discussed in the literature, is the integrator wind-up that may occur when saturation units are placed in the output of integral controllers (IC) in order to bound the control input of the plant [51]. Specifically, when the output of the controller is saturated, the controller is actually getting deactivated and this can lead to undesired performance or instability [52]. In response to this issue, a number of works have introduced anti-windup techniques [51, 53, 54]. However, the only approach that has managed to implement the IEEE anti-windup PI control model for dynamic analysis of power systems, is the one in [55]. Lately, the proposed in [56] bounded integral controller (BIC) is shown to be able to replace the traditional integral controller, while ensuring the control state boundedness and closed-loop system asymptotic stability. This work is supplemented by [57], where an enhanced version of the BIC is proposed to mimic more adequately the operation of the traditional IC while ensuring a bounded output and to de-stress the assumptions made in the original BIC about the initial values of the controller states.

The above description and discussion offers a general design approach for the control system of grid-connected inverter-interfaced DERs. Even if the same structure (with the corresponding challenges) is often used in microgrids, the control design for inverter-interfaced DERs in islanded microgrids is a more challenging task and thus, it will be separately reviewed. Furthermore, due to their popularity both in grid-connected and in microgrid applications, droop-controlled inverters will be also separately reviewed in the sequel.

2.4 Control of inverter-based microgrids

In the absence of grid connection, the power produced from DERs needs to match the requested load power. In the same context, the control of standalone DERs can not follow current control techniques as in the case of DERs connected to stiff grids, but has been based for years on voltage control schemes, where the load voltage is regulated to its nominal value. Nevertheless, with the increased integration of DERs, the formation of microgrids which host multiple DERs, raised new issues regarding the control system design, like the requirements for proportional power sharing and network voltage/frequency regulation.

A microgrid is a "small scale" power system that hosts production and consumption units, while it has the ability to operate either connected to the main grid or as an island. As stated in [58], the difference between a microgrid and a distribution system feeder with DERs, is the control philosophy. A microgrid can be considered as a part of the grid that is independently controlled. This does not hold for any feeder hosting DERs since each feeder can not necessarily operate in islanded mode. The microgrid concept was originally presented in [59], as the future power system structural unit. In the same work, the first concepts about the microgrid control system, protection system and energy management techniques, were briefly proposed. Nowadays, nearly two decades after those first concepts, advanced control techniques have been proposed for microgrids which vary between centralized or decentralized schemes and between primary or multilevel control systems (similarly to the conventional power system control levels structure), according to the required reliability and ancillary services for each application. Moreover, since inverter-interfaced DERs correspond to the vast majority of grid-connected DERs, the inverter-based microgrid concept has attracted a lot of attention [6].

A significant challenge under the islanded inverter-based microgrid configuration, is how the inverter-interfaced DERs will share the load proportionally to their ratings, in order to ensure an efficient operation and increase the devices lifetime. This challenge combined with the need for load voltage and frequency regulation restricts the primary control of inverter-interfaced DERs in islanded inverter-based microgrids to grid-forming control techniques. Droop control is the most widely used primary control technique in microgrids, due to its ability to regulate the load voltage and frequency and at the same time share the power according to the capacity of each inverter, without requiring any communication links [6, 38, 60]. Apart from droop control, other primary grid-forming control schemes have also been proposed for microgrids, like the virtual oscillator control [61, 62]. Nevertheless, droop control remains the most widely used technique in microgrids [63, 64], either by directly being applied to inverter-interfaced DERs in its conventional form [6] or by utilizing the advanced droop control schemes that were discussed in the previous section [16, 39, 65].

For a long time, different control levels have been utilized for the proper power system operation, i.e. hierarchical control structures with primary, secondary and

tertiary levels. Likewise, hierarchical control structures have been proposed for inverter-based microgrids as well. In [8], the primary, secondary and tertiary control levels of microgrids are classified. The primary control level of grid-forming inverters aims to stabilize voltage and frequency, as it was previously discussed, while it does not require any communication links, since it acts in a decentralized manner based on the local inverter measurements. However, it usually introduces an error in the voltage and frequency regulation and the power sharing is accurate only when the p.u. output impedance of every inverter is the same [1]. Hence, aiming to address optimization issues, the local primary control is not enough and a need for higher control levels comes up. Regarding the higher control levels, the secondary control level aims at restoring the microgrid voltage and frequency to their rated values and furthermore, at restoring the proportional power sharing between inverter-interfaced DERs. Then, the tertiary control level is used to optimize the power flow and the operation cost between interconnected microgrids or between a microgrid and the main grid [66]. A typical hierarchical control structure consisting of primary, secondary and tertiary levels is depicted in Fig. 2.5. In [66], a complete framework of hierarchical control of inverter-based microgrids is proposed. Specifically, primary, secondary and tertiary controllers are presented and the proposed scheme is verified experimentally. However, a centralized secondary control scheme is proposed, while power sharing restoration is not considered. It should be highlighted that distributed secondary control schemes are more reliable than centralized schemes, which have a single point of failure and require more communication links. To face these issues, the reactive power sharing restoration is performed through a distributed controller in [67]. In [68], the effect of the voltage and frequency restoration to the restoration of the real and reactive power sharing is analyzed and a distributed controller is proposed to guarantee voltage and frequency restoration and proportional power sharing, simultaneously. A review is performed in [69], where the recently proposed primary decentralized control schemes and their stability analysis are presented. Furthermore, microgrid hierarchical control techniques are presented. It is noteworthy that since the higher control levels require communication links which may fail for various reasons, every inverter in a microgrid should always be capable to operate only with its primary grid-forming controller, as a backup solution.

Another crucial challenge in control of microgrids, is to ensure that a microgrid can smoothly connect and disconnect to the main grid, when this is required [8]. This transition between the grid-connected and the islanded modes usually requires information which is not available locally (e.g. the grid frequency and the grid phase sequence). Thus, the appropriate control action is commonly performed through the secondary or the tertiary control level. In [70], the droop control law is modified during the synchronization process, such that to achieve a smooth connection to the grid, by utilizing a distributed control scheme. A similar technique is presented in [71], where seamless transition is achieved by modifying the droop control law, using a central controller that transmits the grid voltage measurements to each unit. In [44], a droop-like universal primary controller that has the ability to seamlessly

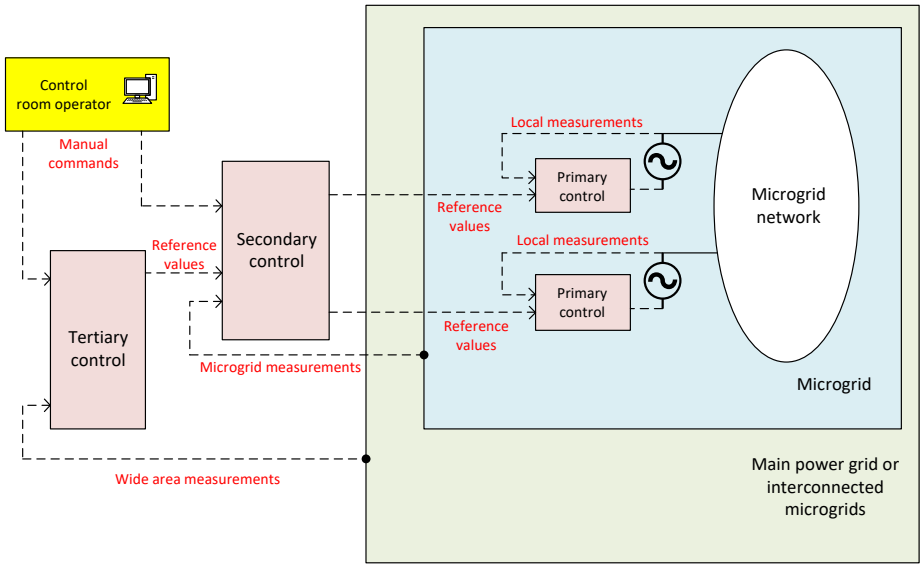

Figure 2.5: Different control levels of microgrids

transit between the two operation modes is proposed. The control scheme in [44] can guarantee voltage and frequency regulation when in islanded mode and control the real and reactive power injection when in grid-connected mode. This controller is modified in [72] to be applied to three-phase inverters, while in [30], it is redesigned so that it can follow the FRT guidelines during unbalanced grid faults.

2.5 Droop Control of inverter-interfaced DERs

As it was highlighted in sec. 2.4, droop control is the most widely used primary control method in microgrids, while as it was discussed in sec. 2.3, the droop control technique is useful in the case of grid-connected inverters as well, due to its voltage and frequency regulation property. Hence, the droop control technique will be analytically discussed in this section.

Droop-controlled inverters operating in parallel were firstly investigated in [38]. In [38], real and reactive power sharing between two inverters was achieved through the droop control technique, without using any communication links. Nowadays, droop controllers are considered for most of the inverter-interfaced DERs which integrate renewable energy sources and distributed storage devices to inverter-dominated networks. Note that even if most of the inverter-interfaced DERs have a renewable energy source as a prime mover, energy storage devices have the ability to take part in voltage and frequency regulation too and thus, droop control is commonly utilized for these devices as well.

Droop control offers many advantages both in the grid-connected and in the islanded modes of operation of inverter-interfaced DERs. In an islanded microgrid scenario,

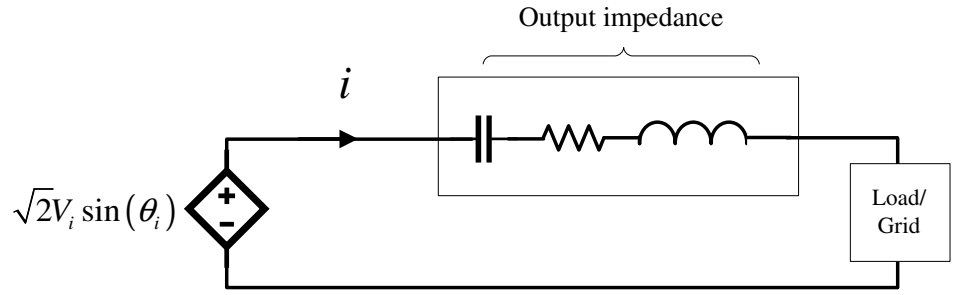

Figure 2.6: Output impedance between a voltage source and the load

droop-controlled inverters are able to regulate the load voltage and frequency close to their rated values and share the load according to the DERs capacities, by controlling two values - the angular frequency and the voltage magnitude. The proportional power sharing capability is subject to errors due to inaccuracies in the output impedance of each inverter. In fact, only when the p.u. output impedance of each inverter in a microgrid is the same, accurate real and reactive power sharing will be achieved [1]. Apart from its benefits in the islanded mode of operation, droop control is beneficial in the grid-connected mode as well, since it enhances the inverters with the ability to regulate the injected power according to the grid voltage and frequency. This ability is of great importance in feeders with high penetration level of inverter-interfaced DERs, since if all the units of a feeder were injecting the maximum available power and did not take part in the voltage and frequency regulation, overvoltage phenomena could arise and the DERs could eventually trip. Nevertheless, as in [63, 73], droop control is more widely used by inverters in islanded microgrids, while for grid-connected inverters, the power regulation through current controllers is the most common approach in the industry today.

To better understand the droop control operation, the nature of the output impedance needs to be introduced. The output impedance refers to the impedance between the PCC of each generation unit and the load, as shown in Fig. 2.6. Traditionally, the transmission system of power networks possesses an inductive impedance due to the long transmission lines. Furthermore, the heavy transformers in the output of the power plants make the impedance nature even more inductive. This inductive nature of the power system lines introduces the $P \sim \omega$ and $Q \backsim V$ relations, i.e. real power is mainly related to the frequency of the grid and reactive power mainly relates to the grid voltage [1, 66]. The operation of the AVR and the governor devices (that control the behavior of synchronous machines) is based on the aforementioned relations. In a similar manner, by assuming an inductive output impedance for the inverter-interfaced DERs, the conventional droop control is also defined based on the $P \sim \omega$ and $Q \backsim V$ relations [6, 38]. These droop functions are defined by the Grid Code [74] and CERTS [75], and should be followed by DERs that take part

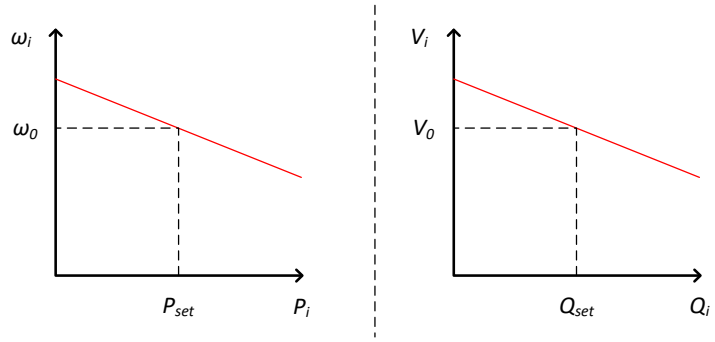

Figure 2.7: Conventional droop control curves

in the voltage and frequency regulation. To this end, the conventional static droop control functions take the form

$$\omega_i = \omega_0 + m_i \left(P_{set} - P_i\right) \tag{2.2}$$

$$V_i = V_0 + n_i \left(Q_{set} - Q_i\right), \tag{2.3}$$

where ω_0 is the nominal angular frequency, V_o is the nominal voltage, m_i and n_i are the droop coefficients which define the power injection according to the deviation from the nominal voltage and frequency and P_i, Q_i are the measured real and reactive powers. In practice, equations (2.2)-(2.3) define the desired output voltage and frequency of a voltage source, as the one shown in Fig. 2.6, where $\theta_i = \omega_i t + \delta_i$. The corresponding droop curves are depicted in Fig. 2.7. It should be highlighted that P_{set} and Q_{set}, which are the reference values of the output real and reactive power, are mostly used during the grid-connected operation, while they are usually removed in the islanded microgrid operation, where producing excess power may lead to instability. Note that aiming to guarantee proportional power sharing between DERs in inverter-based microgrids, all DERs should adopt the same droop control design (e.g. selection of droop coefficients).

As it was discussed, droop control is an important control method due to the advantages that it offers. Hence, it remains an active research topic and new concepts are continuously being proposed. In the following list, some of the most recent advances in droop control of inverter-interfaced DERs are presented:

- Research on output impedance shaping and universal droop schemes: When the output impedance is not of inductive nature, the droop relations of (2.2)-(2.3) can not guarantee the proportional power sharing and the voltage/ frequency regulation anymore. In these cases, the droop relations are modified to $P \sim V$, $Q \sim -\omega$ for resistive output impedance and to $P \sim -\omega$, $Q \sim -V$ for capacitive output impedance [1]. Note that the resistive output impedance scenario mainly corresponds to low voltage power networks or to cases of mixed

output impedance (i.e. resistive-inductive), where a virtual resistance is introduced through the control design to shape the output impedance [1, 76]. Similarly, in the case of mixed output impedance, a virtual inductance may also be introduced through the control design in order to use the conventional droop equations of (2.2)-(2.3). This virtual impedance (resistance or inductance or both) concept is a commonly used technique to ensure the proper operation of droop-controlled inverter-interfaced DERs. Nevertheless, the dynamic stability of the closed-loop system is affected from the introduction of the virtual impedance and this effect should always be considered in the controller analysis [77]. Furthermore, the calculation of the virtual impedance value is a difficult task, since it introduces a virtual voltage drop. In [78], under an adequate selection of droop parameters, the performed analysis shows that power sharing can be properly achieved in a highly resistive AC microgrid by adopting the conventional droop controller instead of the modified $P \sim V$, $Q \sim -\omega$ scheme. In [79], a universal droop control scheme is proposed that does not depend on the nature of the output impedance.

- Research on robustness to system loading: Most of the studies regarding droop control schemes for inverter-based microgrids consider balanced loading and only fundamental frequency components. However, the analysis done for balanced systems does not hold under unbalanced or other distorted conditions. As an example, regarding the analysis of three-phase microgrids in the *dq* frame, the *dq* components do not remain constant (DC) in the steady-state under unbalanced conditions. In [80], unbalanced microgrid loading is considered and in order to overcome the negative sequence current sharing error and the overcurrent stress issues that may occur, a combination of droop control and a supplementary model predictive control (MPC) action is proposed. The proposed scheme can degrade the system unbalance while ensuring the inverter current limitation. Nevertheless, the effectiveness of this technique is not verified experimentally but through simulation results only. The microgrid stability under this control technique is not verified as well. Similarly, droop controllers have been proposed to deal with the sharing of loads with higher harmonic content [1, 81]. Finally, the controller in [76], which introduces the $P \sim V$ and $Q \sim -\omega$ droop equations for the case of resistive output impedance, is shown to achieve a good power sharing even in the case of nonlinear loading.
- Research on enhanced droop control schemes to provide ancillary services: According to the discussion in sec. 2.1, a challenge arises in developing control schemes of inverter-interfaced DERs that combine the droop control mechanism for the steady-state response with extra properties to maintain grid stability during transients. The most common ancillary services that are required from inverter-interfaced DERs have to do with the performance of those units under transients. Aiming to deal with problems arising from the low inertia of inverter-dominated power networks, many droop-based power controllers

have been proposed to virtually introduce inertia to DERs [16, 39, 65], while the optimal placement of virtual inertia has been investigated as well [19]. Nevertheless, recently it has been proven that the conventional droop controller inherits a virtual inertia property through the low pass filter that is usually required for the average real power measurement [63]. Hence, under a certain selection of the control parameters, the droop control and the VSG control schemes become identical. Note though that obtaining the average power through integration (instead of low pass filtering) has been shown to improve inverter transient response [77]. At the same time, other approaches aim to exploit the fast dynamics of inverter-interfaced DERs, such as the V/I droop control proposed in [82]. In [82], it is shown that the power sharing problem can be translated into a current sharing problem, where the nonlinear power measurements are not required. In particular, it is shown that if the inverter reference voltages vary according to the inverter currents, proper power sharing can be achieved. As in the case of the conventional droop control scheme, the dynamic response of the proposed control scheme is mainly associated with the selection of the droop coefficients. Last but not least, since droop-controlled inverters are widely used in grid-connected inverter applications as well, their ability to provide grid voltage support during transients (as discussed in sec. 2.2.2), while ensuring a safe (limited) inverter current injection is of great importance. Hence, rigorous techniques that inherit the desired current limitation in the droop controller have been proposed in [45, 64]. This concept will be analytically discussed in the sequel.

Apart from the aforementioned broad categorization, many strategies that deal with a variety of different issues have been proposed, based on the droop control mechanism. A review about different control strategies that aim to achieve proportional power sharing in islanded microgrids can be found in [83]. In [84], a dual droop control scheme is proposed for two-stage converters. The main novelty of this work lies on the fact that except for the output real and reactive powers, the inverter DC link voltage regulation is considered in the control design in order to avoid the instability that may arise when the required power injection from the droop controller can not be supplied from the prime mover. However, it would be interesting to further consider voltage drops in the AC microgrid, since faults in the AC side may affect the DC-link voltage regulation. As a matter of fact, investigating every proposed control scheme under faulty conditions is essential in order to be considered for real-world applications, since overcurrents or overloading conditions may lead to infrastructure damages. In [85], a droop controller that combines a virtual impedance introduction with a voltage compensation technique is proposed to achieve accurate real and reactive power sharing between DERs in a microgrid, during both the transient state and the steady-state. Balanced, unbalanced and nonlinear loads were considered for the simulation verification, while both single-bus and multi-bus microgrid cases were investigated. However, the stability of the microgrid has not been investigated under the proposed control scheme. In [86], an extra feed-forward term is added

to the current controller of a cascaded droop control scheme in order to facilitate the droop control operation in the grid-connected mode. In the islanded mode, this controller is able to switch between the conventional droop control mode, the power quality control mode (which adapts to the nominal frequency and voltage magnitude values) and the sync control mode (in which the droop characteristics are modified in a way to achieve a smooth grid-connection). However, no stability analysis has been performed to verify this control approach. Furthermore, an enable/disable action of PI controllers is required to change the mode of operation, which can lead to undesirable effects. In [87], proportional real power sharing between DERs and system frequency restoration are guaranteed through the proposed control method. The self-frequency recovery is achieved through a local control loop. Hence, a secondary frequency restoration control is not required. Then, a compensation method is proposed to avoid errors in the real power sharing due to the different instantaneous frequency deviations. Nevertheless, a central secondary control scheme is required for this compensation method, while the stability analysis for this method is missing as well. A similar problem is addressed by the droop control scheme of [88], where a frequency restoration process (named FRP) is used to maintain the frequency at its nominal value, while proportional reactive power sharing is guaranteed as well. Since the droop control approach may be considered for energy storage devices as well, in [89], distributed energy storage devices are considered in an islanded microgrid and a novel droop controller is proposed to guarantee the voltage and frequency regulation, the proportional power sharing and the state of charge (SoC) balancing between the storage devices. The method in [89] is well supported with a stability analysis and experimental results.

Recently, an alternative of the conventional frequency droop control (given in (2.2)) was proposed to improve the voltage and frequency regulation; this is the angle droop control scheme of [90]. Nevertheless, due to the required high droop coefficient, a supplementary control action is essential to maintain closed-loop system stability. The angle droop control concept is also considered in [91], where proportional power sharing is guaranteed without the need of a supplementary control action. However, communication links are required for this control scheme, which degrade the reliability of the proposed control structure. Finally, in [92], the control techniques of virtual impedance introduction, frequency droop and angle droop are analyzed. In particular, it is mathematically proven that angle droop control corresponds to the virtual inductance introduction method, while the virtual inductance method can be considered as same with the frequency droop control with the addition of a derivative term. Particularly, when combining the introduction of virtual inductance and frequency droop control, the result is analogous to the PD (proportional–derivative) frequency droop, which is often introduced in the control system to mitigate power oscillations. The aforementioned conclusions lead to a unified control scheme that combines the properties of the three control techniques under investigation. Furthermore, the presented analysis can provide new perspectives on the design of droop controllers and motivate researchers for technical modifications

to improve the dynamic response of droop-controlled inverters.

Apart from the modifications that have been proposed for the droop control technique to guarantee improved power sharing, enhanced dynamic performance and to provide ancillary services, the applicability of droop control in a variety of applications that require high reliability such as all-electric ships, all-electric aircrafts and isolated community microgrids (microgrids without PCC), should be verified as well. Furthermore, aiming to standardize the droop control operation in the inverter-interfaced DERs of power systems, its operation should always mathematically ensure a stable operation regardless of the system parameters, a task which is really challenging and is usually ignored.

2.6 Stability analysis of inverter-dominated networks

Apart from the appropriate control of inverters to meet the Grid Code requirements, the stability of power systems with high share of inverter-interfaced DERs should be considered for the control design as well. Even if well-known stability tools exist for the conventional power systems structure with centralized generation, these tools cannot be directly applied to power systems or microgrids that host a high share of DERs or operate in the islanded mode, due to the different system dynamics [6, 36]. As an example, one may consider the common assumption used in power system stability studies according to which, the line dynamics are much faster than the generation units dynamics, which allows the use of the admittance matrix in the stability analysis. In the case of inverter-dominated power networks, this assumption does not hold [93]. Another common assumption when investigating power systems with centralized generation, is the existence of a slack bus of constant voltage and frequency which simplifies the power flow and stability analyses. However, this can not be valid in inverter-based microgrids, where voltage and frequency are governed by distributed generation units [6, 36].

Even though the inverter filter and distribution line dynamic models are linear, nonlinearities in the closed-loop system of inverter-interfaced DERs come up due to the power measurements of the power controller, due to nonlinear loads (e.g. constant power loads or converter-fed loads [76]) or due to advanced control schemes with nonlinear dynamics [56]. Hence, the stability analysis of inverter-dominated power networks is a challenging task due to the nonlinear nature of the closed-loop system. To overcome these nonlinearities, the majority of the stability analyses in the literature use the linearization method together with a root-locus analysis, to investigate the stability properties of power systems or microgrids under different control schemes of inverter-interfaced DERs. This method is commonly met in the literature as “small-signal stability analysis.”

One of the first attempts to develop a small-signal model to investigate the stability properties of a droop-controlled inverter-based microgrid, is presented in [94]. However, in this work, the network dynamics are ignored. A more realistic modeling

is performed in [6], where each inverter of the microgrid is modeled in its own dq reference frame and then, all the inverters together with the the lines and the loads of a meshed microgrid, are combined into a global (common) DQ reference frame. The transformation from each local dq frame to the global DQ frame is based on the rotational angle difference of each inverter. The derived model is investigated through sensitivity and root-locus analyses, while it is experimentally verified as well. A thorough description of the global (common) reference frame which is utilized in dq frame-based stability analyses of microgrids is given in [95] and [96]. It should be highlighted that [6] served as a reference for most of the works that followed on small-signal stability analysis of droop-controlled inverter-based microgrids. As a recent example of a microgrid stability investigation that is based on the small-signal technique of [6], a "critical cluster" technique is employed to investigate stability of interconnected inverter-based droop-controlled microgrids in [97]. In [98], an optimization domain of the droop controller parameters is obtained, based on the results of a small-signal stability analysis. It should be highlighted that by adjusting the controller parameters and design according to the results of the stability analysis, the DER control schemes can guarantee the closed-loop system stability. In [99], a small-signal model is utilized to define the angle stability of voltage-controlled inverter-interfaced DERs. Hence, angle stability is researched similarly to the method used for conventional power system studies, i.e. through the $P - \delta$ curve, while the DC bus dynamics of the DER are also considered. As a result, it is revealed that the output impedance of the DER and the line impedance determine significantly the angle stability of the system. In [100], a small-signal stability analysis of a droop-controlled inverter-based microgrid with a centralized secondary control scheme is performed, which takes into account the delays that come up due to the communication links of the central controller. In [101], the possible instability occurring from the interaction of the output impedance of inverters operating in parallel is investigated through a small-signal stability analysis. Moreover, a controller is proposed to enhance microgrid stability. Finally, in the universal droop control scheme of [79], a small-signal stability analysis is performed in order to verify the applicability of the proposed scheme under any type of output impedance. Nevertheless, the above approaches present some drawbacks. Apart from the fact the the original nonlinear model is not considered in those stability analyses, which would provide global stability results but is indeed a daunting task, the main drawback of the studies that employ a root-locus analysis is that the latter tool gives an insight for the stability properties of a given network application only. Thus, there is a challenge in developing more robust methodologies.

Recently, stability of inverter-dominated power networks has been investigated without using the root-locus analysis tool. These approaches are based on determining conditions for stability of inverter-based microgrids or grid-connected inverter-interfaced DERs [102, 103, 104]. In [103], conditions about the voltage droop coefficients are derived to guarantee local asymptotic stability of inverter-based microgrids, under some assumptions on the topology and the electrical characteristics (e.g.

lossless structure and bounded phase angle difference). Hence, the droop controller can be designed accordingly to guarantee the microgrid closed-loop system stability. In [105], a droop-like controller for microgrids is proposed to improve power sharing and guarantee regulation at the nominal frequency. The control design is optimized through a linear matrix inequality problem in order to guarantee stability of the original nonlinear model of a microgrid. In particular, specific control gains can be derived to achieve the desired control properties. In [67], voltage stability is investigated, while ignoring the real power-frequency droop dynamics. Particularly, conditions for local exponential stability are derived under a distributed consensus controller that achieves proportional reactive power sharing in inverter-based microgrids. In [102], stability of the synchronized solution of inverter-based microgrids is investigated. To tackle the synchronization issue, the authors in [102], highlight that an inverter-based microgrid governed by the frequency droop control of (2.2), is equivalent to a network of Kuramoto oscillators. In [106], microgrids with both synchronous machine-based DERs and inverter-interfaced DERs are considered and frequency synchronization is investigated. In particular, conditions are derived to guarantee local stability of the synchronized solution. It should be highlighted that the analyses that determine conditions for stability of power networks represent a more rigorous approach compared to the root-locus analyses, since they do not refer to a specific application. In fact, satisfying the derived conditions for stability based on the worst case scenario, guarantees stability for the whole operation of the grid-connected inverter-interfaced DER or the inverter-based microgrid. However, these approaches usually consider restricting assumptions, such as a lossless network structure, neglecting the output filter dynamics and small or bounded power angles, while abnormal grid conditions are rarely taken into consideration.

To sum up, even if useful stability results can be obtained through the small-signal stability analysis method, there is a challenge in investigating stability of the closed-loop system of inverter-interfaced DERs and inverter-based microgrids without considering a specific application example. An interesting and more rigorous approach is based on deriving conditions for stability of inverter-dominated power networks. Nevertheless, common assumptions that are required to obtain these generic results, may deteriorate the accuracy of the derived conditions.

2.7 Current-limiting control of inverter-interfaced DERs

Although guaranteed stability is a crucial property of power systems, the protection of the inverter devices during abnormal grid conditions is of great importance as well. Abnormal grid conditions may correspond to a variety of grid faults in grid-connected applications, while both overloading and grid faults may lead to abnormal conditions in microgrid applications. Most of the studies that propose control schemes for inverter-interfaced DERs or analyze stability, investigate the operation under normal grid conditions [6, 94, 103, 107]. However, during abnormal grid conditions, the

current injection increases and this can cause damages to the inverter devices which have a limited thermal capability, compared to that of the synchronous generators. At the same time, as it was highlighted in sec. 2.2.2, according to the recent Grid Codes, DERs should not trip in the presence of grid faults but instead, remain connected to the grid and support the PCC voltage. Hence, the safe injection of current (according to the inverter limitations) during abnormal grid conditions represents a great challenge for control system designers.

Indeed, to guarantee the protection of inverter-interfaced DERs, several methods have been proposed for the implementation of current-limiting techniques through the control design. Note that apart from the control-based approaches, hardware techniques can be found in the literature too, based on algorithms which detect the overcurrent and enable external limiters or relay devices, however these techniques have an increased cost and they may restrict the operation according to the FRT requirements. In the context of control-based current-limiting techniques, the most common approaches limit the inverter current reference values through saturation units [108], or in the case of grid-following inverters, by designing the current reference such that it does not violate the maximum allowed current [109]. Furthermore, a switching to a different current-limiting control scheme is employed in some methods, when faulty conditions appear [47]. In [47, 110], the most common current-limiting techniques for grid-forming inverters are presented. The main methods presented in [47, 110] are: the reference inverter current dq components limitation through saturation units, the vector amplitude limitation through saturation units, the switching to a predefined saturated reference value during faults and the current limitation through virtual impedance. Among all these techniques, the prevalent approach is the reference inverter current dq components limitation through saturation units. However, the maximum power utilization is not always available with this technique, since a conservative selection of the upper and lower values of the saturation units is required. Moreover, the techniques that limit the reference inverter current are based on the assumption of the high bandwidth of the current controller, i.e. the current controller is very fast and quickly regulates the inverter current to its reference (limited) value during faults. Finally, the saturation units cause a deactivation of the voltage controller during faults, which can lead to integrator wind-up and instability. Even though, the maximum power injection issue can be addressed through adaptive saturation units [111] or through the vector amplitude limitation technique [110], these alternatives still require saturation units and thus, integrator wind-up remains as their crucial drawback. This led to the development of advanced current-limiting techniques based on the virtual impedance method, as it will be analytically discussed in the literature review that follows.

In [46], a comparison of current-limiting methods that have been proposed in the literature is provided. All the considered techniques are experimentally tested, with the response of currents and voltages being mainly observed, in order to determine the effectiveness of each technique in limiting the injected current and in returning to its initial operation, when the fault is cleared. Apart from the inverter response

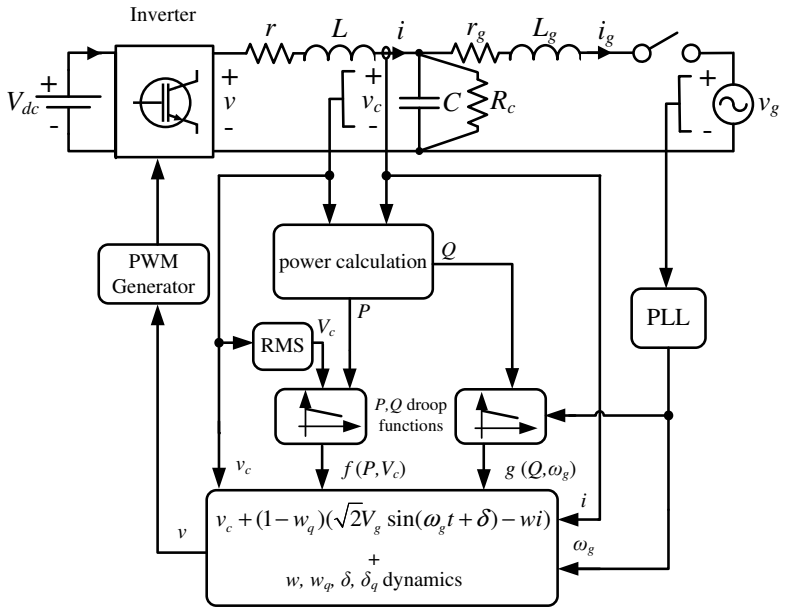

Figure 2.8: Current-limiting droop control design [45]

to the fault appearance, the post fault operation is a crucial aspect of designing current-limiting techniques as well. As it is explained in [46], two problems may occur when the employed control technique switches to a different controller during faults, integrator wind-up and latch up. Integrator wind-up occurs when the original controller keeps integrating during the fault and the output of the PI controller may result to overshoots when the fault is cleared. Latch up occurs when the current-limiting controller remains enabled when the fault is cleared, instead of granting control back to the original controller. In the same work, conclusions are derived on how current-limiting techniques should be designed in order to avoid such phenomena and specifically, set and reset functions are proposed. In [52], it is underlined that the widely used current-limiting technique through saturation units can lead to integrator wind-up and instability. As a matter of fact, the use of saturation units is similar to switching to a different control scheme, since when the output of the voltage controller is saturated, the voltage controller is unable to act. Then, it is proven that the use of a virtual impedance for the current limitation can improve the transient stability, since it effectively limits the voltage reference, instead of saturating the output of the voltage controller. Specifically, under faulty or overload conditions, the virtual impedance rises to higher values, thus reducing the injected current without deactivating the voltage controller. Similar current-limiting techniques which use the virtual impedance concept have been also proposed in [47, 112]. However, the aforementioned techniques require additional control loops and a smart tuning to define the value of the virtual impedance that needs to be added through the controller during faults, while saturation units may be required in these loops as well. To overcome these issues, a current-limiting property is introduced in the droop controller operation in [64]. Nevertheless, the

line impedance is required for the implementation of this technique, which is a strict requirement.
A new current-limiting controller was proposed in [43], that inherits the current limitation property in the power controller loop through the bounded integral controller (BIC) structure, proposed in [56]. In practice, the current limitation is accomplished by feed-forwarding the output voltage and at the same time introducing a dynamic virtual resistance with given bounds. Through this dynamic virtual resistance, the power controller operation is inherited in the control design. Furthermore, in [43], it is mathematically proven that the proposed controller can guarantee the limitation of the inverter current under a given maximum value, without any switching actions or saturation units. In [45], an extension of this technique, the Current-Limiting Droop (CLD) controller, is proposed. Compared with the original controller of [43], the CLD does not have a self-synchronization capability but has the ability to regulate real and reactive power to its reference values or operate under the droop control law, while the original control scheme of [43] was operating under unity power factor and the real power controller operation was restricted to regulating the output real power to its reference value.

According to [45], the CLD is defined using the universal robust droop control scheme functions [79], and the inverter voltage (control input) is proposed as follows:

$$v = v_c + (1 - w_q)(\sqrt{2}V_g \sin(\omega_g t + \delta) - wi), \tag{2.4}$$

where v_c is the LCL filter capacitor voltage with V_c being its RMS value and V_g and ω_g correspond to the RMS grid voltage and grid frequency, respectively. The control state w is a dynamic virtual resistance and w_q is an auxiliary control state. Similarly, δ is a phase shift, with δ_q being an extra control state. These control states vary according to the BIC scheme, through the functions

$$\begin{aligned}
\dot{w} &= -c_w(K_e(E^* - V_c) - n(P - P_{set}))w_q^2 \\
\dot{w}_q &= \frac{c_w(w - w_m)w_q}{\Delta w_m^2}(K_e(E^* - V_c) - n(P - P_{set})) - k_w\left(\frac{(w - w_m)^2}{\Delta w_m^2} + w_q^2 - 1\right)w_q \\
\dot{\delta} &= c_\delta(\omega^* - \omega_g + m(Q - Q_{set}))\delta_q^2 \\
\dot{\delta}_q &= -\frac{c_\delta \delta \delta_q}{\Delta \delta_m^2}(\omega^* - \omega_g + m(Q - Q_{set})) - k_\delta\left(\frac{\delta^2}{\Delta \delta_m^2} + \delta_q^2 - 1\right)\delta_q,
\end{aligned}$$

to achieve the desired current limitation and droop control functionality. Note that c_w, c_δ, K_e are constant positive gains, w_m, Δw_m, $\Delta \delta_m$ are control parameters and n, m are the droop coefficients. The CLD controller is depicted in Fig. 2.8.

Nevertheless, in [43, 45], the maximum power capability is not utilized during faults since the current provision depends on the amount of the residual voltage. This fact violates the demand of the modern Grid Codes for voltage support under grid faults. Furthermore, the CLD control scheme has been proposed and verified solely

for single-phase grid-connected inverters. A framework to be applied to three-phase inverters and extend the controller application to MV and HV networks is missing, while extending its properties to microgrid scenarios would be of great interest as well. Finally, the asymptotic stability of the closed-loop system under the CLD control scheme remains unverified.

2.7.1 Current limitation under the "voltage support concept"

Even though similar current-limiting techniques are used in both single-phase and three-phase applications, the main feature that differentiates the three-phase scenario is the case of unbalanced grid faults. In fact, the majority of grid faults are single-phase to ground or phase to phase faults, while balanced three-phase faults correspond to a rare case.

From sec. 2.2.2, it can be concluded that under balanced faulty conditions, the limitation of the total current and the maximum power injection for supporting the grid voltage are the two main tasks of the inverter. However, when unbalanced faults appear at the grid, the selection of the appropriate strategy to optimally provide voltage support, is a complicated problem [32, 113]. Significant amount of research has addressed the inverter response through grid-following current controllers that inject both positive and negative sequence currents, in order to provide voltage support in terms of positive sequence voltage support and negative sequence voltage elimination [35, 114]. The voltage support concept is thoroughly presented in [35], where current controllers that employ symmetrical components theory and reduce the voltage unbalance factor (VUF) are reviewed. Nevertheless, the way current limitation is achieved under unbalanced grid conditions still represents a challenging task, especially when grid-forming droop-controlled inverters are considered, since their task is to regulate the grid voltage and frequency. The authors in [30, 31] have implemented power controllers that ensure a balanced current provision under voltage sags. As explained in [30], this enhances the fault-ride-through capability in terms of injecting only positive sequence powers/current that comply with the FRT requirement, while current limitation at the steady-state is achieved through the real and reactive power set points. However these approaches do not deal with negative sequence voltage mitigation. In the latter case, injection of both positive and negative sequence currents is required while the selection of the current amplitude in each sequence is a difficult task as well. An explanation of two limiting methods (i.e. the straight forward technique and the advanced technique) of the total current, when injecting current in both sequences, is given in [34, 115].

Regarding the control schemes that have investigated voltage unbalance elimination through grid-forming converters, in [33], a negative sequence droop controller is presented which manages to mitigate the voltage unbalance at the point of common coupling under voltage drops. Nevertheless, current limitation is not considered in this control design; instead, saturation units are used in the negative sequence reference power generation unit. A current-limiting scheme in both sequences for voltage

controllers is presented in [111] and [116] for microgrid and grid-connected applications, respectively, where the novel theory from [117] is introduced and employed. However, the current limitation is performed through saturation units that can lead to instability, while the droop control concept is not considered in the control design.

Table 2.1: System and controller parameters for the case study

Parameters	Values	Parameters	Values
L_1, L_2	2.2 mH	C_1, C_2	1 μF
r_{l1}, r_{l2}	0.04 Ω, 0.02 Ω	L_{l1}, L_{l2}	3 mH, 2 mH
ω^*	314.15 rad/s	E^*	220 V
n_1	0.0047	m_1	0.0012
n_2	0.0094	m_2	0.0024
I_1^{rated}	20 A	I_2^{rated}	10 A
I_1^{max}	40 A	I_2^{max}	10 A

2.7.2 Case study: Current limitation through saturation units

As it has been highlighted in [52], when a droop-controlled inverter-interfaced DER that uses saturation units in the inner loops as a current-limiting method operates in parallel to a synchronous machine-based DER (i.e. a unit with a different transient frequency response), integrator wind-up can occur in the inverter-interfaced DER under abrupt load changes or grid faults. In particular, when saturation units are placed in the output of the voltage controller to ensure the desired current limitation, the voltage controller gets deactivated during transients, thus losing the ability to control the output voltage. In this case, the phase shift of the inverter drifts away and the voltage controller suffers from integrator wind-up. As shown in [52], this can lead to a number of undesirable events such as transient instability and violation of the inverter current limit. Apart from the case of parallel operation of an inverter-interfaced DER and a synchronous machine-based DER, similar events occur in the cases of parallel inverter-interfaced DERs with different virtual inertia constants and parallel inverter-interfaced DERs with different p.u. maximum current. In this case study, two inverter-interfaced DERs are considered, which operate in parallel and have different p.u. maximum allowed currents. We showcase that undesirable events can occur during sadden load changes or grid faults. Hence, we highlight that the current-limiting techniques which utilize saturation units in cascaded droop controllers may lead to instability even in inverter-based microgrid applications.

In order to perform the case study, Matlab/Simulink simulation results are provided for an inverter-based microgrid consisting of two inverter-interfaced DERs

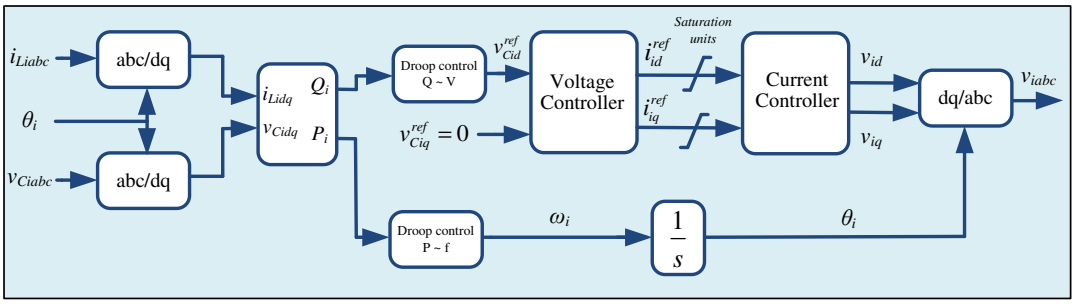

Figure 2.9: Inverter control scheme for the case study

connected to a common resistive-inductive load (RL), through an $L_iC_iL_i$ filter and a resistive-inductive $(r_{li}L_{li})$ line. The controller under consideration is the conventional cascaded droop controller, as it is presented in [6, 52] and depicted in Fig. 2.9, with saturation units placed at the inverter reference currents, while voltage feedforward terms are also added to the current controller since they can improve the effectiveness of the current limitation [47]. The power system and controller parameters are given in Tab. 2.1. The maximum inverter currents are selected as $I_1^{max} = 2I_1^{rated} = 2\,\text{p.u.}$ and $I_2^{max} = I_2^{rated} = 1\,\text{p.u.}$, which represents a real-world scenario since according to the inverter manufacturer, a different maximum current may be allowed [47, 118]. Moreover, it is considered that Inverter #1 has twice the capacity of Inverter #2. The presented simulation scenario in Fig. 2.10, is as follows: Initially, both inverters do not feed the load since their PCC switches are open while at 0.1 s, the first inverter is connected to the load which initially has the value $R = 25\,\Omega$ and $L = 40\,\text{mH}$. At 0.3 s, the second inverter is connected to the common load bus and at 2 s, a sudden load change takes place with the total load being driven to a very low resistive value. In this case, the required current for regulation close to the load voltage and frequency set points is higher than the total capacity of both inverters. In practice, this loading case corresponds to a microgrid fault. At 2.6 s, the load is returned to its initial value. As it is observed in Fig. 2.10, due to the integrator wind-up and phase shift drift issues, the inverters never return to their normal operation. This is caused due to the fact that the voltage controller of the second inverter loses its controllability, as it is clear from Fig. 2.10f. Hence, the second inverter current never returns from its maximum value while it also flip flops between the maximum and minimum values of the saturation units, as it can be understood from Fig. 2.10c. This has also been explained in [52]. It should be finally highlighted that the reactive power sharing operation is completely distorted with the second inverter absorbing reactive power instead of taking part in the load voltage regulation. Hence, the load voltage regulation is deteriorated, as it is depicted in Fig. 2.10d.

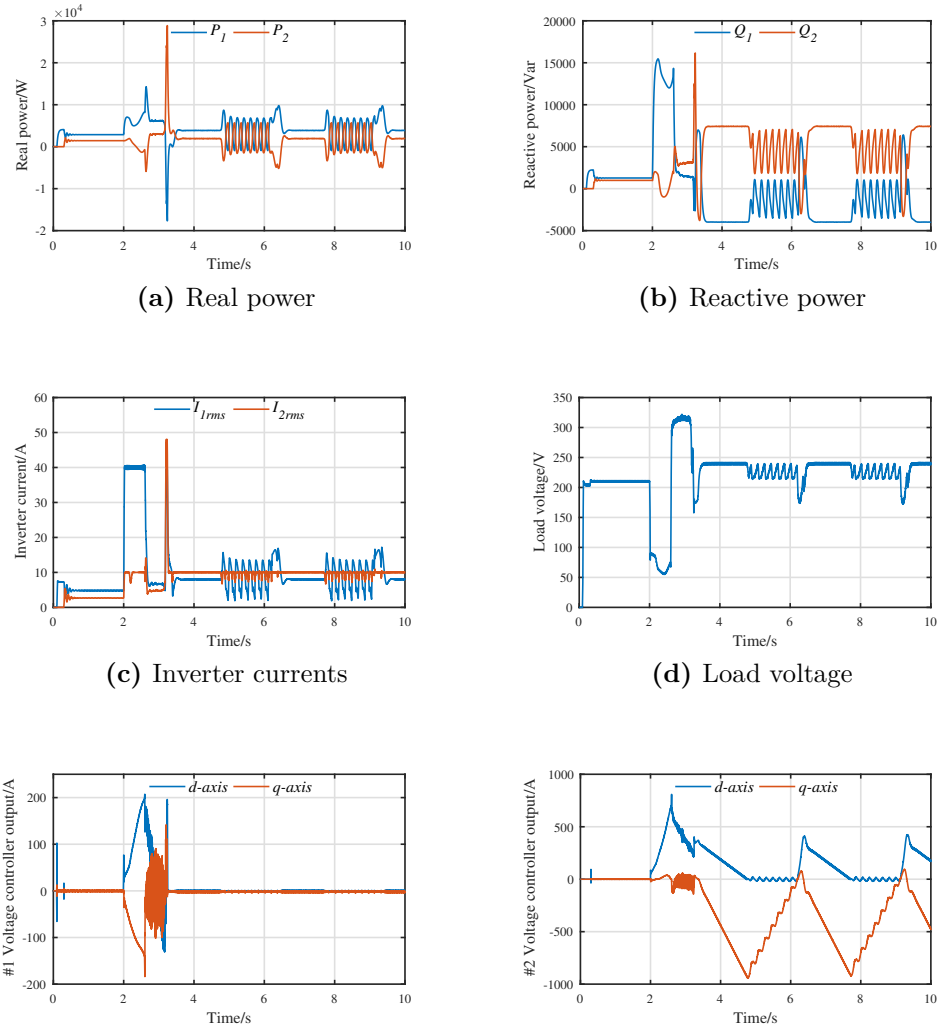

(a) Real power **(b)** Reactive power

(c) Inverter currents **(d)** Load voltage

(e) Inverter #1 voltage controller output **(f)** Inverter #2 voltage controller output

Figure 2.10: Microgrid operation with conventional current-limiting control of cascaded droop-controlled inverters

2.8 Literature gaps and challenges to be addressed

According to the discussions and the literature review presented in this chapter, droop control, current-limiting techniques of inverter-interfaced DERs and stability analysis of power networks dominated by inverter-interfaced DERs, are active research topics and there are still crucial challenges to be tackled. Furthermore, a property that the inverter control scheme should ideally have, is to operate in a unified way under normal and abnormal grid conditions. One may also notice, that these challenges correspond to a cross disciplinary research area between power system analysis, control systems design and analysis, and power electronics experimental applications. This makes contributing in this specific research field an even more challenging task. According to the findings of this chapter, the main challenges for

this thesis will be now outlined for the scenarios of grid-connected inverter-interfaced DERs and inverter-interfaced DERs that form inverter-based microgrids.

In the grid-connected applications, the main challenges lie on developing unified control schemes for inverters to:

- Support the grid voltage and frequency during normal grid conditions, according to the Grid Code.
- Support grid voltage when balanced and unbalanced faults occur, according to the voltage support concept and the fault-ride-through requirements.
- Contribute to system's protection through advanced current-limiting control techniques that allow the operation of the aforementioned voltage support schemes.
- Introduce a virtual inertia property, aiming to mimic the transient response of synchronous generators.
- Inherit a self-synchronization mechanism – no PLL requirement.
- Guarantee closed-loop system stability of grid-tied inverters, by deriving the necessary conditions for asymptotic stability.

In the case of inverter-interfaced DERs that form inverter-based microgrids, the main challenge lies on developing a unified control scheme for the inverters to:

- Contribute to system's protection by developing advanced current-limiting techniques that are not prone to integrator wind-up.
- Inherit the current-limiting technique in the power controller loop, without additional adaptive techniques that are usually employed in the dq framework.
- Achieve power sharing between inverter-interfaced DERs, without additional communication units that increase cost and decrease reliability.
- Guarantee stability for an entire microgrid.

The development of such control schemes will lead to a new generation of smart inverters with advanced control and protection features which will pave the way towards reliable and resilient power networks and microgrids, with a high penetration level of inverter-interfaced DERs. The facilitation of increased power generation from inverter-interfaced DERs will lead to a rise in "clean" energy production and contribute to the environmental and sustainability policies.

3 Preliminaries

In order to address the challenges that were discussed and posed in the previous chapter (e.g. inherent current-limiting property of inverters and closed-loop system stability of inverter-dominated power networks), a rigorous mathematical analysis is required. As it was highlighted in sec. 2.6, even if most of the dynamic models of power system components are linear (e.g. inverter output filter and line dynamic models), the closed-loop system of inverter-dominated power networks is usually of nonlinear nature. This is due to the power calculations that are required for the operation of the power control schemes or due to advanced control schemes with nonlinear dynamics or due to nonlinear system loading. Hence, stability tools for nonlinear systems are of great importance for the issues tackled throughout this thesis. This chapter highlights theorems and tools, which are utilized in the analysis of the control schemes proposed in the sequel of this thesis.

3.1 Lyapunov indirect method

In this section, the "Lyapunov's first" or "indirect" method is presented. This method investigates the stability properties of a nonlinear system, based on the fact that in a small area around an equilibrium point, we can study the behavior of a nonlinear system through its linear approximation about that equilibrium point. It is noteworthy that the transient response of a linear or a nonlinear system around an equilibrium point can be investigated through its response around the origin of the state-space, by shifting the equilibrium point to the origin [119, 120]. Hence, without loss of generality, most of the theorems regarding closed-loop system stability investigate the case where the origin of the state-space corresponds to the desired equilibrium point.

Theorem 1 [119]**:**

Let $x = 0$ be an equilibrium point for the nonlinear system

$$\dot{x} = f(x) \tag{3.1}$$

where $f : D \rightarrow R^n$ is continuously differentiable and D is a neighborhood of the origin. Let

$$A = \left.\frac{\vartheta f}{\vartheta x}(x)\right|_{x=0}$$

Then,

1. *The origin is asymptotically stable if* $Re\lambda_i < 0$ *for all eigenvalues of* A.
2. *The origin is unstable if* $Re\lambda_i > 0$ *for one or more of the eigenvalues of* A.

The proof of Theorem 1 can be found in [119], 3rd Edition, Th. 4.7.

3.2 Ultimate boundedness

In many engineering applications, it is crucial to guarantee boundedness of the solution of the system state equations. Notably, in inverter-interfaced DER applications (that this thesis focuses on), it is of great interest to rigorously guarantee the boundedness of the power system and control system states, instead of using methods which can degrade system stability, such as saturation units. A "Lyapunov-like" theorem for proving ultimate boundedness for the states of the system

$$\dot{x} = f(t, x), \tag{3.2}$$

is the one that follows.

Theorem 2 [119]**:**

Let $D \in R^n$ *be a domain that contains the origin and* $V : [0, \infty) \times D \to R$ *be a continuously differentiable function such that*

$$\alpha_1(\|x\|) \leq V(t, x) \leq \alpha_2(\|x\|)$$
$$\frac{\vartheta V}{\vartheta t} + \frac{\vartheta V}{\vartheta x} f(t, x) \leq -W_3(x), \forall \|x\| \geq \mu > 0$$

$\forall t \geq 0$ *and* $\forall x \in D$, *where* α_1 *and* α_2 *are class* $\mathcal{K}$ *functions and* $W_3(x)$ *is a continuous positive definite function. Take* $r > 0$ *such that* $B_r \subset D$ *and suppose that*

$$\mu < \alpha_2^{-1}(\alpha_1(\rho)).$$

Then, there exists a class $\mathcal{KL}$ *function* β *and for every initial state* $x(t_0)$, *satisfying* $\|x(t_0)\| \leq \alpha_2^{-1}(\alpha_1(\rho))$, *there is* $T \geq 0$ *(dependent on* $x(t_0)$ *and* μ*) such that the*

solution of (3.2) *satisfies*

$$\|x(t)\| \leq \beta(\|x(t_0)\|, t - t_0), \forall t_0 \leq t \leq t_0 + T \tag{3.3}$$

$$\|x(t)\| \leq \alpha_1^{-1}(\alpha_2(\mu)), \forall t \geq t_0 + T. \tag{3.4}$$

Moreover, if $D = R^n$ *and* α_1 *belongs to class* $\mathcal{K}_\infty$, *then* (3.3) *and* (3.4) *hold for any initial state* $x(t_0)$, *with no restriction on how large* μ *is.*

The proof of Theorem 2 can be found in [119], 3rd Edition, Th. 4.18.

An interesting note in [119], which may be useful when using this theorem, states that if $\|x(t_0)\| \leq \alpha_1^{-1}(\alpha_2(\mu))$, then $T = 0$, i.e.

$$\|x(t)\| \leq \alpha_1^{-1}(\alpha_2(\mu)), \forall t \geq 0.$$

3.3 Input-to-state stability

The "input-to-state stability" notion is extending the Lyapunov stability tools to systems with inputs, such as the nonlinear non-autonomous system described by

$$\dot{x} = f(t, x, u). \tag{3.5}$$

Theorem 3 [119]**:**

Let $V : [0, \infty) \times R^n \to R$ *be a continuously differentiable function such that*

$$\alpha_1(\|x\|) \leq V(t, x) \leq \alpha_2(\|x\|)$$

$$\frac{\vartheta V}{\vartheta t} + \frac{\vartheta V}{\vartheta x} f(t, x, u) \leq -W_3(x), \forall \|x\| \geq \rho(\|u\|) > 0$$

$\forall (t, x, u) \in [0, \infty) \times R^n \times R^m$, *where* α_1, α_2 *are class* $\mathcal{K}_\infty$ *function,* ρ *is a class* $\mathcal{K}$ *function, and* $W_3(x)$ *is a continuous positive definite function on* R^n. *Then, the*

system (3.5) *is input-to-state stable with* $\gamma = \alpha_1^{-1} \circ \alpha_2 \circ \rho$.

The analytical proof of Theorem 3, which is based on the ultimate boundedness property of Theorem 2, can be found in [119], 3rd Edition, Th. 4.19.

3.4 Stability of interconnected systems

In a variety of engineering problems and particularly in power systems, the subsystems of a larger system may form an interconnected system of the following form, as described in [119].

Initially, consider the interconnected system

$$\dot{x}_1 = f_1(t, x_1, x_2) \tag{3.6}$$

$$\dot{x}_2 = f_2(t, x_2), \tag{3.7}$$

where $f_1 : [0, \infty) \times D_1 \times D_2 \rightarrow R^{n_1}$ and $f_2 : [0, \infty) \times D_2 \rightarrow R^{n_2}$ are piecewise continuous in t and locally Lipschitz in x; $x \stackrel{def}{=} [x_1\ x_2]^T$. The set D_i is a domain in R^{n_i} that contains the origin $x_i = 0$; in the global case, we take $D_i = R^{n_i}$.

In these cases, the following theorem can be found of use in the closed-loop system stability investigation.

Theorem 4 [119]**:**

Under the stated assumptions

- *If the system* (3.6)*, with* x_2 *as input, is input-to-state stable and the origin of* (3.7) *is uniformly asymptotically stable, then the origin of the interconnected system* (3.6)-(3.7) *is uniformly asymptotically stable.*
- *If the system* (3.6)*, with* x_2 *as input, is input-to-state stable and the origin of* (3.7) *is globally uniformly asymptotically stable, then the origin of the interconnected system* (3.6)-(3.7) *is globally uniformly asymptotically stable.*

Theorem 4 and its proof can be found in [119], 2nd Edition, Lemma 5.6.

3.5 Bounded integral control

Recently, the bounded integral control (BIC) structure was proposed in [56]. The BIC aims to mimic the operation of a traditional integral controller and moreover,

guarantee the boundedness of the control state (plant control input), while maintaining the stability properties of the conventional integral control scheme. The structure and the operation of the BIC is briefly explained in the remainder of this section.

Initially, consider the plant $\dot{x} = f(x, u)$. In order for the control input u to remain inside a given bounded range $[-u_{max}, u_{max}]$, the BIC dynamics take the form

$$\begin{bmatrix} \dot{w} \\ \dot{w}_q \end{bmatrix} = \begin{bmatrix} 0 & k_I g(x) \frac{w_q u_{max}^2}{u_{max}^2 - u_c^2} \\ -k_I g(x) \frac{w_q}{u_{max}^2 - u_c^2} & -k_q \left(\frac{w^2}{u_{max}^2} + w_q^2 - 1 \right) \end{bmatrix} \begin{bmatrix} w \\ w_q \end{bmatrix} \tag{3.8}$$

where $u = w$, k_I is the integral gain, k_q is a positive constant, $g(x)$ is the function to be regulated, $u_c \in (-u_{max}, u_{max})$ is a constant and the states initial values are selected as $w_0 = 0$ and $w_{q0} = 1$. Through the analysis in [56], based on the stated initial conditions, it is proven that using the BIC structure, the control states will start and remain on the ellipse

$$W_0 = \left\{ w, w_q \in R, \ \frac{w^2}{u_{max}^2} + w_q^2 = 1 \right\}.$$

Hence, the desired boundedness of the control input is inherently guaranteed by the BIC. The analytical proofs of the BIC properties can be found in [56].

4 Enhanced current-limiting droop control of single-phase grid-connected inverters

4.1 Motivation and novel outcome

The ancillary services that Grid Codes require from DERs continuously get updated, as the share of DERs in power systems is increasing. Among other ancillary services, the requirements regarding the response of DERs during grid faults are of great importance. In order to increase the reliability in power system operation, DERs are expected to remain connected to the grid and provide voltage support by injecting maximum available power, instead of tripping, during grid faults. This brings a significant challenge in the inverter-interfaced DERs control system design, since advanced control schemes are required to guarantee at the same time a rigorous current limitation for inverter protection, maximum power injection for voltage support and closed-loop system stability.

In [45], it is proven that the proposed current-limiting droop controller limits the RMS value of the inverter current under a given value, without employing saturation units which may lead to instability [52]. However, the maximum capacity of the inverter is not utilized under grid voltage drops, since the current is limited to a value proportional to the residual voltage. As an example, in the case of a solid short circuit, the inverter current is limited to zero, which is similar to disconnecting the inverter. Hence, reactive power cannot be maximized to provide voltage support to the grid during voltage drops, as demanded by the recent FRT requirements. Furthermore, stability is guaranteed only in the sense of inverter current boundedness, while the proof of regulation to the desired equilibrium is still missing. Finally, the CLD control method for grid-connected inverters requires a PLL device for its implementation and does not introduce any virtual inertia to the system, a property which is expected to be an essential requirement in future power systems.

To deal with the above stated limitations, an enhanced version of the CLD controller is initially proposed in this chapter, in sec. 4.2. Opposed to the original CLD which limits the inverter current under a lower value than its maximum when voltage sags occur, the proposed controller fully utilizes the capacity of the inverter, by injecting the maximum allowed current during any grid fault. Hence, the enhanced

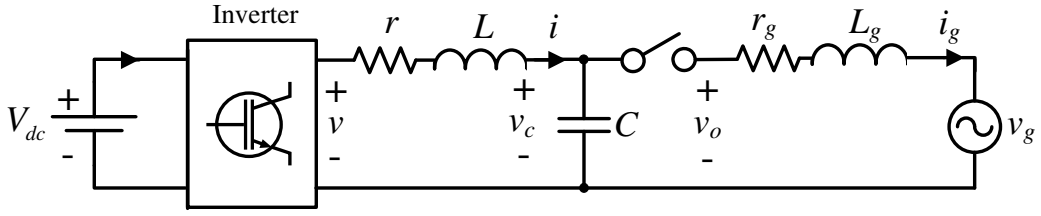

Figure 4.1: Single-phase inverter connected to the grid through an LCL filter

CLD scheme allows the implementation of a rigorous FRT technique to provide voltage support during faults. Furthermore, conditions for asymptotic stability of the closed-loop system are derived, to deal with the challenging task of guaranteeing the stability properties of inverter-interfaced DERs. Then, in sec. 4.3, an extension of the proposed enhanced CLD controller is developed, which operates without the need of a PLL device and at the same time introduces a virtual inertia property to the inverter-interfaced DER.

4.2 Enhanced current-limiting droop controller to guarantee stability and maximize power injection under grid faults

4.2.1 System modeling

The power system under consideration is a single-phase inverter connected to the grid through an LCL filter, as depicted in Fig. 4.1. The capacitor of the filter is denoted as C while the inductances are denoted as L and L_g with r and r_g being their parasitic resistances, respectively. The output voltage and current of the inverter are v and i, while the capacitor voltage is denoted as v_c. The voltage and current of the grid are v_g and i_g with $v_g = \sqrt{2}V_g \sin \omega_g t$, where V_g is the RMS grid voltage and ω_g is the angular grid frequency.

The dynamic equations of the system can be obtained as

$$\begin{aligned} L\frac{di}{dt} &= v - v_c - ri \\ C\frac{dv_c}{dt} &= i - i_g \\ L_g\frac{di_g}{dt} &= v_c - v_g - r_g i_g \end{aligned} \tag{4.1}$$

where v represents the control input and corresponds to the voltage at the output of the inverter.

4.2.2 The proposed controller

The main goal in this section is to propose a droop controller that inherently limits the inverter current to protect the device under unrealistic power demands or under grid faults, while supporting the grid voltage at all times. Hence, inspired by the structure of the original CLD in [45], a dynamic virtual resistance is introduced in series with the filter inductor through the control input v, which should remain positive and bounded. Although this bounded dynamic virtual resistance can be implemented using traditional integral control with saturation, such an approach can lead to integrator wind-up and instability [52]. Therefore, the bounded integral control (BIC) concept proposed in [56] is utilized here to overcome this limitation. Finally, in order to provide robustness to different output impedance, the $P \sim V$ and $Q \sim -\omega$ droop expressions of the universal droop controller are employed [76, 79].

As it was mentioned in the previous section, the main limitations of the original CLD control technique are i) the failure to utilize the maximum inverter capacity during faults and ii) the absence of an asymptotic stability analysis. In order to overcome the maximum power utilization issue, the maximum value of the inverter current should not be defined by the residual voltage during grid faults, but by the nominal load voltage. Furthermore, in order to provide a rigorous asymptotic stability analysis, it would be advantageous to remove the extra control state of the BIC from the inverter voltage equation. Hence, the novel control structure of the current-limiting droop controller proposed in this thesis takes the form:

$$v = v_o + \frac{(w - w_m)^2}{\Delta w_m^2}\left(\sqrt{2}E^* \sin(\omega_g t + \delta) - wi\right), \tag{4.2}$$

with control dynamics

$$\begin{bmatrix} \dot{w} \\ \dot{w}_q \end{bmatrix} = \begin{bmatrix} 0 & -c_w f(P_g, V_g) w_q^{2l-1} \\ \frac{c_w w_q}{l\Delta w_m^2} f(P_g, V_g) & -\frac{k_w}{l}\left(\frac{(w-w_m)^2}{\Delta w_m^2} + w_q^{2l} - 1\right) \end{bmatrix} \begin{bmatrix} w - w_m \\ w_q \end{bmatrix} \tag{4.3}$$

$$\begin{bmatrix} \dot{\delta} \\ \dot{\delta}_q \end{bmatrix} = \begin{bmatrix} 0 & c_\delta g(Q_g, \omega_g) \delta_q^{2l-1} \\ -\frac{c_\delta \delta_q}{l\Delta\delta_m^2} g(Q_g, \omega_g) & -\frac{k_\delta}{l}\left(\frac{\delta^2}{\Delta\delta_m^2} + \delta_q^{2l} - 1\right) \end{bmatrix} \begin{bmatrix} \delta \\ \delta_q \end{bmatrix} \tag{4.4}$$

where $l \geq 1 \in \mathcal{N}$ and $f(P_g, V_g)$ and $g(Q_g, \omega_g)$ are given by

$$f(P_g, V_g) = n(P_{set} - P_g) + K_e(E^* - V_g) \tag{4.5}$$

$$g(Q_g, \omega_g) = m(Q_g - Q_{set}) + \omega^* - \omega_g \tag{4.6}$$

and represent the droop control expressions, with c_w, c_δ, k_w, k_δ, w_m, Δw_m and $\Delta\delta_m$ being positive constant parameters of the controller, E^* and ω^* being the rated grid voltage and frequency and n, m representing the droop coefficients. The initial conditions are defined as $w_0 = w_m, w_{q0} = 1$ and $\delta_0 = 0, \delta_{q0} = 1$. The proposed controller implementation is depicted in Fig. 4.2. Comparing (4.2) with the original

CLD expression (2.4), one can notice that the term $(1 - w_q)$ has been replaced by $\frac{(w-w_m)^2}{\Delta w_m^2}$ to facilitate the closed-loop system stability analysis and that the controlled voltage source in (4.2), uses the rated voltage E^* instead of the grid voltage, in order to allow the maximum power utilization under grid faults. These novel properties will be analytically proven in the sequel.

As it is obvious from Fig. 4.1, when the inverter is not connected to the grid, then $v_o = v_g$ and when the relay closes, $v_o = v_c$. Parameters w and δ represent a virtual resistance and phase shift, respectively, which vary according to the nonlinear dynamic expressions (4.3)-(4.4). In order to guarantee boundedness of the controller states w, w_q, δ and δ_q without using saturation units, a generalized version of the BIC [56], is proposed in this section depending on the value of $l \geq 1 \in \mathcal{N}$. Through this approach, it is guaranteed that w is bounded in the range $[w_{min}, w_{max}] > 0$ and δ is bounded in the range $\delta \in [-\Delta\delta_m, \Delta\delta_m]$.

To further explain this boundedness property, consider initially the continuously differentiable function

$$W_w = \frac{(w - w_m)^2}{\Delta w_m^2} + w_q^{2l}$$

for system (4.3). The time derivative of W_w takes the form

$$\dot{W}_w = \frac{2(w - w_m)\dot{w}}{\Delta w_m^2} + 2l w_q^{2l-1} \dot{w}_q$$

which by substituting $\dot{w}$ and $\dot{w}_q$ from (4.3) becomes

$$\dot{W}_w = -2k_w \left(\frac{(w - w_m)^2}{\Delta w_m^2} + w_q^{2l} - 1 \right) w_q^{2l}.$$

According to the stated initial conditions (i.e. $w_0 = w_m$ and $w_{q0} = 1$), it holds true that $\dot{W}_w = 0$, i.e. $W_w(t) = W_w(0) = 1$. Hence, the controller states w and w_q will start and remain on the set $E_w = \left\{ w, w_q \in R : \frac{(w-w_m)^2}{\Delta w_m^2} + w_q^{2l} = 1 \right\}$, yielding the desired boundedness property of the controller state w, i.e. $w \in [w_m - \Delta w_m, w_m + \Delta w_m] = [w_{min}, w_{max}], \forall t \geq 0$, for $w_m > \Delta w_m > 0$. A similar analysis holds for the controller states δ and δ_q by considering the continuous differentiable function $W_\delta = \frac{\delta^2}{\Delta\delta_m^2} + \delta_q^{2l}$ for the system (4.4), thus guaranteeing that states δ and δ_q will start and remain on the set $E_\delta = \left\{ \delta, \delta_q \in R : \frac{\delta^2}{\Delta\delta_m^2} + \delta_q^{2l} = 1 \right\}$, based on the given initial conditions $\delta_0 = 0, \delta_{q0} = 1$.

From the above analysis it is concluded that $w \in [w_{min}, w_{max}] > 0$ and $\delta \in [-\Delta\delta_m, \Delta\delta_m]$ for all $t \geq 0$. Note that for $l = 1$, the dynamics (4.3)-(4.4) take

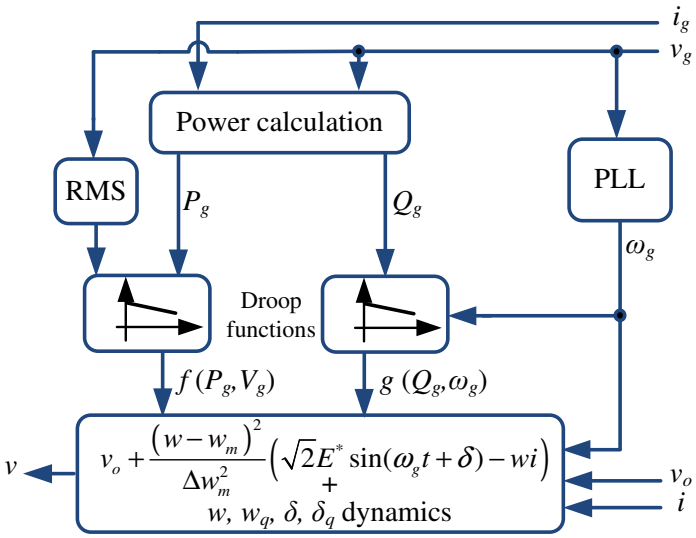

Figure 4.2: Proposed controller implementation

the form of the original BIC [56], while $w_{min} = w_m - \Delta w_m$, $w_{max} = w_m + \Delta w_m$, $\Delta\delta_m$ can be set by the control operator and represent the minimum and maximum values of the virtual resistance and the maximum absolute value of the phase shift, respectively.

Regarding the selection of the rest of the controller parameters, the variables c_w and c_δ represent the controller integral gains and the variables k_w and k_δ are used to increase the robustness of the control states w_q and δ_q. These parameters can be selected according to the analysis in [45]. Furthermore, note that $w_0 = w_m$ corresponds to the initial current I_m that flows through the LC filter when the switch in Fig. 4.1 is open (before grid connection) and thus, it can be selected as $w_m = \frac{E^*}{I_m} = \frac{E^*}{\omega_g C V_g}\sqrt{\left(1-\omega_g^2 LC\right)^2 + (r\omega_g C)^2}$.

Note that at the steady-state, the functions (4.5) and (4.6) get to 0, i.e. it holds $V_g = E^* + \frac{n}{K_e}(P_{set} - P_g)$ and $\omega_g = \omega^* + m(Q_g - Q_{set})$. Hence, the proposed control scheme adopts the droop control scheme proposed in [79]. Moreover, by removing the terms $K_e(E^* - V_g)$ and $\omega^* - \omega_g$ from equations (4.5) and (4.6), the proposed controller can easily change its operation from the PQ-droop mode to the PQ-set mode in order to regulate the real and reactive power at their reference values. It is underlined that, compared to the original CLD in [45], here the proposed enhanced controller introduces the generalized nonlinear dynamics (4.3)-(4.4) and a different expression for the control input v given in (4.2). In particular, the proposed inverter voltage v depends only on the virtual resistance w and the phase shift δ (controller states) and makes use of the rated value E^* of the voltage. The new structure of the controller ensures that the maximum power capacity of the inverter is utilized under faults and facilitates a rigorous stability analysis, as shown in the subsection that follows, which represent two of the key contributions of this control scheme.

4.2.3 Stability Analysis

4.2.3.1 Current-limiting property

By applying the proposed controller (4.2) into the original system dynamics (4.1) and assuming grid-connected operation where $v_o = v_c$, the closed-loop dynamics of the inverter current become

$$L\frac{di}{dt} = -ri - \frac{(w - w_m)^2}{\Delta w_m^2} wi + \frac{(w - w_m)^2}{\Delta w_m^2}\sqrt{2}E^* \sin(\omega_g t + \delta). \tag{4.7}$$

For system (4.7), consider the continuous differentiable function V representing the energy stored in the inductor L, i.e.

$$V = \frac{1}{2}Li^2. \tag{4.8}$$

Since $w \in [w_{min}, w_{max}] > 0$ for all $t \geq 0$ according to the boundedness property of the generalized BIC explained above, the time derivative of V is calculated as

$$\begin{aligned}
\dot{V} &= -ri^2 - \frac{(w - w_m)^2}{\Delta w_m^2} wi^2 + \frac{(w - w_m)^2}{\Delta w_m^2}\sqrt{2}E^* i \sin(\omega_g t + \delta) \\
&\leq -ri^2 - \frac{(w - w_m)^2}{\Delta w_m^2} w_{min} i^2 + \frac{(w - w_m)^2}{\Delta w_m^2}\sqrt{2}E^* |i| |\sin(\omega_g t + \delta)| \\
&\leq -ri^2, \forall\, |i| \geq \frac{\sqrt{2}E^*}{w_{min}}.
\end{aligned}$$

Thus, according to the Theorem 2 in sec. 3.2, which is analytically given in [119], there exists a $\mathcal{KL}$ function β so that for any initial condition $i\,(0)$, there is a $T \geq 0$ such that

$$\begin{aligned}
&|i\,(t)| \leq \beta\,(|i\,(0)|\,, t) \quad \forall 0 \leq t \leq T \\
&|i\,(t)| \leq \frac{\sqrt{2}E^*}{w_{min}} \qquad\quad \forall t \geq T,
\end{aligned}$$

proving that the solution of the inverter current is uniformly ultimately bounded. Note that if initially $|i\,(0)| \leq \frac{\sqrt{2}E^*}{w_{min}}$, then $T = 0$, i.e. it holds true that

$$|i(t)| \leq \frac{\sqrt{2}E^*}{w_{min}}, \forall t \geq 0. \tag{4.9}$$

Since w_{min} is linked to the controller parameters ($w_{min} = w_m - \Delta w_m$), which are designed by the user, then by selecting

$$w_{min} = \frac{E^*}{I_{max}} \tag{4.10}$$

it yields

$$|i(t)| \leq \sqrt{2} I_{max}, \forall t \geq 0. \tag{4.11}$$

The previous inequality holds for any $t \geq 0$ and for any constant positive I_{max}. As a result

$$I \leq I_{max}, \forall t \geq 0, \tag{4.12}$$

where I is the RMS value of the inverter current, showing that the proposed controller introduces a current-limiting property below a given value I_{max}, that can be selected by the control operator. Since inequalities (4.9) and (4.12) do not depend on the grid voltage or frequency, i.e. V_g or ω_g, it is clear that the proposed controller can limit the RMS value of the current under I_{max} irrespectively of grid variations or faults, thus utilizing the maximum power capacity of the inverter at all times. This is a significant advantage compared to the original CLD.

4.2.3.2 Asymptotic stability

In sec. 4.2.3.1, the dynamic model (4.1) was used to prove the desired current limitation for the instantaneous value of the current, irrespective of the functions $f(P_g, V_g)$ and $g(Q_g, \omega_g)$; hence, the current-limiting property holds at all times, even during transients. However, to investigate whether the closed-loop system can regulate the real and reactive power or operate under the droop control mode, the functions $f(P_g, V_g)$ and $g(Q_g, \omega_g)$ should be considered in the analysis.

Note that for a single-phase inverter, the P_g and Q_g expressions represent the average real and reactive power of the inverter. Hence, as it is shown in [102, 103, 121], in order to analyze the stability of a droop-controlled single-phase inverter, the expressions of P_g and Q_g that use the RMS voltages and the power angles, i.e. the phasor voltages, should be utilized. This approach can be used in this work since the inverter frequency does not introduce additional dynamics due to the utilization of the PLL to obtain ω_g (PLL response is much faster than the inverter and droop control dynamics [122] and hence the phasor analysis makes sense).

As it can be seen from (4.7), the dynamics of the inverter current, when grid-connection has been achieved, are partially decoupled from the capacitor voltage and grid current dynamics due to the feed-forward term v_o used in (4.2). Thus, the equivalent circuit of the grid-connected inverter takes the form shown in Fig. 4.3. Here,

$$\boldsymbol{V}_{eq} = -jX_C \boldsymbol{I}$$

where $X_c = \frac{1}{\omega_g C}$ and

$$\boldsymbol{I} = \frac{E^* \frac{(w-w_m)^2}{\Delta w_m^2} \angle \delta}{\frac{(w-w_m)^2}{\Delta w_m^2} w + r + j\omega_g L}.$$

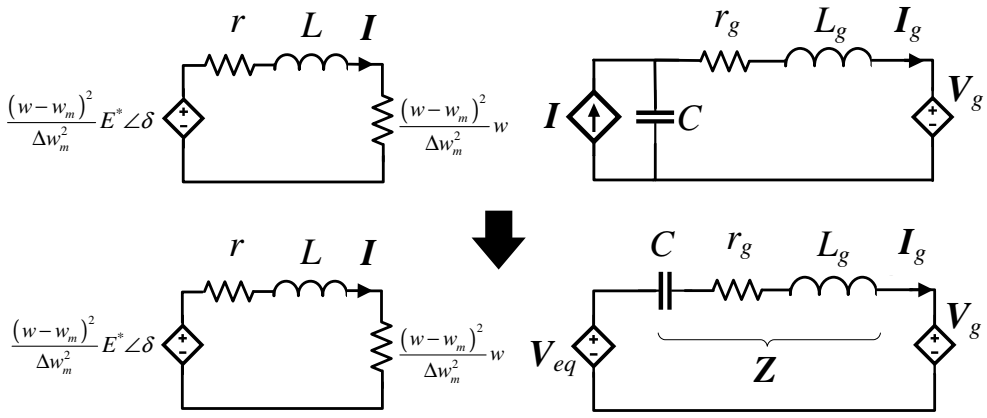

Figure 4.3: Equivalent circuit of the closed-loop system

Considering that $\boldsymbol{V}_g = V_g\angle 0^o$, then the real and reactive power delivered at the grid are given from the following expressions explained in [121] and [123]:

$$P_g = -\frac{V_g^2}{Z}cos\left(\theta_Z\right) + \frac{V_g E^*\left(w-w_m\right)^2 X_c}{\Delta w_m^2\sqrt{\left(\frac{(w-w_m)^2}{\Delta w_m^2}w+r\right)^2+\left(\omega_g L\right)^2 Z}}cos(\varphi) \tag{4.13}$$

$$Q_g = -\frac{V_g^2}{Z}sin\left(\theta_Z\right) - \frac{V_g E^*\left(w-w_m\right)^2 X_c}{\Delta w_m^2\sqrt{\left(\frac{(w-w_m)^2}{\Delta w_m^2}w+r\right)^2+\left(\omega_g L\right)^2 Z}}sin(\varphi)\,, \tag{4.14}$$

with $\mathbf{Z} = Z\angle\theta_Z = \sqrt{r_g^2+\left(\omega_g L_g - \frac{1}{\omega_g C}\right)^2}\angle tan^{-1}\left(\frac{\omega_g L_g - \frac{1}{\omega_g C}}{r_g}\right)$ and $\varphi = \delta - tan^{-1}\left(\frac{\omega_g L}{\frac{(w-w_m)^2}{\Delta w_m^2}w+r}\right) - \theta_Z - \frac{\pi}{2}$. Since δ is bounded, i.e. $\delta \in [-\Delta\delta_m, \Delta\delta_m]$, then φ is also bounded and can take positive or negative values to allow the inverter to inject or receive reactive power from the grid. Thus, without loss of generality, we can assume that $\varphi \in \left(-\frac{\pi}{2}, \frac{\pi}{2}\right)$ and $\omega_g^2 L_g C < 1$.

The closed-loop dynamics for the stability analysis can be obtained by combining (4.3)-(4.6) with (4.13)-(4.14) and the state vector is given as $x = [w\, w_q\, \delta\, \delta_q]^T$. Note that by considering constant V_g and ω_g (not necessarily equal to their rated values), an equilibrium point $x_e = [w_e\, w_{qe}\, \delta_e\, \delta_{qe}]^T$ of the closed-loop system can be obtained. Hence, the stability properties of the grid-connected inverter under the proposed enhanced CLD are summarized in the following proposition.

Proposition 1: Every equilibrium point $x_e = [w_e\, w_{qe}\, \delta_e\, \delta_{qe}]^T$ of the closed-loop system obtained by (4.3)-(4.6) and (4.13)-(4.14), with $w_e \in \left(w_{min}, \frac{w_m}{3}\right)$ and $\delta_e \in (-\Delta\delta_m, \Delta\delta_m)$ is asymptotically stable when $\Delta\delta_m$ is selected as

$$\Delta\delta_m = \min\left\{\left|\max\left\{0, \frac{\pi}{2} + \tan^{-1}\left(\frac{2\left((w_{min}+r)^2 + (\omega_g L)^2\right)}{\omega_g L\,(3w_{min} - w_m)} - \frac{w_{min}+r}{\omega_g L}\right)\right\} + \right.\right.$$
$$\left.\left. + \tan^{-1}\left(\frac{\omega_g L}{w_{min}+r}\right) + \theta_Z\right|, \pi + \tan^{-1}\left(\frac{27\omega_g L \Delta w_m^2}{4w_m^3 + 27\Delta w_m^2 r}\right) + \theta_Z\right\}. \quad (4.15)$$

Proof: Considering any equilibrium point $x_e = [w_e\, w_{qe}\, \delta_e\, \delta_{qe}]^T$ with $w_e \in \left(w_{min}, \frac{w_m}{3}\right)$ and $\delta_e \in (-\Delta\delta_m, \Delta\delta_m)$, the Jacobian matrix of the system takes the form

$$A = \begin{bmatrix} A_T & 0_{2x1} & 0_{2x1} \\ A_1 & -2k_w w_{qe}^{2l} & 0 \\ A_2 & 0 & -2k_\delta \delta_{qe}^{2l} \end{bmatrix},$$

where

$$A_T = \begin{bmatrix} -a\zeta\cos(\varphi_e) - \frac{a\omega_g L\psi\Delta w_m^2}{\varepsilon}\sin(\varphi_e) & -a\,(w_e - w_m)^2\sin(\varphi_e) \\ b\zeta\sin(\varphi_e) - \frac{b\omega_g L\psi\Delta w_m^2}{\varepsilon}\cos(\varphi_e) & -b\,(w_e - w_m)^2\cos(\varphi_e) \end{bmatrix}$$

with $\varepsilon = \left(\left(\frac{(w_e - w_m)^2}{\Delta w_m^2} w_e + r\right)^2 + (\omega_g L)^2\right)\Delta w_m^4$, $a = \frac{c_w n V_g E^* w_{qe}^{2l}}{\omega_g C\sqrt{\varepsilon} Z}$, $b = \frac{c_\delta m V_g E^* \delta_{qe}^{2l}}{\omega_g C\sqrt{\varepsilon} Z}$, $\psi = (w_e - w_m)^3\,(3w_e - w_m)$, $\gamma = \left(\frac{(w_e - w_m)^2}{\Delta w_m^2} w_e + r\right)\Delta w_m^2\psi$ and $\zeta = \frac{\gamma}{\varepsilon} - 2\,(w_e - w_m)$. Since $w_e \in \left(w_{min}, \frac{w_m}{3}\right)$ and $\delta_e \in (-\Delta\delta_m, \Delta\delta_m)$, then $w_{qe}, \delta_{qe} \in (0, 1]$ and therefore $-2k_w w_{qe}^{2l} < 0$ and $-2k_\delta \delta_{qe}^{2l} < 0$ (for details see [45]). Aiming to prove stability through Theorem 1 in sec. 3.1, the eigenvalues of A will have negative real parts if the eigenvalues of A_T have negative real parts. The characteristic polynomial that is derived from the characteristic equation $\det[\lambda I - A_T] = 0$ takes the form

$$\lambda^2 + \lambda\left(\left(b\,(w_e - w_m)^2 + a\zeta\right)\cos(\varphi_e) + \frac{a\omega_g L\psi\Delta w_m^2}{\varepsilon}\sin(\varphi_e)\right) + ab\zeta\,(w_e - w_m)^2 = 0.$$

Since $ab\zeta\,(w_e - w_m)^2 > 0$, then x_e is asymptotically stable if

$$\left(b\,(w_e - w_m)^2 + a\zeta\right)\cos(\varphi_e) + \frac{a\omega_g L\psi\Delta w_m^2}{\varepsilon}\sin(\varphi_e) > 0 \quad (4.16)$$

is satisfied. Since $\varphi_e \in \left(-\frac{\pi}{2}, \frac{\pi}{2}\right)$, then

$$\tan^{-1}\left(\frac{\omega_g L}{\frac{(w_e - w_m)^2}{\Delta w_m^2} w_e + r}\right) + \theta_Z < \delta_e < \pi + \tan^{-1}\left(\frac{\omega_g L}{\frac{(w_e - w_m)^2}{\Delta w_m^2} w_e + r}\right) + \theta_Z. \quad (4.17)$$

The term $b\left(w_e - w_m\right)^2 \cos(\varphi_e)$ is always positive and by substituting all the considered variables, (4.16) will hold true if

$$\tan(\varphi_e) > \frac{2\Delta w_m^2 \left(\left(\frac{(w_e - w_m)^2}{\Delta w_m^2} w_e + r \right)^2 + (\omega_g L)^2 \right)}{\omega_g L \left(w_e - w_m\right)^2 (3w_e - w_m)} - \frac{\left(\frac{(w_e - w_m)^2}{\Delta w_m^2} w_e + r \right)}{\omega_g L} \tag{4.18}$$

yielding

$$\delta_e > \tan^{-1}\left(\frac{\omega_g L}{\frac{(w_e - w_m)^2}{\Delta w_m^2} w_e + r} \right) + \theta_Z + \frac{\pi}{2} +$$

$$+ \tan^{-1}\left(\frac{2\Delta w_m^2 \left(\left(\frac{(w_e - w_m)^2}{\Delta w_m^2} w_e + r \right)^2 + (\omega_g L)^2 \right)}{\omega_g L \left(w_e - w_m\right)^2 (3w_e - w_m)} - \frac{\left(\frac{(w_e - w_m)^2}{\Delta w_m^2} w_e + r \right)}{\omega_g L} \right). \tag{4.19}$$

By combining inequalities (4.17) and (4.19), the condition that δ_e needs to satisfy in order to guarantee asymptotic stability becomes

$$\max\left\{ 0, \frac{\pi}{2} + \tan^{-1}\left(\frac{2\Delta w_m^2 \left(\left(\frac{(w_e - w_m)^2}{\Delta w_m^2} w_e + r \right)^2 + (\omega_g L)^2 \right)}{\omega_g L \left(w_e - w_m\right)^2 (3w_e - w_m)} - \frac{\left(\frac{(w_e - w_m)^2}{\Delta w_m^2} w_e + r \right)}{\omega_g L} \right) \right\} +$$

$$+ \tan^{-1}\left(\frac{\omega_g L}{\frac{(w_e - w_m)^2}{\Delta w_m^2} w_e + r} \right) + \theta_Z < \delta_e < \pi + \tan^{-1}\left(\frac{\omega_g L}{\frac{(w_e - w_m)^2}{\Delta w_m^2} w_e + r} \right) + \theta_Z. \tag{4.20}$$

Since $w_e \in \left(w_{min}, \frac{w_m}{3} \right)$, then (4.20) will be always satisfied if the following condition holds:

$$\max\left\{ 0, \frac{\pi}{2} + \tan^{-1}\left(\frac{2\left((w_{min} + r)^2 + (\omega_g L)^2 \right)}{\omega_g L \left(3w_{min} - w_m\right)} - \frac{w_{min} + r}{\omega_g L} \right) \right\} + \tag{4.21}$$

$$\tan^{-1}\left(\frac{\omega_g L}{w_{min} + r} \right) + \theta_Z < \delta_e < \pi + \tan^{-1}\left(\frac{27\omega_g L \Delta w_m^2}{4w_m^3 + 27\Delta w_m^2 r} \right) + \theta_Z,$$

where $w_{min} = \frac{E^*}{I_{max}}$ according to (4.10) and $w_m = w_{min} + \Delta w_m$. Taking into account that $-\Delta\delta_m < \delta_e < \Delta\delta_m$ from the proposed controller dynamics and $w_e \in \left(w_{min}, \frac{w_m}{3} \right)$, then if $\Delta\delta_m$ is selected from (4.15), it is concluded that (4.21) is always satisfied guaranteeing asymptotic stability for the considered equilibrium point x_e.

Remark 1: Compared to the existing approaches that consider the assumption of small power angle to guarantee stability [67], here the bound for the phase shift δ is guaranteed via the control design and does not represent an assumption.

For typical values of L, E^* and I_{max} in low power-rating grid-connected inverter applications, where also small parasitic resistances r and r_g are considered, the term $\frac{2\left((w_{min}+r)^2+(\omega_g L)^2\right)}{\omega_g L(3w_{min}-w_m)} - \frac{w_{min}+r}{\omega_g L}$ takes small values and $\theta_Z \approx -\frac{\pi}{2}$. Therefore, from (4.15), it is clear that $\Delta\delta_m$ can be simply selected as $\Delta\delta_m = \frac{\pi}{2}$. In practice, a slightly lower value than $\frac{\pi}{2}$ can be used to compensate the very small terms $\tan^{-1}\left(\frac{\omega_g L}{w_{min}+r}\right)$ and $\tan^{-1}\left(\frac{27\omega_g L\Delta w_m^2}{4w_m^3+27\Delta w_m^2 r}\right)$. However, for inverters with higher power ratings, the original expression (4.15) should be used to realize $\Delta\delta_m$.

Remark 2: Proposition 1 shows that asymptotic stability is guaranteed for any equilibrium point where $w_e \in \left(w_{min}, \frac{w_m}{3}\right)$. This corresponds to the range of the inverter RMS current $3I_m < I_e < I_{max}$, i.e. $\frac{3\omega_g C V_g}{\sqrt{\left(1-\omega_g^2 LC\right)^2+(r\omega_g C)^2.}} < I_e < I_{max}$, which shows that the smaller the filter capacitor C the largest the operating range for the inverter current with guaranteed asymptotic stability.

4.2.4 Voltage support capability under grid faults

As proven in sec. 4.2.3.1, the maximum power capability of the inverter can be now utilized with the proposed controller. Thus, inspired by the FRT requirements that have been proposed for DERs connected to the transmission and distribution networks, the proposed controller can be extended to provide support to the grid voltage under faults. As showcased in different FRT applications [2], voltage support is demanded when the voltage at the point of common coupling drops under 0.9 p.u. and it is practically accomplished through injection of reactive power. In order to introduce the voltage support mode (VSM) into the control design, expression (4.6) is proposed to take the form:

$$g(Q_g, a_f, \omega_g) = m(Q_g - a_f Q_{set} - (1-a_f)S_n) + a_f(\omega^* - \omega_g), \tag{4.22}$$

where a_f is a parameter defining whether VSM is enabled ($a_f = 0$) when $V_g < 0.9$ p.u., or disabled ($a_f = 1$) when $V_g \geq 0.9$ p.u.

As it was analytically explained in sec. 4.2.2, the phase shift δ in the proposed controller (4.2) is bounded in the range $\delta \in [-\Delta\delta_m, \Delta\delta_m]$ independently from the function $g(Q_g, a_f, \omega_g)$ in (4.4). Hence, when the phase shift δ reaches the upper or lower limit of its value ($\Delta\delta_m$ or $-\Delta\delta_m$), from (4.13) and (4.14), it is clear that $P_g = 0$ in both cases while the reactive power becomes $Q_g = -S_n$ and $Q_g = S_n$,

respectively, where S_n is the nominal apparent power of the inverter. This property, combined with the inherent current limitation, leads to the VSM of the proposed controller as explained below.

Considering a relatively stiff grid and a small voltage drop between the capacitor voltage V_c and the grid voltage V_g, which can be neglected, then it yields

$$S = V_c I \approx V_g I \leq E^* I_{max} = S_n. \tag{4.23}$$

This expression actually provides the selection of the maximum current I_{max}, when the nominal apparent power of the inverter is known, i.e. $I_{max} = \frac{S_n}{E^*}$.

However, under grid faults, the grid voltage V_g drops by a percentage p and then according to (4.23), the proposed controller limits the apparent power below $(1-p)V_g I_{max}$. When VSM is enabled, i.e. $p > 0.1$, then $\alpha_f = 0$ and according to (4.4) and (4.22), the dynamics of the phase shift δ become

$$\dot{\delta} = c_\delta m(Q_g - S_n)\delta_q^{2l}. \tag{4.24}$$

Since the apparent power S of the inverter is limited below $(1-p)V_g I_{max}$ due to the current-limiting property, then in (4.24) there is

$$\dot{\delta} = c_\delta m(Q_g - S_n)\delta_q^{2l} \leq c_\delta m((1-p)V_g I_{max} - E^* I_{max})\delta_q^{2l} < 0.$$

This means that the phase shift δ will keep decreasing and since $\delta \in [-\Delta\delta_m, \Delta\delta_m]$, due to the bounded control structure of (4.4), there is $\delta \to -\Delta\delta_m$. This means that $Q_g \to Q_e = (1-p)E^* I_{max} < S_n$, i.e. the reactive power will be regulated to the maximum apparent power under the grid voltage drop. Obviously, the real power will automatically converge to zero since

$$P_g \to P_e = \sqrt{((1-p)E^* I_{max})^2 - Q_e^2} = 0.$$

This property indicates that opposed to existing algorithms that change both the real and reactive power references during faults [30, 33], the proposed controller requires only a change in the phase shift dynamics of δ which are related to the reactive power while the real power will automatically drop to zero to allow maximum reactive power injection with an inherent current limitation and support the grid voltage. Furthermore, the change of the value of a_f during grid faults, changes only the function $g(Q_g, a_f, \omega_g)$ that is being integrated, while in conventional approaches the controller switches between dynamic controllers. Hence, the proposed controller keeps a unified structure with the same dynamic states at all times.

Table 4.1: System and controller parameters for comparative results

Parameters	Values	Parameters	Values
L, L_g	2.2 mH	ω^*	2π x 50 rad/s
r, r_g	0.5 Ω	ω_g	2π x 49.98 rad/s
C	10 μF	I_{max}	8 A
E^*	110 V	w_m	318.25 Ω
S_n	880 VA	Δw_m	304.5 Ω
c_w	348	K_e	10
c_δ	15.7	k_w, k_δ	1000
n	0.0625	m	0.0036

4.2.5 Comparative simulation results

In order to verify the desired operation of the proposed controller, a grid-connected single-phase inverter is simulated in Matlab/Simulink under normal and faulty grid conditions, since the implementation of the FRT algorithm in single-phase systems has shown an increasing interest recently [22, 23]. The power system and controller parameters are shown in Tab. 4.1. The controller parameters are selected according to the analysis in [45] and the stability condition of sec. 4.2.3.2. Note that under the specific parameters of Tab. 4.1, one could further perform a root-locus analysis of the linearized system, to select the gains c_w, c_δ, based on the desired performance metrics. Both the original CLD and the enhanced CLD schemes are investigated under the same scenario, while for the enhanced CLD scheme, the VSM is enabled. The inverter is connected to the grid at 0.1 s. Initially, P_{set} is set to 150 W, and Q_{set} is set to 0 Var, while at 0.6 s, the real power reference changes to 300 W and the reactive power reference increases to 200 Var. As it is shown in Fig. 4.4, both the original and the enhanced CLD lead the real and the reactive power of the inverter to the desired values. The real power and reactive power droop control functions are enabled at 1 s, and it is clear that both the real and the reactive power drop since the output voltage is above the rated value and the grid frequency ω_g is slightly below the rated frequency ω^*. Until this point, the responses of the original and the enhanced CLD are identical, proving that the proposed version maintains the original CLD behavior under a normal grid.

To investigate the controller performance under a faulty grid, at 2 s, a voltage sag occurs and the grid voltage drops by 0.3 p.u., while the fault is self-cleared at 2.3 s. As shown in Fig. 4.4a, when the enhanced CLD controller with the VSM enabled is adopted, the active power reduces during the fault, opposed to the original CLD. In particular, due to the current-limiting property of the proposed controller and the fact that reactive power is being increased in order to reach S_n, as shown in Fig. 4.4b, the real power automatically drops to zero. The support to the PCC voltage is clear in Fig. 4.4c, where it is observed that the RMS output voltage under the enhanced CLD scheme is higher than the one with the original CLD. The reason

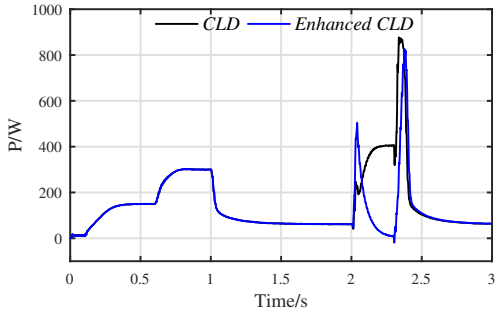

(a) Real power

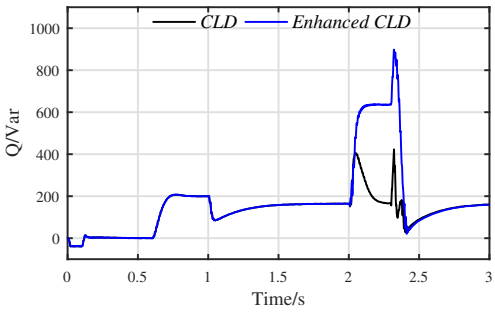

(b) Reactive power

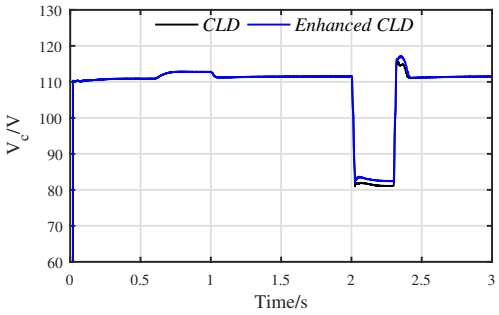

(c) RMS output voltage

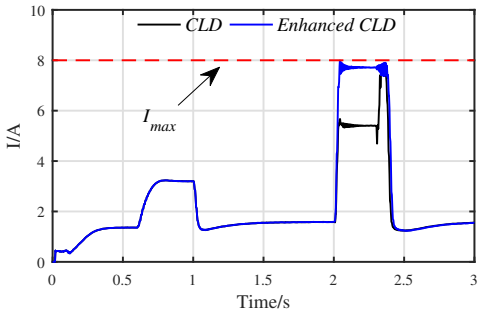

(d) RMS inverter current

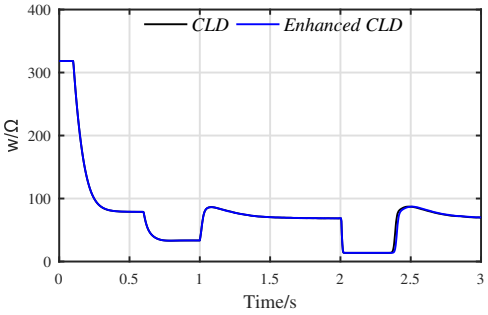

(e) Controller state w

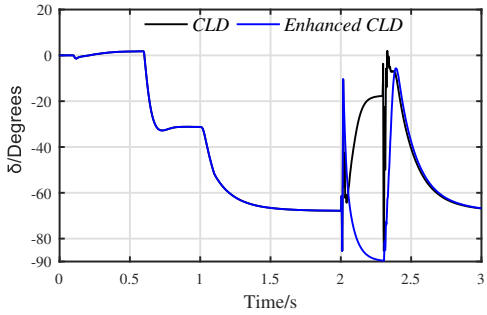

(f) Controller state δ

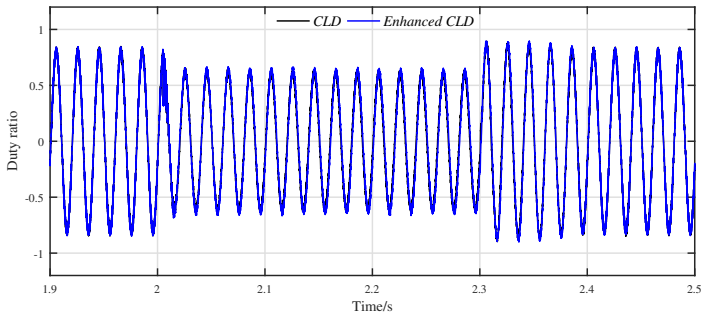

(g) Normalized inverter voltage during the fault

Figure 4.4: Simulation results of a grid-connected inverter equipped with the enhanced CLD with VSM enabled, compared to the original CLD

for the improved voltage support provision is that the current with the enhanced CLD reaches its maximum value, while the original CLD limits the current to a lower value that corresponds to the percentage of the voltage drop, as it is observed in Fig. 4.4d. This clearly indicates the ability of the proposed controller to fully utilize the maximum capacity of the inverter. Furthermore, the maximization of the reactive power rather than the real power, further improves the voltage support operation. The time response of the controller states w and δ are given in Fig. 4.4e and Fig. 4.4f, respectively. Since the dynamics of w are the same in both controllers, it is obvious that the response of w is identical in both scenarios. However, the phase shifting δ differs, since in the case of the enhanced CLD with VSM enabled it tends to -90^o during the fault in order to maximize the injection of the reactive power. Finally, in Fig. 4.4g, the inverter duty ratio (which results from the inverter voltage v divided by the dc voltage) is depicted during the grid fault. It can be observed that the duty ratio always stays inside the linear region of the PWM modulator (i.e. $[-1, 1]$). Moreover, with the enhanced CLD controller, the amplitude and the phase shift of the duty ratio are modified according to the different real and reactive power injections.

4.2.6 Experimental Validation

Table 4.2: System and controller parameters for experimental results

Parameters	Values	Parameters	Values
L	7 mH	ω^*	2π x 50 rad/s
L_g	6 mH	l	1
r	0.5 Ω	r_g	0.5 Ω
C	11 μF	I_{max}	3 A
E^*	110 V	w_{min}	36.66 Ω
S_n	330 VA	Δw_m	531.66 Ω
c_w	380	K_e	10
c_δ	20	k_w, k_δ	1000
n	0.1667	m	0.0095

To experimentally verify the proposed control approach, a single-phase inverter with rated power $S_n = 330$ VA was tested using a modified version of the Texas Instrument (TI) Development Kit HV DC/AC Solar Inverter connected to a Chroma 61830 Regenerative Grid Simulator. The system and controller parameters are shown in Tab. 4.2. A sinusoidal tracking algorithm PLL was used to obtain the required ω_g. The inverter switching frequency was 15 kHz while the proposed controller was implemented using a F28M35H52C1 DSP with a sampling frequency of 4 kHz. A lower sampling frequency was selected, as commonly done when implementing the power control loops for inverter applications. For the droop functions, it is expected that at

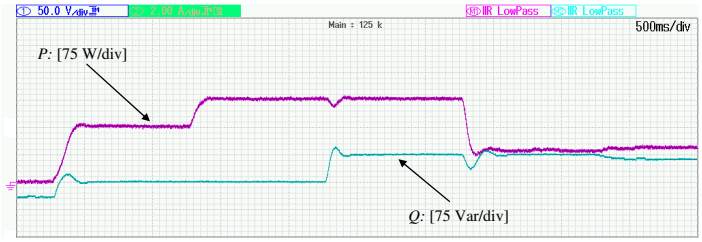

Figure 4.5: Operation under normal grid conditions

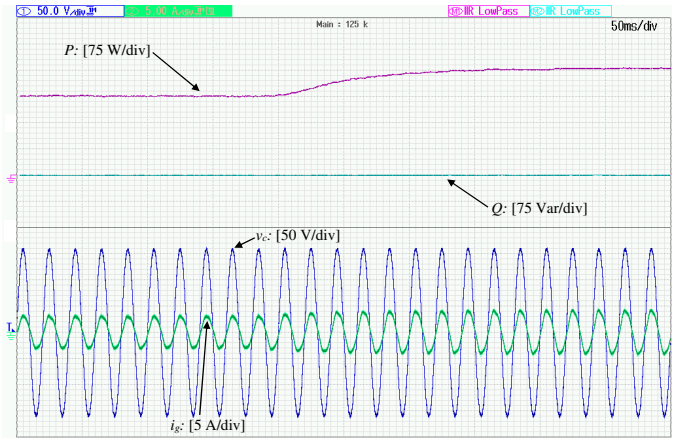

Figure 4.6: Transient response when P_{set} changes from 225 W to 350 W and $Q_{set} = 0$ (current-limiting property)

the nominal power S_n, a maximum of 5% deviation of the voltage and 1% deviation of the frequency is allowed [124]. Thus, since the $P \sim V$ and $Q \sim -\omega$ droop expressions are being used, the droop coefficients can be calculated as $n = \frac{0.05 K_e E^*}{S_n}$ for the real power droop and $m = \frac{0.01\omega^*}{S_n}$ for the reactive power droop, according to [79]. The real and reactive power is calculated using the measurements of the capacitor voltage v_c and the inverter current i, which are available at the TI inverter kit. For typical low-power inverter applications, the real and reactive power delivered to the grid (P_g and Q_g) are very close to the values of the real and reactive power delivered at the filter capacitor (P and Q), and hence P and Q can be used in the controller dynamics based on the measurements of v_c and i to simplify the implementation.

To verify both PQ-set control and PQ-droop control modes of the proposed controller, in Fig. 4.5 the following scenario is presented: At $t = 0.25$ s the inverter is connected to the grid and the real and reactive power reference values are set to 150 W and 0 Var, respectively. After 1 s, the real power reference is increased to 225 W and 1 s later the reactive power reference is increased to 75 Var. As it is shown in Fig. 4.5, both P and Q reach the desired values after a short transient. The real

power droop control is enabled after 1 s and the real power drops in order to bring the output voltage of the inverter closer to the rated value. Similarly, the reactive power droop control is enabled 1 s later and the injected reactive power drops since during that period the grid frequency was at 49.98 Hz, i.e. lower than the rated ω^*. In order to verify the current-limiting property ($I_{max} = 3$ A), in Fig. 4.6, the reference value of real power P_{set} is changed from 225 W to 350 W when the reactive power is zero. As it can be seen in Fig. 4.6, the RMS inverter current value is limited to almost 3 A and hence, the output real power is limited to slightly below 330 W, which corresponds to S_n for $Q = 0$. Thus, it is validated that the proposed controller protects the inverter from unrealistic power reference values. It is noteworthy that a THD around 5% is present at the grid current waveform. This can be a result of imperfect LCL filter design or sampling issues. Note that when a lower THD is required, inner current and voltage control loops can be also considered. Nevertheless, inner loop controllers were not considered in the proposed controller implementation, since the main goal of this section is to propose the enhanced CLD controller and rigorously prove its theoretical current-limiting and stability properties for first time.

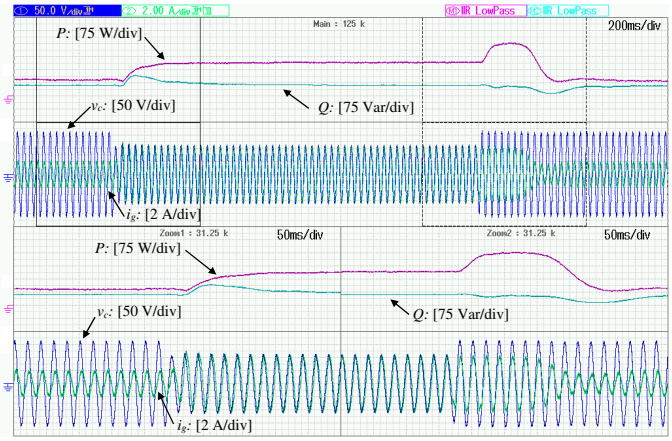

Figure 4.7: Operation under 37% drop of the grid voltage (110 V → 70 V)

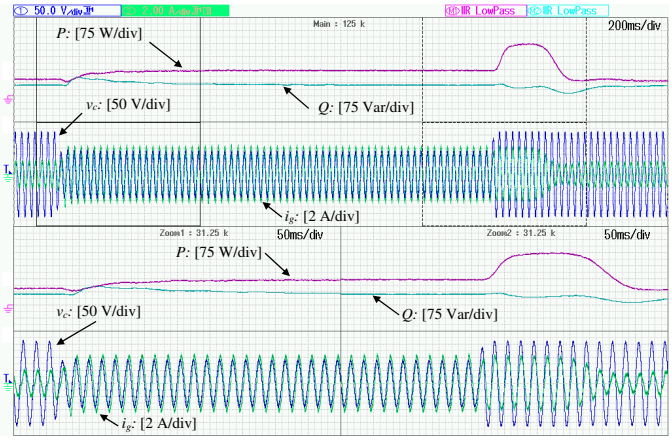

Figure 4.8: Operation under 50% drop of the grid voltage (110 V → 55 V)

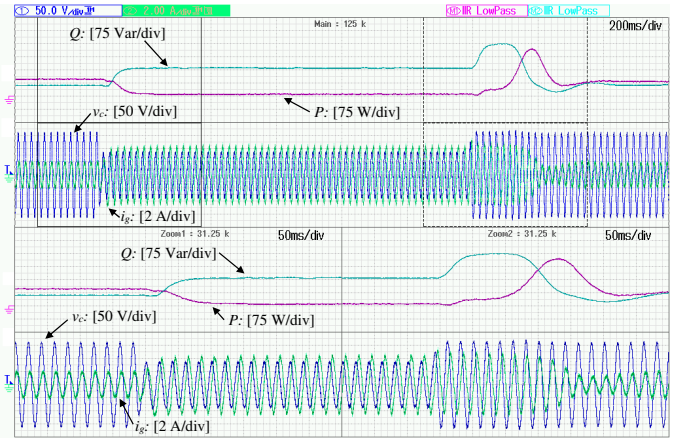

Figure 4.9: Operation under 50% drop of the grid voltage (110 V → 55 V) with voltage support enabled

In order to test the proposed controller efficacy under grid faults, in Fig. 4.7, a drop of the grid voltage from the nominal value (110 V) to 70 V is applied at 340 ms. Due to the voltage drop, the real power increases and the current reaches its upper limit, leading the real power to its steady-state value $P_e = \sqrt{(1-\rho)^2 S_n^2 - Q_e^2} = \sqrt{0.63^2 330^2 - 62^2}\,\mathrm{W} = 198\,\mathrm{W}$. When the fault is cleared, both the real and reactive power return to their original values according to the droop control after a short transient. One can see that during this short transient, the voltage returns to its nominal value instantly while the current remains at its maximum value for a short period of time. Hence, as it is depicted in Fig. 4.7, the apparent power is driven from the maximum available power during the fault to S_n, for a short time before returning to its original value, however it never exceeds S_n as required. At the bottom part of Fig. 4.7, the instances when the fault occurs and is being cleared are presented, where it can be clearly observed that the current remains below its maximum value during transients as well. A similar response is observed for a voltage drop of 50% of the nominal voltage in Fig. 4.8. Compared to the original CLD in [45], where the inverter current is limited to lower values under faults ($I_e \leq (1-\rho)\, I_{max}$), here, the proposed controller leads the inverter current to almost $I_{max} = 3\,\mathrm{A}$; thus utilizing the maximum power capacity of the inverter.

Since the maximum power utilization is now verified under grid faults, the voltage support mode can be enabled in the control system, as explained in sec. 4.2.4. As it was discussed in chapter 2, even if the voltage support operation based on FRT requirements is mainly applied to three-phase inverters for MV and HV grids, very recently, the voltage support capability has shown increased interest for single-phase inverters connected to the LV grid as well [22]. The scenario of a 50% voltage drop

is again tested while the inverter operates in the PQ-droop mode. As illustrated in Fig. 4.9, when the voltage sag occurs, the VSM algorithm is enabled and reactive power is maximized to support the voltage, while real power drops automatically to values close to 0 W, as described in sec. 4.2.4. As it can be observed in Fig. 4.9, when the fault is cleared, the real and reactive powers return to their original values. Note that the inverter current reaches the upper limit during the fault but never violates it, even during transients, as rigorously proven by the nonlinear ultimate boundedness theory in sec. 4.2.3.1.

4.3 Enhanced CLD control with self-synchronization and virtual inertia properties

In the previous section, a novel enhanced version of the CLD controller for grid-tied inverters was proposed to guarantee the maximum power injection during grid faults and closed-loop system stability. In this section, motivated by the recently developed self-synchronization methods, a new CLD structure is proposed which can remove the PLL device and at the same time introduce a virtual inertia property to the grid-connected inverter. Additionally, the proposed structure inherits the bounded integral controller [56] in order to guarantee tight bounds for the inverter frequency, as required by the Grid Code. At the same time, it is proven that the proposed controller maintains the advanced current-limiting capability of the enhanced CLD scheme of the previous section. Finally, the effect of the output filter to the closed-loop system is also investigated under the proposed controller.

4.3.1 The proposed controller design

In Fig. 4.10, the proposed self-synchronized current-limiting droop controller is depicted, for the grid-connected inverter shown in Fig. 4.1 with the system dynamics (4.1). The proposed controller maintains the ability to utilize the maximum capacity of the inverter and takes the form

$$v = v_o + (1 - w_q^l)(\sqrt{2}E^* \sin\theta - wi), \tag{4.25}$$

where $l \geqslant 1 \in \mathcal{N}$ and w represents a dynamic virtual resistance which together with the controller state w_q, is given as

$$\dot{w} = -c_w f(P, V_C) w_q^2 \tag{4.26}$$

$$\dot{w}_q = \frac{c_w(w - w_m)w_q}{\Delta w_m^2} f(P, V_c) - k_w \left(\frac{(w - w_m)^2}{\Delta w_m^2} + w_q^2 - 1 \right) w_q \tag{4.27}$$

with

$$f(P, V_c) = n(P_{set} - P) + K_e(E^* - V_c). \tag{4.28}$$

Again, $w_m, \Delta w_m, c_w, k_w$ are positive constants with $w_m > \Delta w_m$.

The w, w_q dynamics introduce the $P \sim V$ droop function and similar to the analysis of the original CLD in [45], for initial conditions $w = w_m$ and $w_{q0} = 1$, there is $w \in [w_{min}, w_{max}] = [w_m - \Delta w_m, w_m + \Delta w_m] > 0$ and $w_q \in [0, 1]$ for all $t \geqslant 0$. For the calculation of the phase θ in (4.25), and consequently the frequency ω, a self-synchronization mechanism is adopted using a PI controller as shown in Fig. 4.10, motivated by the self-synchronized synchronverter [15]. In this way, the output voltage v_o in (4.25) can be initially applied to the inverter voltage and then, the dynamic part of the proposed control scheme $\left((1 - w_q^l)(\sqrt{2}E^* \sin\theta - wi)\right)$ can be enabled at the time that relays close, without requiring a PLL, to achieve a smooth connection. Moreover, since the frequency $f = \frac{\omega}{2\pi}$ is required to remain in a bounded range, eg. [49.5 Hz, 50.5 Hz] , in this control scheme, the BIC of [56] is used to replace the traditional integrator in the frequency dynamics. Since the BIC guarantees a bound for the frequency without any saturation units, it prevents integrator wind-up phenomena and instability in the frequency dynamics. Thus, the frequency dynamics take the form

$$\dot{\theta} = \omega \tag{4.29}$$

$$\dot{\omega} = u(t)\omega_q^2 \tag{4.30}$$

$$\dot{\omega}_q = -\frac{(\omega - \omega_n)\omega_q}{\Delta\omega_m^2} u(t) - k_\omega \left(\frac{(\omega - \omega_n)^2}{\Delta\omega_m^2} + \omega_q^2 - 1 \right) \omega_q \tag{4.31}$$

where $u(t)$ results from the inverse Laplace transformation of

$$u(s) = \frac{1}{J} \left(Q(s) - Q_{set} - \frac{1}{m}(\omega(s) - \omega_n - \omega_{PI}(s)) \right),$$

with

$$\omega_{PI}(s) = \frac{(K_P s + K_I)(\omega(s) - \omega_n)}{(m + K_P)s + K_I},$$

when S_Q is closed. Parameter k_ω is a positive constant, ω_n is the nominal angular frequency and $K_P, K_I > 0$ represent the proportional and integral gain of the PI controller. Additionally, $\Delta\omega_m$ is the maximum acceptable frequency derivation from the nominal value. For example, for a nominal frequency of 50 Hz with maximum deviation 0.5 Hz, there is $\omega_n = 100\pi$ rad/s and $\Delta\omega_m = \pi$ rad/s.

A significant difference that distinguishes the proposed controller with the original CLD [45] is the self-synchronization property in the frequency dynamics for the calculation of the phase θ, opposed to the original CLD which used a traditional PLL.

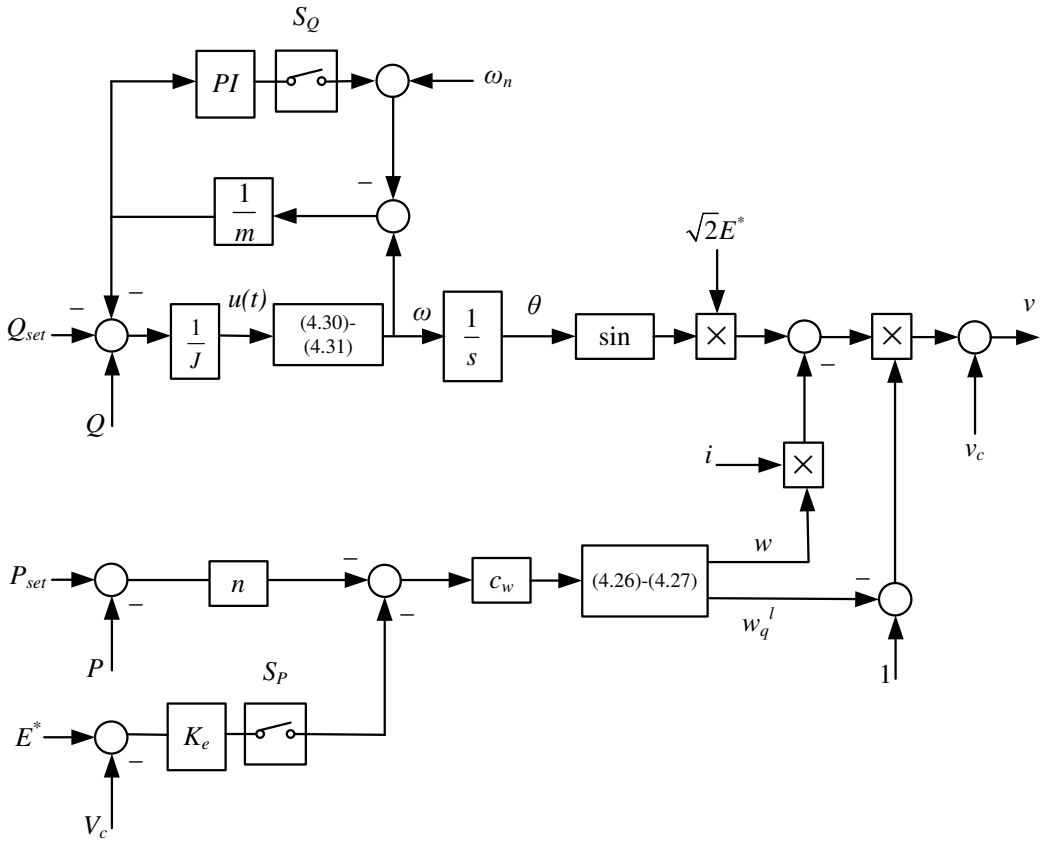

Figure 4.10: The proposed self-synchronized current-limiting droop controller

A second key difference is the use of the nominal voltage E^* in (4.25) instead of the grid voltage V_g, as in the enhanced CLD scheme of the previous section. Remember that the original CLD fails to utilize the maximum capacity of the inverter under faults, i.e. the inverter current is limited to a lower value depending on the grid voltage drop, which is a significant disadvantage in grid-connected units to support the grid under faulty conditions. The difference in the structure of (4.25) enables the current-limiting property with maximum capacity utilization as shown below.

4.3.2 Current-limiting property

By applying the proposed controller (4.25) into the grid-tied inverter dynamics (4.1), the dynamics of the inverter current take the form

$$L\frac{di}{dt} = -(r + (1 - w_q^l)w)i + (1 - w_q^l)\sqrt{2}E^* \sin\theta. \tag{4.32}$$

Following the analysis of the original CLD dynamics for w and w_q, it holds true (for details see [45]) that $w \in [w_{min}, w_{max}] > 0$, where $w_{min} = w_m - \Delta w_m$, $w_{max} =$

$w_m + \Delta w_m$, and $w_q \in [0, 1]$ for all $t \geq 0$. For system (4.32), let us consider the Lyapunov function candidate

$$V = \frac{1}{2} L i^2, \tag{4.33}$$

which actually represents the energy stored in the inductor L. Therefore, the time derivative of V becomes

$$\begin{aligned} \dot{V} &= -(r + (1 - w_q^l)w)i^2 + (1 - w_q^l)\sqrt{2}E^* i \sin\theta \\ &\leq -(r + (1 - w_q^l)w_{min})i^2 + (1 - w_q^l)\sqrt{2}E^* |i| \, |\sin\theta| \, . \end{aligned}$$

This shows that $\dot{V} \leq -ri^2$ when $|i| \geq \frac{\sqrt{2}E^*|\sin\theta|}{w_{min}}$, proving that (4.32) is input-to-state stable (ISS) assuming as input the expression $\sqrt{2}E^* \sin\theta$. Since this expression is bounded, then the inverter current i is bounded for all $t \geq 0$. According to the ISS property highlighted in sec. 3.3, it holds true that

$$|i| \leq \frac{\sqrt{2}E^*}{w_{min}}, \forall t \geq 0,$$

if initially $i(0)$ satisfies the previous inequality. Since w_{min} is one of the controller parameters ($w_{min} = w_m - \Delta w_m$), by selecting

$$w_{min} = \frac{E^*}{I_{max}} \tag{4.34}$$

where I_{max} is the maximum allowed RMS value of the inverter current, then

$$|i| \leq \sqrt{2} I_{max}. \tag{4.35}$$

The previous inequality holds for any $t \geq 0$ and for any constant positive I_{max}. As a result

$$I \leq I_{max}, \forall t \geq 0, \tag{4.36}$$

where I is the RMS value of the inverter current, showing that the proposed controller maintains the current-limiting property below a given value I_{max}. Since the closed-loop current equation (4.32) does not depend on the grid voltage v_g, then the current-limiting property holds independently from any grid voltage variations (eg. grid faults), similarly to the enhanced CLD of the previous section.

4.3.3 Effect of the LCL filter to the closed-loop system

LCL filters are widely used in inverter-interfaced DERs due to their ability to reduce the harmonic content resulting from the pulse width modulation. However, the main

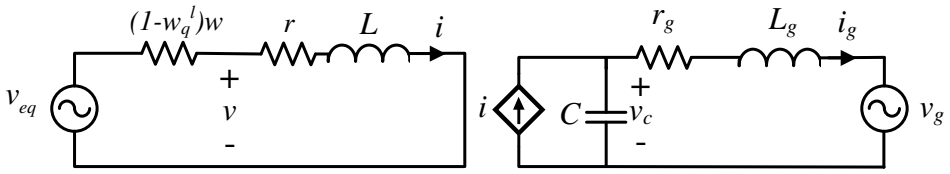

Figure 4.11: Equivalent circuit of the closed-loop system

drawback of these topologies is the high gain that they introduce at the resonance frequency [125]. Depending on the controller structure and dynamics, the closed-loop system may become unstable due to this resonance issue. In order to realize the effect of the LCL to the closed-loop system based on the proposed controller, the closed-loop system resulting from the combination of (4.1) and (4.25) with dynamics (4.26)-(4.31) is investigated. By replacing (4.25) into (4.1) the equivalent closed-loop circuit is shown in Fig. 4.11 where $v_{eq} = (1 - w_q^l)\sqrt{2}E^* \sin\theta$. Hence, the transfer functions from the voltage $v_{eq}(s)$ to the inverter current $i(s)$ and to the grid current $i_g(s)$ are

$$\frac{i(s)}{v_{eq}(s)} = \frac{1}{Ls + r + (1 - w_q^l)w} \tag{4.37}$$

and

$$\begin{aligned}\frac{i_g(s)}{v_{eq}(s)} = 1/\Big[&LL_gCs^3 + (r_gCL + L_gCr + L_gC(1 - w_q^l)w)s^2 + \\ &+ (L + rr_gC + r_gC(1 - w_q^l)w)s + r + (1 - w_q^l)w\Big].\end{aligned} \tag{4.38}$$

Since the values of w and w_q change during the inverter operation but remain bounded in a given range, both (4.37) and (4.38) represent a set of transfer functions. Given that w starts from the initial condition $w_o = w_m$ and can reach the minimum value w_{min} at the maximum current, then the bode diagrams of (4.37) and (4.38) are provided in Fig. 4.12a and Fig. 4.12b, respectively, for $w \in [w_{min}, w_m] = [w_m - \Delta w_m, w_m]$ and by neglecting r, r_g. Since from (4.27), w_q is restricted on the ellipse $\frac{(w-w_m)^2}{\Delta w_m^2} + w_q^2 = 1$ and $w_q \in [0, 1]$, then $w_q = \sqrt{1 - \frac{(w-w_m)^2}{\Delta w_m^2}}$ [45]. In the same figures, the open-loop transfer functions for an LCL filter are provided. Note that the parameters of Tab. 4.3 have been taken into account. In Fig. 4.12a, it is observed that considering the proposed controller dynamics, the resonance of the LCL filter is avoided. However, in Fig. 4.12b, for the transfer function $\frac{i_g(s)}{v_{eq}(s)}$, one can see that the resonance still exists with the proposed controller but with a limited value.

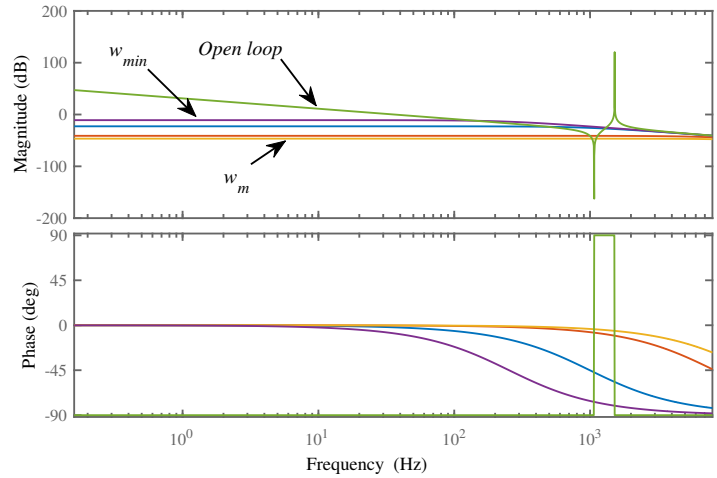

(a) Voltage to inverter current

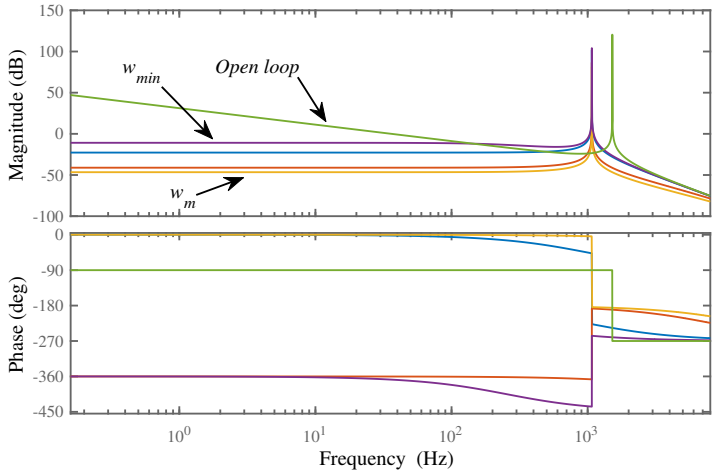

(b) Voltage to grid current

Figure 4.12: Effect of the LCL filter to the closed-loop system

4.3.4 Controller verification through simulation results

In order to verify the effectiveness of the proposed controller, a single-phase grid-connected inverter is simulated under both normal and faulty grid conditions. The parameters of the power and the control systems used for the simulations, are given in Tab. 4.3. The scenario is as follows: The inverter is connected to the grid at 0.1 s. Initially, the PQ-set control is enabled by setting the desired values of the real and reactive power. Particularly, the real power reference is set to 100 W and after 2 s changes to 500 W, while the reactive power reference is initially set to 0 Var and at 3 s changes to 50 Var, as shown in Fig. 4.13a and Fig. 4.13b. It is observed that both the real and the reactive power are regulated to their reference values after a short transient. At 4 s, the droop control for both the real and the reactive power is enabled by opening switch S_Q and closing switch S_P, and the real and reactive power injected

Table 4.3: System and controller parameters for simulation results

Parameters	Values	Parameters	Values
L, L_g	2.2 mH	ω_n	2π x 50 rad/s
r, r_g	0.5 Ω	ω_g	2π x 49.98 rad/s
C	10 μF	I_{max}	8 A
E^*	110 V	l	100
J	0.001 kg.m^2	w_m	318.25 Ω
S_n	880 VA	Δw_m	304.5 Ω
c_w	348	K_e	10
k_w	1000	k_ω	1000
n	0.0625	m	0.0036
K_P	0.1	K_I	1
$\Delta\omega_m$	π rad/s	t_s	0.05 s

to the grid change according to the droop expressions, as shown in Fig. 4.13a and Fig. 4.13b. At 7 s, a voltage drop of 0.3 p.u. occurs and lasts for 2.5 s in order to investigate a grid fault. Under this grid fault, the injected power to the grid remains limited (Fig. 4.13a and Fig. 4.13b) because as shown in Fig. 4.13d, the current-limiting property of the proposed controller maintains the RMS current under the maximum value. When the fault is self-cleared, both the real and the reactive power return to their original values. In Fig. 4.13e, the response of the controller state w is depicted and in Fig. 4.13f a comparison between the inverter frequency that is obtained via the self-synchronization process of the proposed controller and the grid frequency measured from a conventional PLL is illustrated. One can observe that the inverter equipped with the proposed self-synchronized CLD remains synchronized with the grid at all times and that the inverter frequency stays always inside the desired range $[49.5\,\text{Hz}, 50.5\,\text{Hz}]$, even during faults in the grid voltage. It should be noted that the conventional PLL is used only for comparison purposes and is not part of the proposed controller. Hence, the self-synchronization property of the proposed controller has been verified, proving that a PLL is not required for its operation. This brings significant advantages to the control system operation, due to the limitations that PLL devices introduce, as discussed in sec. 2.3.

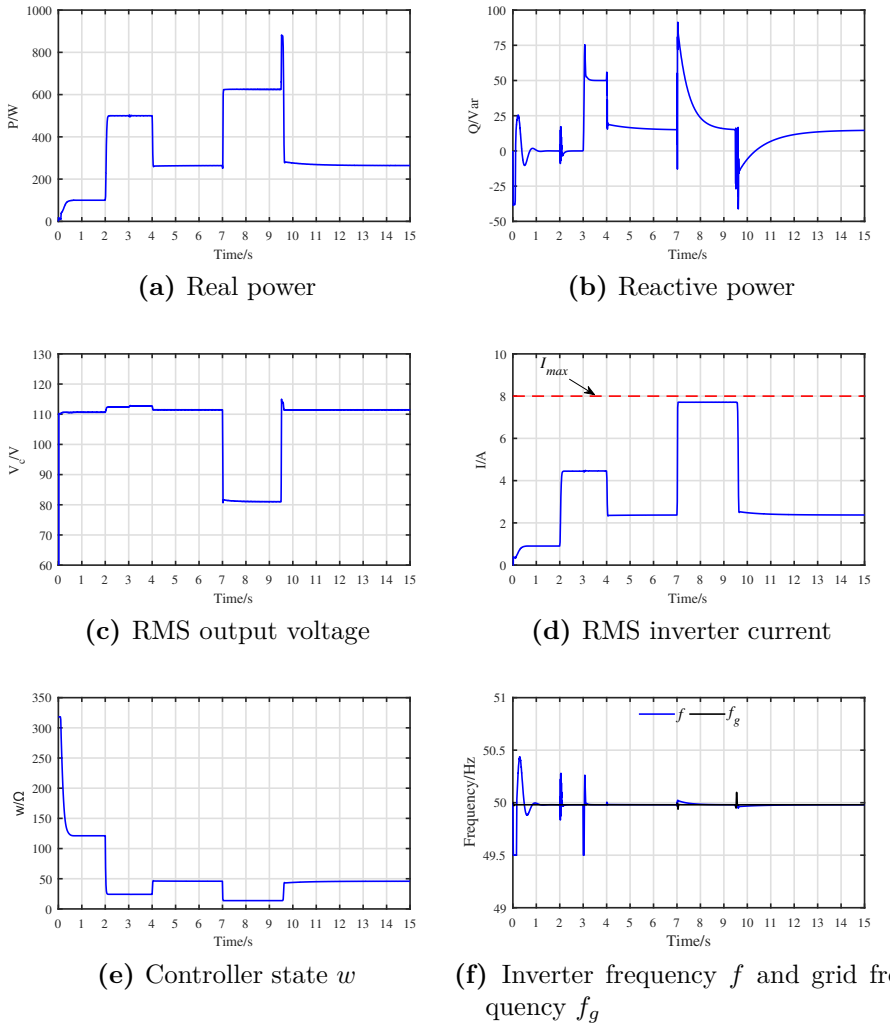

(a) Real power

(b) Reactive power

(c) RMS output voltage

(d) RMS inverter current

(e) Controller state w

(f) Inverter frequency f and grid frequency f_g

Figure 4.13: Simulation results of a grid-tied inverter operating under the proposed self-synchronized CLD controller

4.4 Conclusions

In this chapter, the concept of current-limiting droop control of grid-connected inverters was revisited and two advanced control schemes were proposed to address the limitations of the original CLD control scheme. Firstly, an enhanced CLD controller was proposed to guarantee the maximum power utilization during voltage drops and closed-loop system stability. It was analytically proven that the proposed controller can guarantee the desired current-limiting property at all times, even under transient phenomena, without using any saturation units or depending on the

system parameters. This current limitation was proven independently from the grid voltage variations; thus enabling maximum power utilization under grid faults. In addition, the asymptotic stability of any equilibrium point of the closed-loop system within a given operating range was proven for the first time with the proposed controller. Finally, since the maximum power capacity of the inverter (or equivalently the DER unit) can be utilized under faults, an extension of the proposed enhanced CLD was developed to provide voltage support under faults by injecting maximum reactive power (inspired by the FRT requirements). The efficacy of the proposed control approach was validated with comparative simulation results and extended experimental results for a grid-connected inverter under both normal and faulty grid conditions. In the sequel of this chapter, a modified version of the enhanced CLD controller was proposed, which inherits virtual inertia and self-synchronization properties to the grid-connected inverter, apart from the inherent current limitation and the maximum power utilization capabilities. Extended simulation results were presented to validate the self-synchronized enhanced CLD scheme.

5 Three-phase grid-connected inverters with inherent current-limiting capability

5.1 Motivation and novel outcome

In this chapter, the design of current-limiting control techniques for three-phase grid-connected droop-controlled inverters is investigated. Three-phase grid-connected inverter applications are of vital importance, since they enable the connection of DERs to the MV and HV power networks. Furthermore, a different modeling is required to represent the dynamics of a three-phase system, which usually employs a reference frame transformation. Moreover, the operation of three-phase inverters during grid faults is subject to more demanding requirements, compared to single-phase inverters. In particular, a challenging task in three-phase systems is how to deal with unbalanced grid faults from the control perspective. Particularly, in the context of current-limiting control techniques, the safe voltage support provision during unbalanced grid faults is a complicated problem. Note that most of the faults that appear in power systems are of unbalanced nature, and as the share of DERs is increasing, ancillary services like the voltage support of both the positive and the negative sequence voltages, will be required from DERs.

As it has already been highlighted, a novel current-limiting control technique has been proposed in [45] for single-phase grid-connected droop-controlled inverters. This technique inherits a current-limiting property into a droop controller without using saturation units, thus avoiding integrator wind-up and instability. Nevertheless, in order to extend this technique to three-phase inverter applications, the current-limiting droop control concept should be redesigned. As in the case of single-phase inverters in sec. 4.2, the resulting scheme should be capable to inject the maximum available power during faults in order to comply with the modern Grid Code requirements and provide voltage support. Note that as it was mentioned before, a challenge arises in optimizing the voltage support operation, while guaranteeing a safe current injection. More specifically, in the case of unbalanced grid faults, the inverter should accomplish both positive sequence voltage support and negative sequence voltage elimination, according to the "voltage support concept" [35], by injecting both positive and negative sequence currents.

To deal with the above stated challenges, in sec. 5.2, a novel current-limiting control scheme is proposed for three-phase grid-connected droop-controlled inverters, which uses the SRF model (dq model) to reduce the computational burden. A full model of the three-phase grid-connected inverter in the dq framework is obtained and the inherent current limitation is proven through nonlinear analysis of the closed-loop system. Furthermore, the proposed control design is shown to facilitate the investigation of asymptotic stability of the closed-loop system. In the sequel, in sec. 5.3, building on the previously developed control scheme, the fault-ride-through operation of three-phase inverters with inherent current-limiting characteristics is investigated, especially during unbalanced grid faults. Initially, the dq modeling of a three-phase grid-connected inverter is revisited in order to consider the existence of both positive and negative sequence components. Then, the control design is performed such that to combine a guaranteed current limitation and voltage support provision, when injecting both positive and negative sequence currents. Moreover, a novel method is proposed so that the maximum available current is divided into the two sequences, during unbalanced grid faults. Finally, asymptotic stability of the closed-loop system is proven with the proposed control scheme, regardless of the system parameters.

5.2 Current-limiting droop control of three-phase grid-connected inverters

5.2.1 System modeling in the SRF under balanced grid conditions

The system under consideration consists of a three-phase inverter connected to the grid through an LCL filter, as depicted in Fig. 5.1. The capacitors of the filter are denoted as C, while the inductances are denoted as L and L_g with parasitic resistances r and r_g, respectively. The line-to-line voltage between phases a and b is given as v_{iab}, while v_{ia} represents the phase voltage of the inverter. The capacitor voltage is denoted as v_{ca} and the grid voltage is v_a with $v_a = \sqrt{2}V_g \cos\omega_g t$, where V_g is the RMS grid voltage and ω_g is the angular grid frequency. The inverter and grid side currents are i_a and i_{ga} respectively. In order to obtain the dynamic model of the system, the widely used SRF theory is considered [48]. Although the clockwise SRF transformation from [1] is most commonly used with phase a aligned to the α axis, in this case, the generic $\alpha\beta$ transformation is taken into account as presented in [49]:

$$T_{\alpha\beta} = \frac{2}{3}\begin{bmatrix} \cos\theta_a & \cos(\theta_a - 120^o) & \cos(\theta_a + 120^o) \\ \sin\theta_a & \sin(\theta_a - 120^o) & \sin(\theta_a + 120^o) \\ 0.5 & 0.5 & 0.5 \end{bmatrix},$$

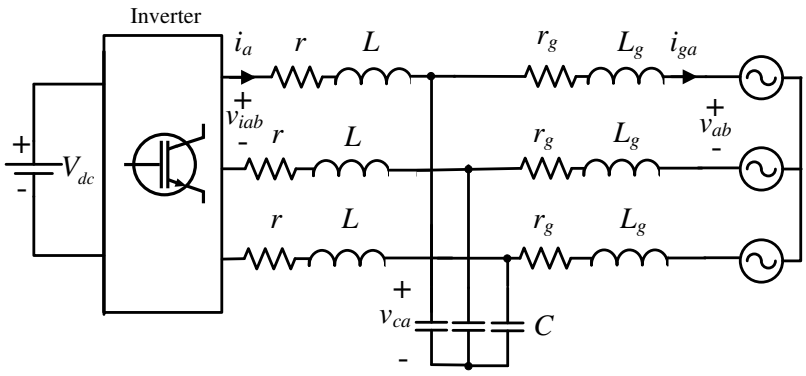

Figure 5.1: Three-phase inverter connected to the grid through an LCL filter

where θ_a is the angle between phase a and the α axis, followed by the rotating transformation

$$T_{dq} = \begin{bmatrix} \cos\theta_g & -\sin\theta_g \\ \sin\theta_g & \cos\theta_g \end{bmatrix},$$

with $\theta_g = \omega_g t$.

By applying the above transformations to the three-phase current and voltage quantities of the system, the SRF-based dynamic equations of the three-phase grid-tied inverter are obtained as

$$L\frac{di_d}{dt} = v_{id} - v_{cd} - ri_d - \omega_g L i_q \tag{5.1}$$

$$L\frac{di_q}{dt} = v_{iq} - v_{cq} - ri_q + \omega_g L i_d \tag{5.2}$$

$$L_g\frac{di_{gd}}{dt} = v_{cd} - v_d - r_g i_{gd} - \omega_g L_g i_{gq} \tag{5.3}$$

$$L_g\frac{di_{gq}}{dt} = v_{cq} - v_q - r_g i_{gq} + \omega_g L_g i_{gd} \tag{5.4}$$

$$C\frac{dv_{cd}}{dt} = i_d - i_{gd} - \omega_g C v_{cq} \tag{5.5}$$

$$C\frac{dv_{cq}}{dt} = i_q - i_{gq} + \omega_g C v_{cd}, \tag{5.6}$$

where v_{id} and v_{iq} are the dq-axis values of the inverter voltage and represent the control inputs of the system [126].

5.2.2 The proposed controller design

The proposed controller consists of an inner-loop voltage and current controller and an outer-loop power controller, which includes the droop control characteristics and inherently limits the grid current.

5.2.2.1 Inner-loop controller

The inner-loop current controller takes the form

$$\begin{aligned} v_{id} &= v_{cd} + \left(k_{PCC} + \frac{k_{ICC}}{s}\right)(i_d^{ref} - i_d) + \omega_g L i_q \\ v_{iq} &= v_{cq} + \left(k_{PCC} + \frac{k_{ICC}}{s}\right)(i_q^{ref} - i_q) - \omega_g L i_d, \end{aligned}$$

where PI controllers with decoupling and feed-forward terms are applied to regulate i_d to i_d^{ref} and i_q to i_q^{ref}. Similarly, the voltage controller from which i_d^{ref} and i_q^{ref} are obtained is described through the equations

$$\begin{aligned} i_d^{ref} &= i_{gd} + \left(k_{PVC} + \frac{k_{IVC}}{s}\right)(v_{cd}^{ref} - v_{cd}) + \omega_g C v_{cq} \\ i_q^{ref} &= i_{gq} + \left(k_{PVC} + \frac{k_{IVC}}{s}\right)(v_{cq}^{ref} - v_{cq}) - \omega_g C v_{cd}, \end{aligned}$$

where the reference values v_{cd}^{ref} and v_{cq}^{ref} are defined by the outer-loop power control.

As in typical multi-loop controller applications, the current controller is designed to settle much faster than the voltage controller which settles much faster than the power controller. In order to satisfy this, the parameters of the PI controllers can be suitably selected using the pole placement technique. Thus, for the power controller design, which operates in a slower time scale, it is reasonable to assume that v_{cd} and v_{cq} are quickly regulated to v_{cd}^{ref} and v_{cq}^{ref}. Further analysis about the inner-loop controllers commonly used in DERs applications can be found in [29].

5.2.2.2 The proposed droop controller

The outer-loop controller consists of a power controller which adopts droop control to support the grid. Following to the introduction of the inner-loop controller in sec. 5.2.2.1, the power controller will be directly applied to the capacitor voltage of the LCL filter through controlling the reference capacitor voltage values v_{cd}^{ref} and v_{cq}^{ref}. The proposed power controller for the grid-connected operation is described

by the equations

$$v_{cd}^{ref} = v_d + E_d^* - w_d i_{gd} + \omega_g L_g i_{gq} \tag{5.7}$$
$$v_{cq}^{ref} = v_q + E_q^* - w_q i_{gq} - \omega_g L_g i_{gd} \tag{5.8}$$

where v_d, v_q are the grid voltage dq components and w_d, w_q are the virtual resistances applied to each axis, which change according to the expressions

$$\dot{w_d} = -c_{wd} f(P) w_{dq}^2 \tag{5.9}$$
$$\dot{w_{dq}} = \frac{c_{wd}(w_d - w_m) w_{dq}}{\Delta w_m^2} f(P) - k_w \left(\frac{(w_d - w_m)^2}{\Delta w_m^2} + w_{dq}^2 - 1 \right) w_{dq}$$
$$\dot{w_q} = -c_{wq} g(Q) w_{qq}^2 \tag{5.10}$$
$$\dot{w_{qq}} = \frac{c_{wq}(w_q - w_m) w_{qq}}{\Delta w_m^2} g(Q) - k_w \left(\frac{(w_q - w_m)^2}{\Delta w_m^2} + w_{qq}^2 - 1 \right) w_{qq}$$

where c_{wd}, c_{wq}, k_w, w_m, Δw_m are positive constants and

$$f(P) = n(P_{set} - P) + K_e \left(E_{rms}^* - V_g \right) \tag{5.11}$$
$$g(Q) = m(Q_{set} - Q) - (\omega^* - \omega_g) \tag{5.12}$$

with E_d^* and E_q^* representing the nominal voltages on dq axes, K_e being a positive constant, E_{rms}^* is the RMS nominal voltage and m, n are the droop coefficients. The real and reactive power of the inverter are denoted as P and Q with their desired values P_{set} and Q_{set}, respectively. It should be noted that the $P \sim V$ and $Q \sim -\omega$ droop expressions of the universal droop controller are adopted here to provide robustness to different output impedances [79].

The PQ-set and PQ-droop control modes can be implemented in the control system through the functions (5.11)-(5.12). In these two control modes, the inverter is either tracking the reference values P_{set}, Q_{set}, when the terms $K_e \left(E_{rms}^* - V_g \right)$ and $\omega^* - \omega_g$ are removed from (5.11) and (5.12), respectively, or regulates to the grid voltage and frequency to support the grid. For the dynamics of the virtual resistances w_d and w_q in (5.7)-(5.8), the bounded integral controller, proposed in [56], is adopted in order to guarantee the boundedness of w_d and w_q without using any saturated integrators that could drive the system to instability. Hence, it is guaranteed that w_d, $w_q \in [w_{min}, w_{max}] > 0$, for all $t \geq 0$, where $\Delta w_m = \frac{w_{max} - w_{min}}{2}$ and $w_m = \frac{w_{min} + w_{max}}{2}$. For more details, the reader is referred to sec. 4.2 and to [56]. This design of bounded virtual resistance will lead to the desired grid current-limiting property, as it will be explained in the sequel. The implementation of the proposed control approach is depicted in Fig. 5.2.

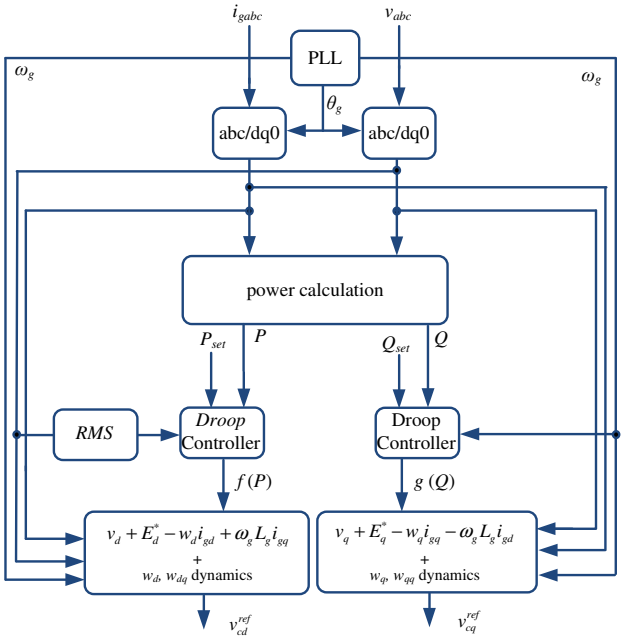

Figure 5.2: The proposed control scheme

5.2.3 Stability analysis

5.2.3.1 Current-limiting property

Taking into account the fast inner current and voltage control loops that regulate v_{cd} and v_{cq} to v_{cd}^{ref} and v_{cq}^{ref} in (5.3) and (5.4), by substituting the proposed controller equations (5.7) and (5.8) into the system dynamics (5.3)-(5.4), the closed-loop system can be obtained as

$$L_g \frac{di_{gd}}{dt} = E_d^* - w_d i_{gd} - r_g i_{gd} \tag{5.13}$$

$$L_g \frac{di_{gq}}{dt} = E_q^* - w_q i_{gq} - r_g i_{gq}. \tag{5.14}$$

The equations (5.13) and (5.14) are the derived dynamics of the grid current. Recall that for the controller dynamics w_d, w_{dq}, w_q, w_{qq} it holds true that $w_d, w_q \in [w_{min}, w_{max}] > 0$, where $w_{min} = w_m - \Delta w_m$, $w_{max} = w_m + \Delta w_m$, for all $t \geq 0$. Taking into account these properties, let us consider the Lyapunov function candidate

$$V = \frac{1}{2} L_g i_{gd}^2 + \frac{1}{2} L_g i_{gq}^2.$$

The time derivative of V, after substituting into its expression the dynamic equation

of the grid current, becomes

$$\begin{aligned}\dot{V} &= -r_g(i_{gd}^2 + i_{gq}^2) + \Big(i_{gd}(E_d^* - w_d i_{gd}) + i_{gq}(E_q^* - w_q i_{gq})\Big) \\ &\leq -(r_g + w_{min})(i_{gd}^2 + i_{gq}^2) + \begin{bmatrix} E_d^* & E_q^* \end{bmatrix} \begin{bmatrix} i_{gd} \\ i_{gq} \end{bmatrix} \\ &\leq -(r_g + w_{min}) \left\|i_g\right\|_2^2 + \left\|E^*\right\|_2 \left\|i_g\right\|_2,\end{aligned}$$

where $i_g = \begin{bmatrix} i_{gd} & i_{gq} \end{bmatrix}^T$ and $E^* = \begin{bmatrix} E_d^* & E_q^* \end{bmatrix}^T$. Hence,

$$\dot{V} \leq -r_g \left\|i_g\right\|_2^2, \forall \left\|i_g\right\|_2 \geq \frac{\left\|E^*\right\|_2}{w_{min}},$$

which means that the grid current dynamics system given by equations (5.13) and (5.14) is input-to-state stable (ISS) according to Theorem 3 in sec. 3.3, when the voltage vector E^* is considered as input. Since E_d^* and E_q^* represent constant values of the rated voltage then the grid currents i_{gd} and i_{gq} will be bounded for all $t \geq 0$.

Since $i_g = \begin{bmatrix} i_{gd} & i_{gq} \end{bmatrix}^T$ and $E^* = \begin{bmatrix} E_d^* & E_q^* \end{bmatrix}^T$, considering the relationship between the RMS value and the dq components, then

$$\begin{aligned}\left\|i_g\right\|_2 &= \sqrt{i_{gd}^2 + i_{gq}^2} = \sqrt{(\sqrt{2} I_{grms})^2} = \sqrt{2} I_{grms} \\ \left\|E^*\right\|_2 &= \sqrt{E_d^{*2} + E_q^{*2}} = \sqrt{(\sqrt{2} E_{rms}^*)^2} = \sqrt{2} E_{rms}^*.\end{aligned}$$

Given a maximum RMS value of the grid current I_{grms}^{max}, then by selecting the controller parameter $w_{min} = \frac{E_{rms}^*}{I_{grms}^{max}}$ and taking into account that the system (5.13)-(5.14) is ISS, it holds true that if at the time that the controller is enabled, the grid current is less than the maximum I_{grms}^{max}, i.e. $I_{grms}(0) < I_{grms}^{max}$, then

$$I_{grms}(t) \leq \frac{E_{rms}^*}{w_{min}} = I_{grms}^{max}, \forall t > 0.$$

Hence, it is mathematically proven that the grid current of the inverter will never violate a given maximum value I_{grms}^{max}. It is highlighted that the maximum value of the grid current is guaranteed by suitably selecting the minimum value of the virtual resistances w_d and w_q in the proposed controller dynamics.

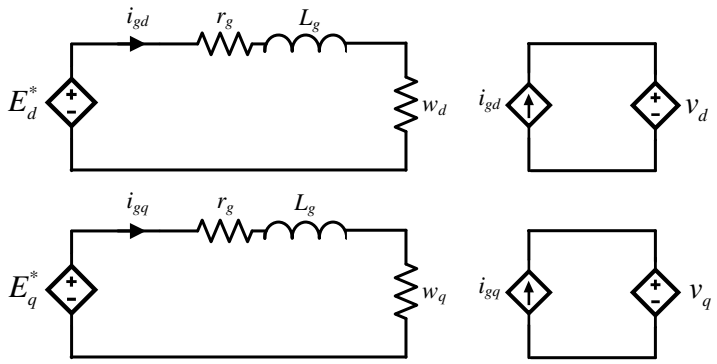

Figure 5.3: Equivalent circuit of the closed-loop system

5.2.3.2 Asymptotic Stability

As it can be seen from (5.13)-(5.14), the dynamics of the grid current are decoupled from the inverter current and capacitor voltage dynamics and are independent from each other due to the lack of cross-coupling terms. The equivalent circuit of the three-phase grid-connected inverter can be simplified as shown in Fig. 5.3 and its dynamics are given by (5.9)-(5.12) and (5.13)-(5.14). Given that in the used SRF the real and reactive power can be calculated from $P = \frac{3}{2}(v_d i_{gd} + v_q i_{gq})$ and $Q = \frac{3}{2}(v_d i_{gq} - v_q i_{gd})$, the state vector of the closed-loop system is $x = [w_d\, w_{dq}\, w_q\, w_{qq}\, i_{gd}\, i_{gq}]^T$. Since $w_{de}, w_{qe} \in (w_{min}, w_{max})$ then $w_{dqe}, w_{qqe} \in (0, 1]$ and for any equilibrium point $x_e = [w_{de}\, w_{dqe}\, w_{qe}\, w_{qqe}\, i_{gde}\, i_{gqe}]^T$, the investigation of closed-loop system stability using the Jacobian matrix results into two negative eigenvalues $-2k_w w_{dqe}^2$ and $-2k_w w_{qqe}^2$ and the remaining eigenvalues obtained from matrix

$$A = \begin{bmatrix} 0 & 0 & c_{wd} w_{dqe}^2 n \frac{3}{2} v_d & c_{wd} w_{dqe}^2 n \frac{3}{2} v_q \\ 0 & 0 & -c_{wq} m w_{qqe}^2 \frac{3}{2} v_q & c_{wq} w_{qqe}^2 m v_d \frac{3}{2} \\ -\frac{E_d^*}{L_g(r_g + w_{de})} & 0 & -\frac{w_{de} + r_g}{L_g} & 0 \\ 0 & -\frac{E_q^*}{L_g(r_g + w_{qe})} & 0 & -\frac{w_{qe} + r_g}{L_g} \end{bmatrix}.$$

To ensure the asymptotic stability, the eigenvalues of A need to have negative real parts, according to Theorem 1 in sec. 3.1. The characteristic polynomial of matrix A is $\lambda^4 + \alpha_3\lambda^3 + \alpha_2\lambda^2 + \alpha_1\lambda + \alpha_0 = 0$, where

$$\alpha_3 = \frac{w_{de} + w_{qe} + 2r_g}{L_g}$$

$$\alpha_2 = \beta \frac{E_{rms}^*}{L_g(r_g + w_{de})} + \alpha \frac{E_{rms}^*}{L_g(r_g + w_{qe})} + \frac{(w_{de} + r_g)(w_{qe} + r_g)}{L_g^2}$$

$$\alpha_1 = \alpha \frac{E_{rms}^*(w_{de} + r_g)}{L_g^2(w_{qe} + r_g)} + \beta \frac{E_{rms}^*(w_{qe} + r_g)}{L_g^2(w_{de} + r_g)}$$

$$\alpha_0 = \frac{2\alpha\beta E_{rms}^{*2}}{L_g^2(w_{de}+r_g)(w_{qe}+r_g)},$$

with $\alpha = c_{wq}w_{qqe}^2 m\frac{3}{2}V_g$ and $\beta = c_{wd}w_{dqe}^2 n\frac{3}{2}V_g$, where $V_g = v_d = v_q$ and $E_{rms}^* = E_d^* = E_q^*$. Note that $v_d = v_q$ and $E_d^* = E_q^*$ can be achieved by selecting $\theta_a = 45^o$ in the generic $T_{\alpha\beta}$ transformation. Then, to ensure the asymptotic stability of x_e using the Ruth-Hurwitz criterion, the following conditions need to be satisfied

$$\frac{\beta E_{rms}^* \left(w_{de}+w_{qe}+2r_g\right)}{\left(w_{de}+r_g\right)\left(w_{qe}+r_g\right)} < \frac{\left(w_{de}+r_g\right)^2}{L_g} \tag{5.15}$$

$$\frac{\alpha E_{rms}^* \left(w_{de}+w_{qe}+2r_g\right)}{\left(w_{de}+r_g\right)\left(w_{qe}+r_g\right)} < \frac{\left(w_{qe}+r_g\right)^2}{L_g}. \tag{5.16}$$

Taking into account that w_{de}, $w_{qe} > w_{min} = \frac{E_{rms}^*}{I_{grms}^{max}}$, then the conditions to guarantee asymptotic stability result in

$$c_{wd} < \frac{\left(\frac{E_{rms}^*}{I_{grms}^{max}} + r_g\right)^4}{3V_g E_{rms}^* L_g n \left(w_{max}+r_g\right)} \tag{5.17}$$

$$c_{wq} < \frac{\left(\frac{E_{rms}^*}{I_{grms}^{max}} + r_g\right)^4}{3V_g E_{rms}^* L_g m \left(w_{max}+r_g\right)}. \tag{5.18}$$

According to (5.17)-(5.18), the controller parameters c_{wd}, c_{wq} can be selected accordingly to guarantee asymptotic stability of any equilibrium point x_e in addition to the desired current-limiting property.

Table 5.1: System and controller parameters for real-time simulations

Parameters	Values	Parameters	Values
L, L_g	2.2 mH	K_e	1
r, r_g	1 Ω	ω_g	314.15 rad/s
C	1 μF	I_{grms}^{max}	3 A
E_{rms}^*	110 V	w_m	294.4 Ω
c_{wd}	183	Δw_m	257.8 Ω
c_{wq}	3217	k_w	1000
n	0.0056	m	0.0032

5.2.4 Controller verification through real-time simulation results

In order to verify the proposed control approach, a three-phase grid-connected inverter equipped with the controller proposed in sec. 5.2.2 will be tested using a OP4500 OPAL-RT real-time digital simulator. The parameters of the controller and the power system are given in Tab. 5.1. The controller is enabled and the reference values P_{set} and Q_{set} have the values of 400 W and 0 Var, respectively. Note that initially, the proposed controller operates in the PQ-set mode and regulates P and Q to their desired values, as shown in Figures 5.4a and 5.4b. In Fig. 5.4d, one can observe that the voltage remains at its nominal value during this operation since a stiff grid is assumed. At 5s, Q_{set} is changed to 50 Var and the reactive power injection is accordingly modified, as depicted in Fig. 5.4b, while at 10s, P_{set} is set as 600 W. At 15s, the droop control operation is enabled and both the real and reactive power drop due to the slightly higher value of the grid voltage compared to the nominal (110.3 V) and the slightly lower than the nominal grid frequency (49.98 Hz). At 20s, a grid voltage drop of 0.2 p.u. occurs (as shown in Fig. 5.4d) to test the operation under faults and the desired current-limiting property of the controller. As shown in Fig. 5.4c, the grid current reaches its maximum RMS value of 3 A, as it has been analytically proven in sec. 5.2.3.1, thus protecting the inverter under grid faults. When the fault is self-cleared at 25s, P and Q return to their original values according to droop control, always without violating the maximum grid current.

Regarding the controller states that were introduced through the control design, one can observe in Figures 5.4e and 5.4f the time response of w_d and w_q, which change in order to regulate the real and reactive power accordingly. As observed in both figures, when the current limit is triggered at 20s, w_d and w_q reach their minimum value $\left(w_{min} = \frac{E^*_{rms}}{I^{max}_{grms}} = \frac{110}{3} = 36.66\,\Omega\right)$, in order to maintain the grid current limited below its given maximum value.

5.3 Voltage support under grid faults with inherent current limitation for three-phase droop-controlled inverters

In the previous section, a current-limiting droop controller was proposed for three-phase grid-connected inverters, based on the CLD concept of [45] and the BIC concept of [56]. However, there is a challenge in developing control schemes that can

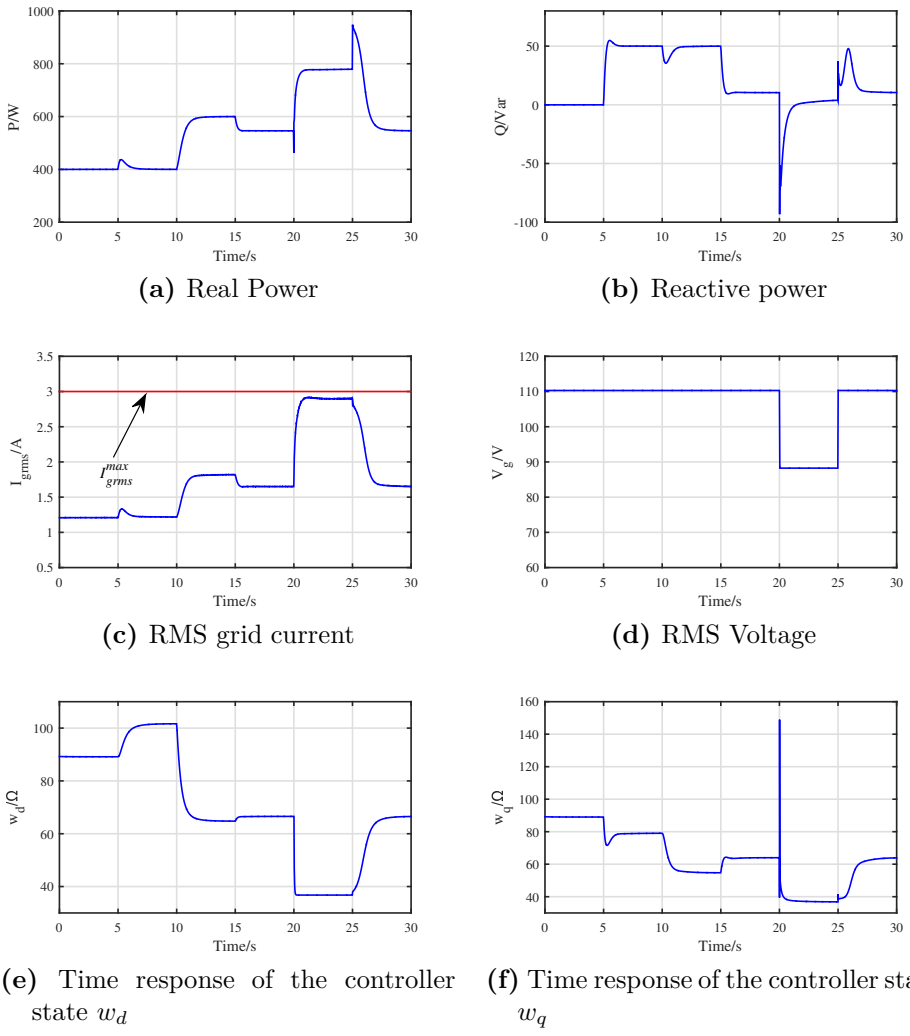

(a) Real Power **(b)** Reactive power

(c) RMS grid current **(d)** RMS Voltage

(e) Time response of the controller state w_d **(f)** Time response of the controller state w_q

Figure 5.4: Response of the three-phase grid-connected inverter equipped with the proposed controller

safely deal with unbalanced grid faults, which represent a more realistic case rather than balanced three-phase grid faults. Hence, in this section, a rigorous modeling in the SRF (dq) frame is performed, while considering both positive and negative sequence components. Moreover, a more accurate power system model is taken into consideration with a line (feeder) between the PCC and the grid. Then, an advanced control scheme is proposed that adopts the droop control during normal grid conditions and complies with the "voltage support concept" during faulty (balanced and unbalanced) grid conditions. In particular, two power controllers are proposed for the positive and the negative sequence systems, to provide voltage support by increasing the positive sequence voltage and eliminating the negative sequence voltage (as required by the "voltage support concept" [35]), while rigorously guaranteeing a limited current injection, during faults. To ensure the safe inverter operation

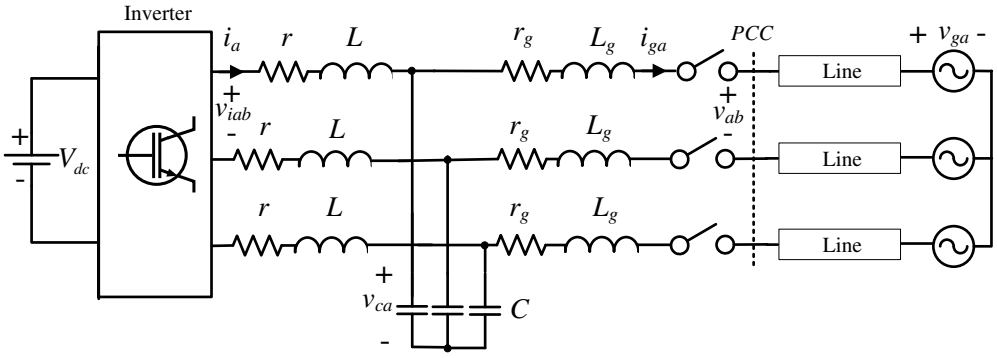

Figure 5.5: Three-phase inverter connected to the grid through an LCL filter and a line

during unbalanced grid faults, a novel method is proposed to divide the maximum available current into the positive and the negative sequence current components. Finally, the proposed control scheme is proven to guarantee asymptotic stability of the grid-connected inverter closed-loop system.

5.3.1 Power system under consideration

The system under consideration consists of a three-phase inverter connected to the grid through an LCL filter and a line, as depicted in Fig. 5.5. The capacitors of the filter are denoted as C, while the inductors are denoted as L and L_g with their parasitic resistances being r and r_g, respectively. The line-to-line inverter voltage between phases a and b is given as v_{iab}, while v_{ia} represents the phase voltage of the inverter. The capacitor voltage is denoted as v_{ca} while the PCC voltage is v_a with $v_a = \sqrt{2}V\cos\omega_g t$, where V is the RMS PCC voltage and ω_g is the angular PCC frequency. The grid voltage is denoted as v_{ga} and is considered as unknown for the controller design. The inverter and grid side currents are i_a and i_{ga}, respectively. When considering a balanced system, the above voltage and current quantities match with the positive sequence components. However, in the presence of unbalanced grid conditions, both positive and negative sequence components appear, while zero sequence components can be neglected when considering a three-phase three-wire system. In order to obtain the dynamic model of the system in both sequences, the widely used synchronous reference framework (SRF) theory is considered together with the delay signal cancellation (DSC) sequence extraction method [29, 127], as explained in the analysis that follows.

5.3.2 System modeling in the SRF under unbalanced grid conditions

Similarly to sec. 5.2, the clockwise SRF transformation is considered. In order to align phase a to the α axis, θ_a can be selected as 0^o in the generic $\alpha\beta$ transformation presented in [49]

$$T_{\alpha\beta} = \frac{2}{3}\begin{bmatrix} \cos\theta_a & \cos(\theta_a - 120) & \cos(\theta_a + 120) \\ \sin\theta_a & \sin(\theta_a - 120) & \sin(\theta_a + 120) \\ 0.5 & 0.5 & 0.5 \end{bmatrix}.$$

Following to the $T_{\alpha\beta}$ transformation, the sequential transformation for the clockwise SRF takes the form:

$$T_{+-} = \frac{1}{2}\begin{bmatrix} 1 & 0 & 0 & 0 & 1 & 0 \\ 0 & 1 & 0 & -1 & 0 & 0 \\ 0 & 0 & 1 & 0 & 0 & 0 \\ 1 & 0 & 0 & 0 & -1 & 0 \\ 0 & 1 & 0 & 1 & 0 & 0 \\ 0 & 0 & 0 & 0 & 0 & 1 \end{bmatrix}.$$

The matrix T_{+-} occurs from the DSC method which is employed here because it is faster compared to the methods using low-pass filters [33]. Note that this matrix is different when the anti-clockwise SRF is employed, while for details on obtaining this matrix and a comparison with the low pass filtering method, the reader is referred to [128]. T_{+-} is then followed by the rotating transformation

$$T_{dq}^{+-} = \begin{bmatrix} \cos\theta_g^{+-} & -\sin\theta_g^{+-} & 0 \\ \sin\theta_g^{+-} & \cos\theta_g^{+-} & 0 \\ 0 & 0 & 1 \end{bmatrix},$$

where $\theta_g^+ = \omega_g t$ for the positive sequence and $\theta_g^- = -\omega_g t$ for the negative sequence. Hence, considering $T(t) = \tilde{T}_{dq} T_{+-} \tilde{T}_{\alpha\beta}$ with $\tilde{T}_{\alpha\beta} = \begin{bmatrix} T_{\alpha\beta} & 0_{3x3} \\ 0_{3x3} & T_{\alpha\beta} \end{bmatrix}$ and $\tilde{T}_{dq} = \begin{bmatrix} T_{dq}^+ & 0_{3x3} \\ 0_{3x3} & T_{dq}^- \end{bmatrix}$, then the complete transformation can be described for a cosinusoidal three-phase voltage variable v_{abc} from the equation

$$\begin{bmatrix} v_d^+ \\ v_q^+ \\ v_0^+ \\ v_d^- \\ v_q^- \\ v_0^- \end{bmatrix} = T(t)\begin{bmatrix} v_a(t) \\ v_b(t) \\ v_c(t) \\ v_a(t-T) \\ v_b(t-T) \\ v_c(t-T) \end{bmatrix} = \begin{bmatrix} \frac{\sqrt{2}}{3}(V_a + V_b + V_c) \\ 0 \\ \frac{1}{6}(v_a(t) + v_b(t) + v_c(t)) \\ \frac{\sqrt{2}}{3}(V_a - 0.5V_b - 0.5V_c) \\ \frac{1}{\sqrt{6}}(V_b - V_c) \\ \frac{1}{6}(v_a(t-T) + v_b(t-T) + v_c(t-T)) \end{bmatrix}, \tag{5.19}$$

where $T = \frac{1}{4f}$ and $f = \frac{\omega_g}{2\pi}$. By applying the above transformation to the three-phase current and voltage quantities of the system, the SRF-based dynamic equations of the three-phase grid-tied inverter are obtained as

$$L\frac{di_d^{+-}}{dt} = v_{id}^{+-} - v_{cd}^{+-} - ri_d^{+-} \mp \omega_g L i_q^{+-} \tag{5.20}$$

$$L\frac{di_q^{+-}}{dt} = v_{iq}^{+-} - v_{cq}^{+-} - ri_q^{+-} \pm \omega_g L i_d^{+-} \tag{5.21}$$

$$L_g\frac{di_{gd}^{+-}}{dt} = v_{cd}^{+-} - v_d^{+-} - r_g i_{gd}^{+-} \mp \omega_g L_g i_{gq}^{+-} \tag{5.22}$$

$$L_g\frac{di_{gq}^{+-}}{dt} = v_{cq}^{+-} - v_q^{+-} - r_g i_{gq}^{+-} \pm \omega_g L_g i_{gd}^{+-} \tag{5.23}$$

$$C\frac{dv_{cd}^{+-}}{dt} = i_d^{+-} - i_{gd}^{+-} \mp \omega_g C v_{cq}^{+-} \tag{5.24}$$

$$C\frac{dv_{cq}^{+-}}{dt} = i_q^{+-} - i_{gq}^{+-} \pm \omega_g C v_{cd}^{+-}, \tag{5.25}$$

where v_{id}^{+-} and v_{iq}^{+-} are the positive and negative sequence dq-axis components of the inverter voltage and represent the control inputs of the system. For the $\pm$ and $\mp$ signs that appear in the coupling terms in (5.20)-(5.25), the top operator corresponds to the positive sequence and the bottom one to the negative sequence. The instantaneous real and reactive power injected to the grid can be calculated from

$$p = P^+ + P^- + \widetilde{p},\ q = Q^+ + Q^- + \widetilde{q},$$

where

$$P^+ = \frac{3}{2}v_d^+ i_{gd}^+,\ P^- = \frac{3}{2}(v_d^- i_{gd}^- + v_q^- i_{gq}^-) \tag{5.26}$$

$$Q^+ = \frac{3}{2}v_d^+ i_{gq}^+,\ Q^- = \frac{3}{2}(v_d^- i_{gq}^- - v_q^- i_{gd}^-) \tag{5.27}$$

since v_q^+ is always zero from (5.19), while $\widetilde{p}, \widetilde{q}$ are oscillation terms with zero average value [30, 33, 109]. The VUF can be defined now at the PCC as

$$VUF = \frac{V^-}{V^+} = \frac{\sqrt{v_d^{-2} + v_q^{-2}}}{\sqrt{v_d^{+2} + v_q^{+2}}}$$

while VUF_{grid} is equivalently derived for the grid side [129, 130].

5.3.3 The proposed control scheme

The proposed controller consists of two inner-loop controllers, i.e. current and voltage control, designed in the $\alpha\beta$ frame and two novel outer-loop controllers in the SRF (in the positive and negative sequence), which include the droop control concept and inherently limit the grid current in both sequences.

5.3.3.1 Inner-loop controllers

The current controller of the inner control loop takes the form

$$v_{i\alpha} = v_{c\alpha} + \left(k_{PCC} + k_{RCC}\frac{s}{s^2+\omega_g^2}\right)(i_\alpha^{ref} - i_\alpha) \tag{5.28}$$

$$v_{i\beta} = v_{c\beta} + \left(k_{PCC} + k_{RCC}\frac{s}{s^2+\omega_g^2}\right)(i_\beta^{ref} - i_\beta) \tag{5.29}$$

where PR controllers are applied to regulate i_α to i_α^{ref} and i_β to i_β^{ref}. Similarly, the voltage controller, from which i_α^{ref} and i_β^{ref} are obtained, is described through the equations

$$i_\alpha^{ref} = i_{g\alpha} + \left(k_{PVC} + k_{RVC}\frac{s}{s^2+\omega_g^2}\right)(v_{c\alpha}^{ref} - v_{c\alpha}) \tag{5.30}$$

$$i_\beta^{ref} = i_{g\beta} + \left(k_{PVC} + k_{RVC}\frac{s}{s^2+\omega_g^2}\right)(v_{c\beta}^{ref} - v_{c\beta}) \tag{5.31}$$

where the reference values $v_{c\alpha}^{ref}$ and $v_{c\beta}^{ref}$ are defined from the values $v_{cd}^{ref+}, v_{cd}^{ref-}$ and $v_{cq}^{ref+}, v_{cq}^{ref-}$ (generated by the positive and negative sequence outer-loop controllers) transformed to $\alpha\beta$. Note that as in typical multi-loop controller applications, the PR controller gains can be suitably selected such that the current controller settles much faster than the voltage controller which settles much faster than the outer-loop controllers. Thus, for the outer-loop controllers design, which operate in a slower time scale, it is reasonable to assume that $v_{c\alpha}$ and $v_{c\beta}$ quickly track $v_{c\alpha}^{ref}$ and $v_{c\beta}^{ref}$. This is a common assumption for the inner-loop controllers used in DERs applications and further analysis can be found in [29].

5.3.3.2 Positive sequence current-limiting droop control

The positive sequence outer-loop controller consists of a droop-based power controller to support the grid. Since apart from the droop operation, a grid current limitation should be embedded through the power controller, inspired by [45], a virtual resistance should be introduced through the control design. Furthermore, to realize current limitation, the controller states should be bounded in a range set by the operator. In order to avoid the possible instability issues that may occur

when using saturation units, for the boundedness of the controller states, the BIC structure from [56] is adopted here. Following the introduction of the inner-loop controller in sec. 5.3.3.1, the power controller will be directly applied to the capacitor voltage of the LCL filter through controlling the reference capacitor voltage values v_{cd}^{ref+} and v_{cq}^{ref+}. The proposed controller is described by the following equations

$$v_{cd}^{ref+} = v_d^+ + E_d^+ - r_v^+ i_{gd}^+ + \omega_g L_g i_{gq}^+ \tag{5.32}$$
$$v_{cq}^{ref+} = v_q^+ + E_q^+ - r_v^+ i_{gq}^+ - \omega_g L_g i_{gd}^+ \tag{5.33}$$

where r_v^+ is a constant virtual resistance and E_d^+, E_q^+ are virtual voltages applied to each axis which change according to the expressions

$$\dot{E}_d^+ = c_{pd} f(\mathcal{P}^+) \left(E_{dq}^+\right)^2 - k_{we} \left(\frac{\left(E_d^+\right)^2}{\left(E_{max}^+\right)^2} + \left(E_{dq}^+\right)^2 - 1 \right) E_d^+ \tag{5.34}$$
$$\dot{E}_{dq}^+ = -\frac{c_{pd} E_d^+ E_{dq}^+}{\left(E_{max}^+\right)^2} f(\mathcal{P}^+) - k_{we} \left(\frac{\left(E_d^+\right)^2}{\left(E_{max}^+\right)^2} + \left(E_{dq}^+\right)^2 - 1 \right) E_{dq}^+$$
$$\dot{E}_q^+ = c_{pq} g(\mathcal{Q}^+) \left(E_{qq}^+\right)^2 - k_{we} \left(\frac{\left(E_q^+\right)^2}{\left(E_{max}^+\right)^2} + \left(E_{qq}^+\right)^2 - 1 \right) E_q^+ \tag{5.35}$$
$$\dot{E}_{qq}^+ = -\frac{c_{pq} E_q^+ E_{qq}^+}{\left(E_{max}^+\right)^2} g(\mathcal{Q}^+) - k_{we} \left(\frac{\left(E_q^+\right)^2}{\left(E_{max}^+\right)^2} + \left(E_{qq}^+\right)^2 - 1 \right) E_{qq}^+$$

where c_{pd}, c_{pq}, k_{we}, E_{max}^+ are positive constants and

$$f(\mathcal{P}^+) = n(P_{set}^+ - \mathcal{P}^+) + E_{rms}^+ - V^+ \tag{5.36}$$
$$g(\mathcal{Q}^+) = m(Q_{set}^+ - \mathcal{Q}^+) - \omega^* + \omega_g \tag{5.37}$$

where E_{rms}^+ is the RMS nominal voltage in the positive sequence, n, m are the droop coefficients, while the powers are being measured from $\mathcal{P}^+ = \frac{3 v_d^+ E_d^+}{2 r_v^+}$ and $\mathcal{Q}^+ = \frac{3 v_d^+ E_q^+}{2 r_v^+}$ by using the steady-state current values (this will be further explained in sec. 5.3.3.4). Hence, at the steady-state $\mathcal{P}^+ = P^+$ and $\mathcal{Q}^+ = Q^+$, thus achieving the desired droop control operation at the steady-state, while the expressions of $\mathcal{P}^+$ and $\mathcal{Q}^+$ are used to facilitate the stability analysis, as explained in the sequel. The positive sequence reference real and reactive power are denoted as P_{set}^+ and Q_{set}^+ respectively. It should be highlighted that the $P \sim V$ and $Q \sim -\omega$ droop expressions of the universal droop control scheme are adopted here [79], to provide robustness to different output impedance. Through the functions (5.36)-(5.37), the PQ-set and PQ-droop control modes are inherited in the control system. In these two control modes, the inverter either regulates the real and reactive power to their reference values P_{set}^+, Q_{set}^+, when the terms $E_{rms}^+ - V^+$ and $-\omega^* + \omega_g$ are removed from (5.36) and (5.37),

respectively, or supports the grid voltage and frequency regulation through droop control. For the dynamics of the virtual voltages E_d^+ and E_q^+ in (5.32)-(5.33), the bounded integral controller (BIC), proposed in [56], is adopted in order to guarantee the boundedness of E_d^+ and E_q^+ without using any saturated integrators that could drive the system to instability. It is noteworthy that in this control scheme, the terms $-k_{we}\left(\frac{\left(E_d^+\right)^2}{\left(E_{max}^+\right)^2}+\left(E_{dq}^+\right)^2-1\right)E_d^+$ and $-k_{we}\left(\frac{\left(E_q^+\right)^2}{\left(E_{max}^+\right)^2}+\left(E_{qq}^+\right)^2-1\right)E_q^+$ have been added in (5.34)-(5.35) to guarantee attractiveness of the controller states to a desired ellipse on the phase plane. To further explain this, consider the lower bounded function

$$W=\frac{1}{4}\left(\frac{\left(E_d^+\right)^2}{\left(E_{max}^+\right)^2}+\left(E_{dq}^+\right)^2-1\right)^2$$

for the system (5.34). The time derivative of W takes the form

$$\dot{W}=\frac{1}{2}\left(\frac{\left(E_d^+\right)^2}{\left(E_{max}^+\right)^2}+\left(E_{dq}^+\right)^2-1\right)\left(\frac{2E_d^+\dot{E}_d^+}{\left(E_{max}^+\right)^2}+2E_{dq}^+\dot{E}_{dq}^+\right)$$

which by substituting $\dot{E}_d^+$ and $\dot{E}_{dq}^+$ from (5.34), becomes

$$\dot{W}=-k_{we}\left(\frac{\left(E_d^+\right)^2}{\left(E_{max}^+\right)^2}+\left(E_{dq}^+\right)^2-1\right)^2\left(\frac{\left(E_d^+\right)^2}{\left(E_{max}^+\right)^2}+\left(E_{dq}^+\right)^2\right)\leqslant 0. \tag{5.38}$$

Furthermore, one can easily show that $\ddot{W}$ is bounded. Hence, according to the "Lyapunov-Like Lemma" (Lemma 4.3 in [120]), $\dot{W}\to 0$ as $t\to\infty$. It is clear from (5.38) that $\dot{W}=0$ holds at the set $E=\left\{E_d^+,E_{dq}^+\in R:\frac{\left(E_d^+\right)^2}{\left(E_{max}^+\right)^2}+\left(E_{dq}^+\right)^2=1\right\}$ and at the origin. However, regarding the origin, where $E_d^+=0$ and $E_{dq}^+=0$, it can be easily proven that it is an unstable equilibrium point, from Theorem 4.4 in [120], by considering the continuously differentiable function $\bar{W}=\frac{\left(E_d^+\right)^2}{\left(E_{max}^+\right)^2}+\left(E_{dq}^+\right)^2$. Thus, starting from any initial conditions E_{d0}^+ and E_{dq0}^+, except from the origin, the states E_d^+ and E_{dq}^+ will be quickly attracted on E and remain on the curve thereafter ensuring that $E_d^+\in[-E_{max}^+,E_{max}^+],\forall t\geq 0$. Note that the positive parameter E_{max}^+ represents the horizontal radius of the ellipse E and when it varies, it becomes clear from (5.38), that E_d^+ and E_{dq}^+ will quickly converge to a new ellipse. The larger the k_{we}, the faster the convergence. This enables an adaptation of the upper and lower bounds of E_d^+. A similar analysis holds for E_q^+ and E_{qq}^+ guaranteeing that $E_q^+\in[-E_{max}^+,E_{max}^+],\forall t\geq 0$.

5.3.3.3 Negative sequence current-limiting control

The proposed current-limiting controller in the negative sequence is designed in a similar form and aims at regulating the negative sequence grid current. Hence it

can be obtained as follows

$$v_{cd}^{ref-} = v_d^- + E_d^- - r_v^- i_{gd}^- - \omega_g L_g i_{gq}^- \tag{5.39}$$
$$v_{cq}^{ref-} = v_q^- + E_q^- - r_v^- i_{gq}^- + \omega_g L_g i_{gd}^- \tag{5.40}$$

where similarly to the positive sequence controller, r_v^- is a constant virtual resistance and E_d^-, E_q^- are virtual voltages applied to each axis which change according to the expressions

$$\dot{E}_d^- = c_{nd}\left(i_{gd}^{ref-} - \frac{E_d^-}{r_v^-}\right)\left(E_{dq}^-\right)^2 - k_{we}\left(\frac{\left(E_d^-\right)^2}{\left(E_{max}^-\right)^2} + \left(E_{dq}^-\right)^2 - 1\right)E_d^- \tag{5.41}$$
$$\dot{E}_{dq}^- = -\frac{c_{nd}E_d^- E_{dq}^-}{\left(E_{max}^-\right)^2}\left(i_{gd}^{ref-} - \frac{E_d^-}{r_v^-}\right) - k_{we}\left(\frac{\left(E_d^-\right)^2}{\left(E_{max}^-\right)^2} + \left(E_{dq}^-\right)^2 - 1\right)E_{dq}^-$$
$$\dot{E}_q^- = c_{nq}\left(i_{gq}^{ref-} - \frac{E_q^-}{r_v^-}\right)\left(E_{qq}^-\right)^2 - k_{we}\left(\frac{\left(E_q^-\right)^2}{\left(E_{max}^-\right)^2} + \left(E_{qq}^-\right)^2 - 1\right)E_q^- \tag{5.42}$$
$$\dot{E}_{qq}^- = -\frac{c_{nq}E_q^- E_{qq}^-}{\left(E_{max}^-\right)^2}\left(i_{gq}^{ref-} - \frac{E_q^-}{r_v^-}\right) - k_{we}\left(\frac{\left(E_q^-\right)^2}{\left(E_{max}^-\right)^2} + \left(E_{qq}^-\right)^2 - 1\right)E_{qq}^-$$

where $i_{gd}^{ref-} = \frac{2\left(P_{set}^- v_d^- - Q_{set}^- v_q^-\right)}{3\left(v_d^{-2} + v_q^{-2}\right)}$ and $i_{gq}^{ref-} = \frac{2\left(P_{set}^- v_q^- + Q_{set}^- v_d^-\right)}{3\left(v_d^{-2} + v_q^{-2}\right)}$ are the current reference values, which can be realized by equating the P^- and Q^- formulas from (5.26) and (5.27) with their reference values P_{set}^- and Q_{set}^-, while c_{nd}, c_{nq}, E_{max}^- are positive constants. As one can see, through the proposed controller, the expressions $\frac{E_d^-}{r_v^-}$ and $\frac{E_q^-}{r_v^-}$, which represent a good approximation of the steady-state negative sequence current values (see sec. 5.3.3.4) can be regulated to the reference values i_{gd}^{ref-} and i_{gq}^{ref-}. Through this control structure, P^- and Q^- can track their reference values which can be computed to optimally eliminate the negative sequence voltage. Following a similar analysis to the positive sequence controller, it can be proven that $E_d^-, E_q^- \in [-E_{max}^-, E_{max}^-], \forall t \geq 0$, which facilitates the desired current limitation. The methodology for generating P_{set}^- and Q_{set}^- and the current-limiting property are explained in the sequel.

5.3.3.4 Current-limiting property

By substituting the proposed controller (5.32)-(5.33) and (5.39)-(5.40) into the system dynamics (5.22)-(5.23), the closed-loop system takes the form

$$L_g \frac{di_{gd}^{+-}}{dt} = E_d^{+-} - \left(r_v^{+-} + r_g\right) i_{gd}^{+-} \tag{5.43}$$

$$L_g \frac{di_{gq}^{+-}}{dt} = E_q^{+-} - \left(r_v^{+-} + r_g\right) i_{gq}^{+-}. \tag{5.44}$$

The equations (5.43) and (5.44) are the derived dynamics of the grid current in both sequences. From (5.43) and (5.44) the steady-state value of the grid currents can be approximated from $i_{gde}^{+-} \backsimeq \frac{E_d^{+-}}{r_v^{+-}}$ and $i_{gqe}^{+-} \backsimeq \frac{E_q^{+-}}{r_v^{+-}}$ considering that $r_v^{+-} > r_g$, which can be achieved by appropriately selecting the virtual resistances r_v^{+-}, which represent controller parameters. This is why the previous expressions are used in (5.36), (5.37), (5.41), (5.42). Taking into account that $E_d^{+-}, E_q^{+-} \in [-E_{max}^{+-}, E_{max}^{+-}], \forall t \geq 0$, let us consider the continuous differentiable function candidate

$$V = \frac{1}{2} L_g i_{gd}^{+-2}$$

for system (5.43).

The time derivative of V becomes

$$\dot{V} = -\left(r_g + r_v^{+-}\right)\left(i_{gd}^{+-}\right)^2 + i_{gd}^{+-} E_d^{+-} \leq -\left(r_g + r_v^{+-}\right)\left(i_{gd}^{+-}\right)^2 + \left|i_{gd}^{+-}\right|\left|E_d^{+-}\right|.$$

Thus,

$$\dot{V} \leq -r_g \left(i_{gd}^{+-}\right)^2, \forall \left|i_{gd}^{+-}\right| \geq \frac{\left|E_d^{+-}\right|}{r_v^{+-}}$$

which according to Theorem 3 in sec. 3.3, proves that system (5.43) is input-to-state stable (ISS) by considering E_d^{+-} as the input. Since it is proven that $\left|E_d^{+-}\right| \leq E_{max}^{+-}, \forall t \geq 0$, then i_{gd}^{+-} will be bounded for all $t \geq 0$. More precisely, it will hold that

$$\left|i_{gd}^{+-}\right| \leq \frac{E_{max}^{+-}}{r_v^{+-}}, \forall t \geq 0,$$

with the condition that initially $\left|i_{gd}^{+-}(0)\right| \leq \frac{E_{max}^{+-}}{r_v^{+-}}$. This holds true because the set $\Omega = \left\{i_{gd}^{+-} \in R, \left|i_{gd}^{+-}\right| \leq \frac{E_{max}^{+-}}{r_v^{+-}}\right\}$ is invariant. Hence, if E_{max}^{+} and E_{max}^{-} are selected as $E_{max}^{+} = \sqrt{2} r_v^{+} I_{grms}^{max+}$ and $E_{max}^{-} = r_v^{-} I_{grms}^{max-}$, then $\left|i_{gd}^{+}\right| \leq \sqrt{2} I_{grms}^{max+}$ and $\left|i_{gd}^{-}\right| \leq I_{grms}^{max-}$. Since the same analysis and same result holds for the q axis current as well, it is

concluded that

$$\begin{aligned} I^{+}_{grms} &= \frac{\sqrt{\left(i^{+}_{gd}\right)^2+\left(i^{+}_{gq}\right)^2}}{\sqrt{2}} \leq \sqrt{2} I^{max+}_{grms} \\ I^{-}_{grms} &= \frac{\sqrt{\left(i^{-}_{gd}\right)^2+\left(i^{-}_{gq}\right)^2}}{\sqrt{2}} \leq I^{max-}_{grms}. \end{aligned}$$

The reason $\sqrt{2}$ is used in E^{+}_{max} and the way I^{max+}_{grms} and I^{max-}_{grms} are selected online, are further explained in sec. 5.3.4.2.

5.3.4 Operation under the voltage support scheme

5.3.4.1 Fault-ride-through operation

Fault-ride-through guidelines have been recently proposed in order to standardize the way DERs should provide support under grid faults. In particular, during grid voltage drops, DERs should provide voltage support through reactive power injection instead of getting disconnected due to tripping of the inverter. In a wider manner, the most common voltage support technique in the literature is the "voltage support concept" where maximum available power is injected to the grid in order to increase the voltage level at the PCC and reduce voltage unbalance [35]. To understand this, consider the voltage difference between the PCC and the grid $\Delta V^{+} = V^{+} - V^{+}_{g}$ and assuming a resistive-inductive line with resistance r_l and inductance L_l, let us use the approximation of this voltage difference as it is commonly presented in the literature [131, 132]

$$\Delta V^{+} = \frac{P^{+} r_l + Q^{+} x_{L_l}}{3V^{+}}. \tag{5.45}$$

Interested readers can obtain this approximation by using the equations that relate the magnitudes of the PCC and grid voltages according to the current real and reactive components, as shown in [32, 133, 134].

Since power lines are most of the times considered as predominantly inductive, it can be understood from (5.45) that reactive power affects more drastically the PCC voltage and thus, by injecting reactive power we can increase the PCC voltage level compared to the faulty grid voltage. In case only resistive or only inductive impedance is considered between the PCC and the grid, the relations between the amplitudes are simplified as presented in [35], thus requiring the injection of only real or reactive power respectively to support PCC by increasing ΔV^{+}. The most commonly used FRT guidelines are those from the German grid code [135] which take the form:

$$I^{+}_{grmsQ} = \begin{cases} 0, & V^{+} \geqslant 0.9E^{+}_{rms} \\ \left(1 - \frac{V^{+}}{E^{+}_{rms}}\right) k I^{max+}_{grms}, & 0.5E^{+}_{rms} < V^{+} < 0.9E^{+}_{rms} \\ I^{max+}_{grms}, & V^{+} \leqslant 0.5E^{+}_{rms} \end{cases} \tag{5.46}$$

where I^{+}_{grmsQ} is the reactive component of the positive sequence grid current and k is the FRT gain ($k \geq 2$) with $\left(1 - \frac{V^{+}}{E^{+}_{rms}}\right) k \leq 1$. According to (5.46), it is concluded that $P^{+}_{set} = \sqrt{\left(S^{+}_{max}\right)^2 - \left(Q^{+}_{set}\right)^2}$ and $Q^{+}_{set} = \left(1 - \frac{V^{+}}{E^{+}_{rms}}\right) k S^{+}_{max}$, where S^{+}_{max} represents the amount of apparent power assigned to the positive sequence controller during faults, in the case where $0.5E^{+}_{rms} < V^{+} < 0.9E^{+}_{rms}$.

Regarding the negative sequence voltage (which is a crucial part of the "voltage support concept" as well), according to the literature, it can be eliminated by increasing the negative sequence reactive power and decreasing the negative sequence real power. This can be understood either from [32], where equations that involve the magnitude of the PCC voltage are shown to explain the negative sequence voltage elimination concept or from the phasor analysis in [33]. For the calculation of the negative sequence reference powers during unbalanced grid faults, in this control scheme, a PI controller is applied to generate Q^{-}_{set}, i.e.

$$Q^{-}_{set} = \left(k_{PVU} + \frac{k_{IVU}}{s}\right)\left(V^{-} - E^{-}_{rms}\right) \tag{5.47}$$

while

$$P^{-}_{set} = -\frac{r_l}{\omega_g L_l} Q^{-}_{set}, \tag{5.48}$$

where E^{-}_{rms} is a constant and k_{PVU}, k_{IVU} are the proportional and integral gains of the PI controller. Note that (5.48) represents a decoupling solution based on the line impedance parameters [33, 136]. However, accurate knowledge of r_l and L_l is not essential since an estimation of the term $\frac{r_l}{L_l}$ is enough. Through (5.47) and (5.48), the required negative sequence reference powers to eliminate the PCC negative sequence voltage are acquired. As it is obvious from (5.47)-(5.48), considering initially a balanced system, as long as there is no negative sequence voltage at the PCC (balanced system), $Q^{-}_{set} = P^{-}_{set} = 0$ and thus the inverter injects only positive sequence power. Note that a superiority of the proposed controller compared to existing approaches, is that when the capacity is not enough to track P^{-}_{set} and Q^{-}_{set}, priority is given to the current limitation property proven in sec. 5.3.3.4, without switching to different control dynamics or suffering from integrator wind-up issues.

It should be highlighted that methodologies that take into account the line impedance have been also applied for positive sequence voltage support, see for example [32, 134]. In this case, decoupling based on the line impedance parameters is achieved in the positive sequence as well and thus, (5.45) does not represent an assumption since it expresses accurately the voltage difference. However, since the FRT is an essential standard in most of the grid codes nowadays, it is adopted for the positive sequence voltage support in this controller, as in [33]. Note though that if required, P^{+}_{set} and Q^{+}_{set} formulas can be easily modified and be determined according to r_l and L_l instead of the FRT guidelines.

5.3.4.2 Online adaptation of I_{grms}^{max+} and I_{grms}^{max-}

With the proposed controller, the grid current limitation is inherently applied through the outer-loop controllers and not through saturated integrators in the inner loop. Thus, a proper selection of the maximum available current in each sequence needs to take place by proposing an algorithm that defines the values I_{grms}^{max+} and I_{grms}^{max-}. To realize this current allocation, priority is given to the positive sequence voltage regulation by means of supporting V_c^+ so that when $V^+ < 0.9E_{rms}^+$, we can achieve $V_c^+ \geq 0.9E_{rms}^+$ or $V_c^+ - V^+ \geq 0.9E_{rms}^+ - V^+$ which based on [137], can be rewritten as

$$\frac{P^+ r_g + Q^+ x_{L_g}}{3V^+} \geq 0.9E_{rms}^+ - V^+. \tag{5.49}$$

This methodology is employed since in contrary to [117], the aim here is to provide a non dynamic method of adjusting the positive and negative sequence maximum currents and furthermore, V_g^+ is considered unknown. Otherwise the positive sequence voltage support could be applied at the PCC voltage. By recalling the P_{set}^+ and Q_{set}^+ formulas derived from (5.46), expression (5.49) results to

$$\frac{S_{max}^+ \left(\sqrt{1-\rho^2 k^2} r_g + k\rho\omega_g L_g\right)}{3V^+} \geq 0.9E_{rms}^+ - V^+$$

which can be equivalently written as

$$I_{grms}^{max+} \geqslant \frac{E_{rms}^+ (\rho - 0.1)}{\sqrt{1-k^2\rho^2} r_g + k\rho\omega_g L_g}.$$

Thus, we can select

$$I_{grms}^{max+} = \frac{E_{rms}^+ (\rho - 0.1)}{\sqrt{1-k^2\rho^2} r_g + k\rho\omega_g L_g}, \tag{5.50}$$

where ρ is the p.u. voltage drop of the RMS voltage at the PCC. The derivation of (5.50) is analytically given in the Appendix. Note that (5.50) is valid only when $0.5 \geq \rho \geq 0.1$ (from (5.46)) and $V^- > E_{rms}^-$ since in the absence of negative sequence voltage, all the available current is assigned to the positive sequence. I_{grms}^{max+} is then passed through a saturator that ensures that $I_{grms}^{max+} \in [0, I_{grms}^{max}]$. Opposed to conventional current-limiting control schemes that apply a saturator on the current dynamics, here the function being saturated is not dynamic and thus does not suffer from integrator wind-up. Then, according to the theory presented in [109, 111, 116], which shows that the total current of any phase has a maximum value $I_{grms}^{max} \leqslant I_{grms}^+ + I_{grms}^-$ even if unbalanced current is injected to the grid, I_{grms}^{max-} can be set as

$$I_{grms}^{max-} = I_{grms}^{max} - I_{grms}^{max+} \tag{5.51}$$

[34, 115, 138, 139]. When current allocation has taken place, the value S_{max}^+ can be easily selected as $3V^+ I_{grms}^{max+}$ and the positive sequence reference powers can be

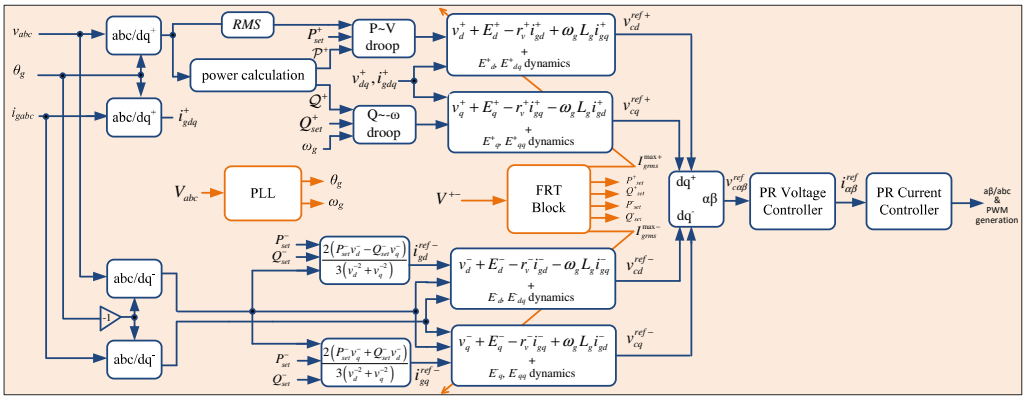

Figure 5.6: Implementation diagram of the proposed controller

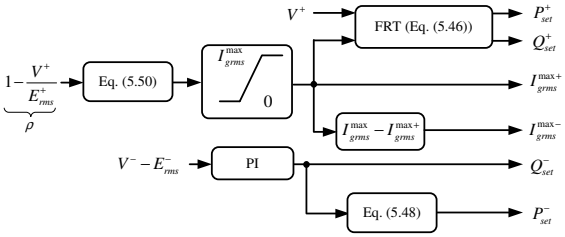

Figure 5.7: FRT Block

calculated according to the FRT guidelines (5.46), while when $I_{grms}^{max+} = I_{grms}^{max}$ from (5.50) or due to the saturator, then $S_{max}^{+} = (1-\rho)\, S_{max}$ and $I_{grms}^{max-} = 0$. Since the maximum current for each sequence is now defined according to the voltage drop, the proposed controller dynamics (5.34)-(5.35) and (5.41)-(5.42) can be adapted online through the expressions $E_{max}^{+} = \sqrt{2} r_v^{+} I_{grms}^{max+}$, $E_{max}^{-} = r_v^{-} I_{grms}^{max-}$. Opposed to the work presented in [45, 140], here the proposed design enables the adaptation of the controller parameters E_{max}^{+} and E_{max}^{-}, and the controller states are attracted on any ellipse E with varying horizontal radius (E_{max}^{+} or E_{max}^{-}) as analytically proven in sec. 5.3.3.2. The positive sequence maximum current is set as the amplitude and not the RMS value in order to allow $P, Q \in [0, S_{max}^{+}]$ for the FRT. However, since it holds that $P_{set}^{+} = \sqrt{\left(S_{max}^{+}\right)^2 - \left(Q_{set}^{+}\right)^2}$, the maximum RMS current will never be violated at the steady-state while during transients, through the input-to-state stability property of the closed-loop current dynamics, it is proven that it remains below the value $\sqrt{2} I_{grms}^{max} = 1.4 I_{grms}^{max}$ (worst-case scenario), which commercial inverters can handle [118]. Finally, during normal grid conditions, I_{grms}^{max+} can be simply selected as $I_{grms}^{max}/\sqrt{2}$ to ensure current limitation under the value I_{grms}^{max} at all times. The implementation of the proposed control approach is depicted in Fig. 5.6, where the control part generating the positive and negative sequence reference powers and the maximum currents is denoted as the FRT block, which is shown in Fig. 5.7.

5.3.5 Stability analysis

After applying the proposed controller into the three-phase inverter system, the closed-loop dynamics are given by (5.34)-(5.37) and (5.41)-(5.44). The state vector of the closed-loop system, for both sequences, takes the form $x^{+-} = \left[\left(x_1^{+-}\right)^T \left(x_2^{+-}\right)^T \right]^T$, where $x_1^{+-} = \left[\begin{array}{cc} i_{gd}^{+-} & i_{gq}^{+-} \end{array} \right]^T$, $x_2^{+-} = \left[\begin{array}{cccc} E_d^{+-} & E_{dq}^{+-} & E_q^{+-} & E_{qq}^{+-} \end{array} \right]^T$. Consider now any steady-state equilibrium point $x_e^{+-} = \left[\left(x_{1e}^{+-}\right)^T \left(x_{2e}^{+-}\right)^T \right]^T = \left[i_{gde}^{+-} \, i_{gqe}^{+-} \, E_{de}^{+-} \, E_{dqe}^{+-} \, E_{qe}^{+-} \, E_{qqe}^{+-} \right]^T$ with $E_{de}^{+-}, E_{qe}^{+-} \in \left(-E_{max}^{+-}, E_{max}^{+-}\right)$, i.e. $E_{dqe}^{+-}, E_{qqe}^{+-} \in (0, 1]$, where the voltage and frequency at the PCC are considered constant (according to the different time scales approach explained in the Appendix) and the negative sequence reference currents are assumed constant. By defining $\tilde{x}_1^{+-} = x_1^{+-} - x_{1e}^{+-}$ and $\tilde{x}_2^{+-} = x_2^{+-} - x_{2e}^{+-}$, then the closed-loop dynamics (5.34)-(5.37) and (5.41)-(5.44) can be written in the following interconnected system form

$$\dot{\tilde{x}}_1^{+-} = f_1\left(\tilde{x}_1^{+-}, \tilde{x}_2^{+-}\right) \tag{5.52}$$

$$\dot{\tilde{x}}_2^{+-} = f_2\left(\tilde{x}_2^{+-}\right), \tag{5.53}$$

where the equilibrium has been shifted at the origin. According to Theorem 4 in sec. 3.4, which is analytically given in Lemma 5.6 in [119], if the system (5.52) with the $\tilde{x}_2^{+-}$ as input, is locally input-to-state stable and the origin of (5.53) is asymptotically stable, then the origin of the interconnected system (5.52)-(5.53) is asymptotically stable.

System (5.52) is linear and can be written from (5.43)-(5.44) as

$$\left[\begin{array}{c} \dot{\tilde{i}}_{gd}^{+-} \\ \dot{\tilde{i}}_{gq}^{+-} \end{array} \right] = \left[\begin{array}{cc} -\frac{r_g + r_v^{+-}}{L_g} & 0 \\ 0 & -\frac{r_g + r_v^{+-}}{L_g} \end{array} \right] \left[\begin{array}{c} \tilde{i}_{gd}^{+-} \\ \tilde{i}_{gq}^{+-} \end{array} \right] + \left[\begin{array}{c} \frac{\tilde{E}_d^{+-}}{L_g} \\ \frac{\tilde{E}_q^{+-}}{L_g} \end{array} \right].$$

Since the characteristic matrix of the grid current dynamics is diagonal with all elements being negative, then the system (5.52) is bounded-input bounded state stable with respect to the input $\left[\frac{\tilde{E}_d^{+-}}{L_g} \; \frac{\tilde{E}_q^{+-}}{L_g} \right]^T$, which means that (5.52) is ISS. Then, for the dynamics of the control system (5.34)-(5.37) and (5.41)-(5.42) the Jacobian matrix of (5.53) becomes

$$A^{+-} = \left[\begin{array}{cc} A_1^{+-} & 0_{2\times 2} \\ 0_{2\times 2} & A_2^{+-} \end{array} \right],$$

where

$$A_1^{+-} = \begin{bmatrix} -\alpha^{+-}\left(E_{dqe}^{+-}\right)^2 - 2k_{we}\frac{\left(E_{de}^{+-}\right)^2}{\left(E_{max}^{+-}\right)^2} & -2k_{we}E_{dqe}^{+-}E_{de}^{+-} \\ \frac{\alpha^{+-}E_{de}^{+-}E_{dqe}^{+-}-2k_{we}E_{de}^{+-}E_{dqe}^{+-}}{\left(E_{max}^{+-}\right)^2} & -2k_{we}\left(E_{dqe}^{+-}\right)^2 \end{bmatrix}$$

$$A_2^{+-} = \begin{bmatrix} -\beta^{+-}\left(E_{qqe}^{+-}\right)^2 - 2k_{we}\frac{\left(E_{qe}^{+-}\right)^2}{\left(E_{max}^{+-}\right)^2} & -2k_{we}E_{qqe}^{+-}E_{qe}^{+-} \\ \frac{\beta^{+-}E_{qe}^{+-}E_{qqe}^{+-}-2k_{we}E_{qe}^{+-}E_{qqe}^{+-}}{\left(E_{max}^{+-}\right)^2} & -2k_{we}\left(E_{qqe}^{+-}\right)^2 \end{bmatrix}$$

with $\alpha^+ = \frac{c_{pd}3nv_d^+}{2r_v^+}$, $\beta^+ = \frac{c_{pq}3mv_d^+}{2r_v^+}$, $\alpha^- = \frac{c_{nd}}{r_v^-}$ and $\beta^- = \frac{c_{nq}}{r_v^-}$. Since A^{+-} is a block diagonal matrix, we can investigate the system matrices A_1^{+-} and A_2^{+-} independently. The characteristic polynomials of these two matrices take the form

$$\lambda^2 + \left(2k_{we} + \alpha^{+-}\left(E_{dqe}^{+-}\right)^2\right)\lambda + 2k_{we}\left(E_{dqe}^{+-}\right)^4\alpha^{+-} + \frac{2k_{we}\left(E_{de}^{+-}\right)^2\left(E_{dqe}^{+-}\right)^2\alpha^{+-}}{\left(E_{max}^{+-}\right)^2} = 0$$

$$\lambda^2 + \left(2k_{we} + \beta^{+-}\left(E_{qqe}^{+-}\right)^2\right)\lambda + 2k_{we}\left(E_{qqe}^{+-}\right)^4\beta^{+-} + \frac{2k_{we}\left(E_{qe}^{+-}\right)^2\left(E_{qqe}^{+-}\right)^2\beta^{+-}}{\left(E_{max}^{+-}\right)^2} = 0.$$

Hence, the condition to guarantee asymptotic stability for any equilibrium point x_e^{+-} of the closed-loop system in the bounded operating range $E_{de}^{+-}, E_{qe}^{+-} \in (-E_{max}^{+-}, E_{max}^{+-})$, is

$$\alpha^+, \alpha^-, \beta^+, \beta^- > 0,$$

which is always true regardless of the voltage level. Opposed to the majority of the conventional approaches that use root-locus analysis and guarantee stability of a given equilibrium point under the specific parameters of the inverter and the grid, here the proposed controller guarantees asymptotic stability of any equilibrium point x_e^{+-} in the bounded operating range. In addition, an inherent current-limiting property and an enhanced operation under grid faults is achieved in a unified control structure, which highlight the novelties of the proposed control scheme.

5.3.6 Validation through real-time results

In order to validate the proposed control approach, a three-phase inverter connected to the grid, as shown in Fig. 5.5, and equipped with the proposed controller, is tested using an OPAL-RT OP4500 real-time digital simulator. The parameters of the controller and the power system are given in Tab. 5.2. In the sequel, the performance of the proposed controller will be showcased under various normal and abnormal grid conditions.

Table 5.2: System and controller parameters for real-time simulations

Parameters	Values	Parameters	Values
L, L_g	2.2 mH	Z_l	$0.9 + 1.256j\,\Omega$
r, r_g	0.5 Ω	V_{dc}	400 V
C	1 μF	S_{max}	3.3 KVA
E^+_{rms}	110 V	I^{max}_{grms}	10 A
E^-_{rms}	0 V	ω^*	314.15 rad/s
ω_g	314.03 rad/s	k_{we}	1000
n	0.00333	m	0.0019
r^+_v	30 Ω	r^-_v	10 Ω
c_{pd}	780	c_{pq}	3415
c_{nd}	250	c_{nq}	125
k_{PVU}	2	k_{IVU}	20
k_{PCC}	0.2	k_{RCC}	2
k_{PVC}	1.5	k_{RVC}	15

5.3.6.1 Balanced operation

Firstly, the operation of the grid-connected inverter equipped with the proposed controller will be tested under balanced grid conditions. The switch between the LCL filter and the PCC is initially open, and then closes at $t = 0.1$ s, while at the same time the controller is enabled with the reference values P^+_{set} and Q^+_{set} having the values of 600 W and 0 Var, respectively. The controller operates initially in the PQ-set mode and regulates P^+ and Q^+ to their desired values, as shown in Fig. 5.8. In the same figure, V^+_c and I^+_{grms} can be observed as well. At $t = 1$ s, Q^+_{set} is changed to 50 Var and the reactive power injection is accordingly modified while at $t = 2$ s, P^+_{set} is set as 800 W. Since the PQ-set operation is now verified, at $t = 4$ s and $t = 5$ s, the real and reactive power droop control modes are enabled respectively. One can see that both the real and the reactive power drop since at that time, the grid operates with a slightly higher value of RMS grid voltage compared to the nominal (110.4 V) and a slightly lower than the nominal grid frequency (49.98 Hz). At $t = 6$ s, a balanced grid voltage drop of 0.4 p.u. is applied in order to test the operation under faulty grid conditions. At the initial transient, it can be observed in Fig. 5.8, that I^+_{grms} reaches the value of 11 A while it never violates the ultimate bound of $\sqrt{2}I^{max}_{grms} = 14$ A. Following to the transient, the RMS value of the grid current is regulated to its maximum value of 10 A, as it has been analytically proven in the controller analysis, while P^+ and $Q^+$are regulated according to the FRT, thus achieving grid support and inverter protection simultaneously. When the fault is self-cleared at $t = 8$ s, P^+ and Q^+ return smoothly to their original values according to the droop control.

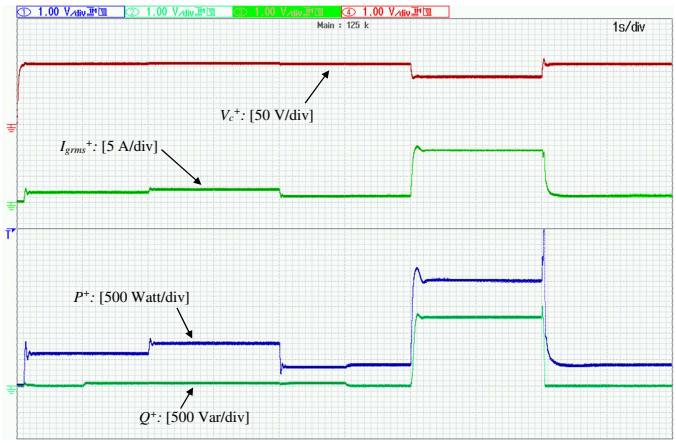

Figure 5.8: Operation under balanced grid conditions with a 0.4 p.u. balanced voltage drop at 6s

5.3.6.2 Operation under single-phase voltage sag

In order to test the operation of the proposed controller under unbalanced faults, a single-phase voltage sag is applied on v_{ga}, with its RMS value dropping by 0.65 p.u. which leads to $V_g^+ \approx 0.78$ p.u., while the inverter is operating with droop control. As it can be observed in Fig. 5.9b, the current allocation algorithm leads the RMS currents to the values $I_{grms}^+ = 6.65$ A and $I_{grms}^- = 3.15$ A. It should be noted that according to the proposed controller operation, the components I_{grms}^+ and I_{grms}^- are tracking their maximum values from (5.50) and (5.51) during voltage drops (unless the desired $V^- = E_{rms}^-$ regulation has been achieved with less than the maximum negative sequence current). Hence, the total current is regulated close to its maximum value I_{grms}^{max} but without exceeding it. The primary objective of the proposed controller is achieved since as it is depicted in Fig. 5.9b, V_c^+ is regulated to $0.9E_{rms}^+$. This verifies the proper selection of the value I_{grms}^{max+} which further leads to the S_{max}^+ calculation, while the rest of the available inverter capacity is assigned to negative sequence current controller so that V^-, shown in Fig. 5.9b, is eliminated as much as possible. Even if the proposed controller does not deal directly with the VUF but aims to increase the positive sequence voltage and eliminate the negative sequence voltage, in this certain scenario, it can be seen in Fig. 5.9c that VUF at the PCC is eliminated by 7% when compared to VUF_{grid}. The real and reactive power components injected to the grid according to (5.46) and (5.47)-(5.48) are depicted in Fig. 5.9a. At the steady-state, P_{set}^- and Q_{set}^- are not tracked since priority is given to the current-limiting property. However, if greater capacity was available, such that $V^- = E_{rms}^-$, P^- and Q^- would be regulated to their reference values. After 1.5 s, the fault is self-cleared and the positive sequence components are driven to their initial values according to droop control while the negative sequence components are driven to 0. Note that during the clearing transient, the value $I_{grms}^+ + I_{grms}^-$ reaches the value 12 A for 10 ms, however, it never exceeds its ultimate bound during transients set at 14 A, as proven in the theoretic analysis.

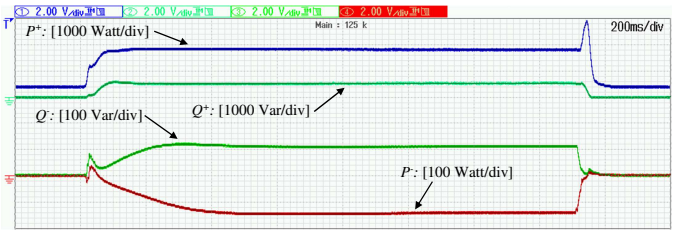

(a) Injected powers

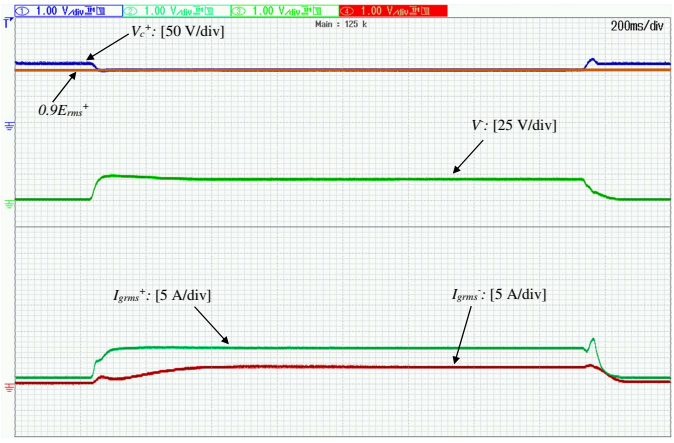

(b) Positive and negative sequence RMS voltages and currents

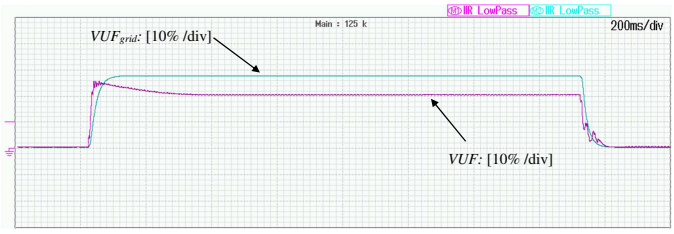

(c) Voltage unbalance factors

Figure 5.9: Operation under single-phase voltage drop ($V_{ga} = 0.35\,\text{p.u.}$)

5.3.6.3 Operation under two-phase voltage sag

To further demonstrate the operation of the proposed controller under unbalanced faults, a two-phase voltage sag is now applied, with the RMS values of v_{ga} and v_{gc} dropping so that $V_{ga} = 0.73\,\text{p.u.}$ and $V_{gc} = 0.65\,\text{p.u.}$ leading to $V_g^+ \approx 0.8\,\text{p.u.}$, while the inverter is operated in the droop control mode. As mentioned before, the maximum current assigned to the positive sequence controller is tracked by the controller leading to $I^+_{grms} = 6.1\,\text{A}$ in order to optimize the support operation and thus, V_c^+ is regulated to $0.9E^+_{rms}$, as shown in Fig. 5.10b. The the rest of the available current, is assigned to the negative sequence current controller which leads to $I^-_{grms} = 3.7\,\text{A}$ thus, managing to eliminate the negative sequence voltage, shown in Fig. 5.10b. Hence, the total current never violates its maximum value $I^{max}_{grms} = 10\,\text{A}$. The powers injected to the grid in both sequences can be observed in Fig. 5.10a

while the VUF is eliminated by 7% compared to the VUF_{grid}, as depicted in Fig. 5.10c. After 1.5 s, the fault is self-cleared and the positive sequence components are driven to their initial values according to droop control while the negative sequence components are driven to 0. It is underlined that during the clearing transient, the addition $I^{+}_{grms} + I^{-}_{grms}$, reaches the value of 11.5 A for less than 10 ms without ever violating the ultimate bound for transient currents, set at 14 A.

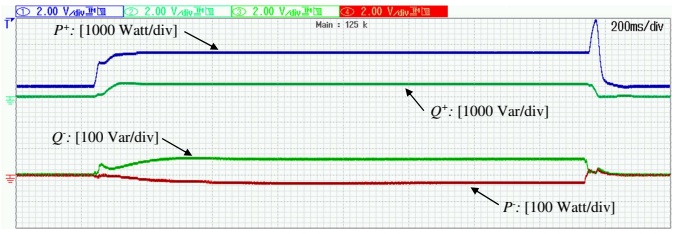

(a) Injected powers

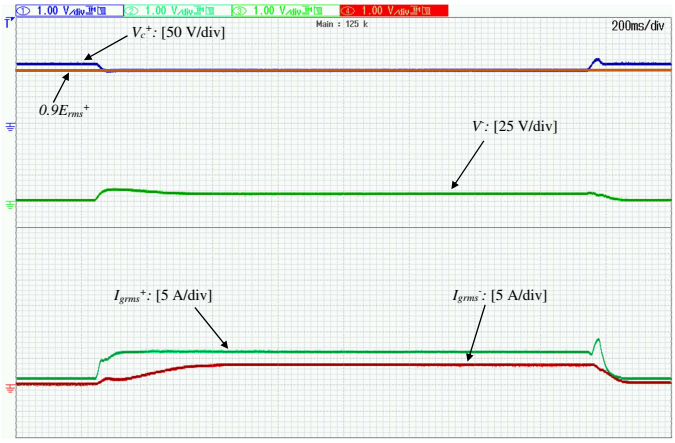

(b) Positive and negative sequence RMS voltages and currents

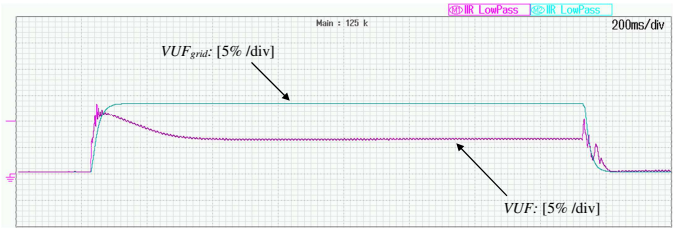

(c) Voltage unbalance factors

Figure 5.10: Operation under two-phase voltage drop ($V_{ga} = 0.73$ p.u. and $V_{gc} = 0.65$ p.u.)

5.4 Conclusions

In this chapter, the current-limiting control design of three-phase grid-connected inverters was investigated. Initially, a current-limiting droop controller was developed for three-phase inverters. The proposed control approach allows the inverter to either track the set reference values for the real and reactive power or to operate with a droop control technique to support the grid. Furthermore, a grid current-limiting property was shown to be sustained at all times by introducing a virtual resistance and was analytically proven using the input-to-state stability (ISS) property of the closed-loop system. This current limitation ensures a safe operation even in the case where voltage dips occur in the grid, without the need of saturation units that can lead to instability. Finally, asymptotic stability of the closed-loop system was proven without assuming knowledge of the system parameters. The proposed control approach was validated through extensive real-time simulation results. In the sequel, aiming to address the operation of three-phase inverters during unbalanced grid faults, a novel control concept was proposed, which inherits a current-limiting property to three-phase grid-connected droop-controlled inverters. The proposed control scheme complies with the "voltage support concept" to achieve grid voltage support under both balanced and unbalanced grid faults. To accomplish the desired tasks, two novel outer-loop controllers were applied to the positive and the negative sequence systems, while the boundedness of the grid current was proven through closed-loop system analysis. A novel way to divide the rated inverter current into the positive and the negative sequence current components was proposed to enable the desired voltage support operation. Finally, asymptotic stability of the closed-loop system was proven for inverters that adopt the proposed control scheme. The proposed controller was verified through extended real-time simulation results.

6 Inverter-based self-protected microgrids

6.1 Motivation and novel outcome

As it was discussed in the literature review of chapter 2, the increasing integration of DERs into power systems has driven to a paradigm shift in the power system structure and operation. In this "smart grid" era, advanced control and protection techniques are required [8]. In the same context, a vital component of the smart grid is the "microgrid" which aims to locally utilize the DERs' capabilities. In particular, a microgrid is a part of a power system that can operate either connected to the the grid or as an island. Hence, sophisticated control schemes are required to guarantee the proper microgrid operation. Up to recently, the islanded operation of parts of the power system was not allowed by the Grid Codes and anti-islanding techniques were required for every DER. However, with the recent advances in the control schemes of inverter-interfaced DERs, which can accomplish tasks like load voltage and frequency regulation and proportional power sharing, the islanded microgrid operation is nowadays actively investigated in order to improve smart grid's reliability. Nevertheless, the safe operation of inverter-based microgrids under faulty or overload conditions has not been sufficiently and rigorously investigated [107].

Aiming to tackle the safe operation of inverter-based microgrids, the concept of droop-controlled inverters with inherent current limitation should be revisited so that it can be applied to islanded systems. The advanced current limitation offered through the BIC structure is expected to bring significant benefits in inverter-based microgrid applications, where the conventional current limitation approaches may lead to undesirable performance [46]. Moreover, the investigation of stability of islanded microgrids is a challenging task due to the absence of a stiff grid to stabilize voltage and frequency. It is noteworthy that similarly to the case of three-phase grid-connected inverter applications, the SRF (dq) framework is commonly used for modeling and control of three-phase microgrids. Nevertheless, since in an inverter-based microgrid each inverter operates with its own phase shift, each inverter has its own dq alignment. Hence, to investigate the microgrid closed-loop system stability, the global DQ framework concept should be considered based on the rotational angle difference of each inverter in the inverter-based microgrid [6].

To deal with the above mentioned challenges, in sec. 6.2, a new current-limiting droop controller is proposed for three-phase inverters operating in parallel. Droop

control is employed to ensure the proportional power sharing between the parallel inverters, while an inherent current-limiting property is achieved through the control design. Furthermore, small-signal analysis is performed to examine the closed-loop system stability of two parallel inverters equipped with the proposed controller. In the sequel, on top of the control scheme proposed in sec. 6.2, a simpler control scheme should be developed while a more accurate model of an inverter-based microgrid with lines between the PCC of each inverter and the load should be considered. Moreover, the microgrid stability analysis should be performed in a more generalized manner, i.e. without considering an exemplary case of two inverter-interfaced DERs operating in parallel. Hence, in sec. 6.3, a novel droop controller that ensures the desired inverter current limitation and guarantees the stable operation of inverter-based microgrids under extreme load conditions is proposed. Opposed to existing dq framework-based droop controllers that align the output voltage on d axis, in the proposed scheme, the inverter current is aligned on d axis in order to achieve two main goals: i) limitation of the RMS value of each inverter current during transients, without a need for saturation units that may lead to instability and that usually require an online adaptation technique to fully utilize inverter capacity and ii) a rigorous proof of closed-loop system stability for the entire microgrid. In particular, the proposed approach significantly simplifies the stability analysis of the microgrid, since it can be investigated through a Jacobian matrix of reduced size.

6.2 Current-limiting droop control of three-phase inverters operating in parallel

6.2.1 System modeling

The system under consideration consists of n three-phase inverters operating connected to a common load bus through an LC filter, as depicted in Fig. 6.1. The inductance of the filter is denoted as L_i, with its parasitic resistance being ignored due to its small value, while the filter capacitor is denoted as C_i where i denotes the number of the inverter with $i \in [1, \ldots, n]$. The inverter voltage in the natural reference framework is denoted as v_{iabc} and the inverter current is given as i_{iabc} while the load voltage and current are denoted as v_{Labc} and i_{Labc}, respectively. The contribution to the total load current from each inverter is given as $i_{Liabc.}$ Following the synchronous reference frame theory proposed in [48] and thoroughly presented in [49], the $abc/dq0$ transformation is described from the matrix

$$T_{\alpha\beta} = \frac{2}{3}\begin{bmatrix} \sin\theta_a & \sin(\theta_a - 120) & \sin(\theta_a + 120) \\ \cos\theta_a & \cos(\theta_a - 120) & \cos(\theta_a + 120) \\ 0.5 & 0.5 & 0.5 \end{bmatrix},$$

where θ_a is the angle between phase a and the α axis, followed by the rotating

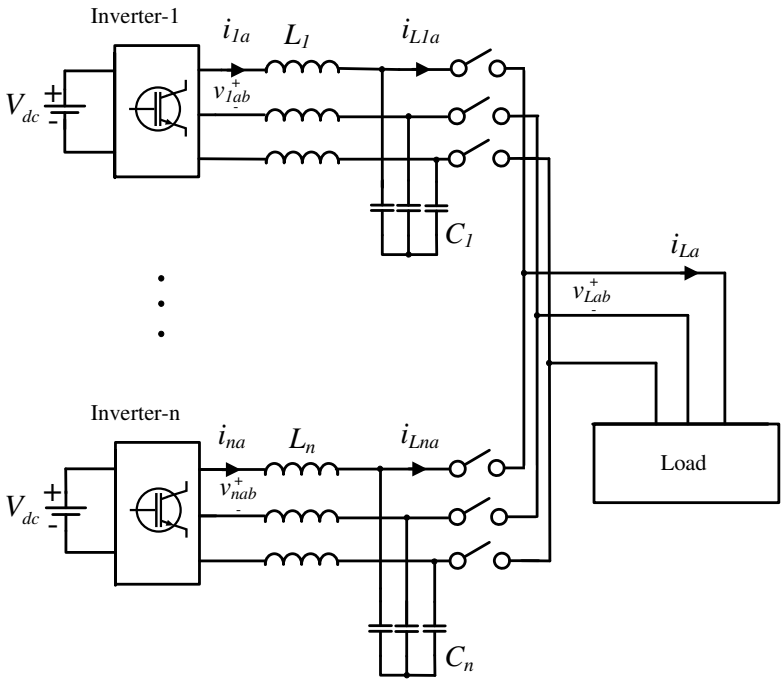

Figure 6.1: Parallel inverters under consideration

transformation

$$T_{dq} = \begin{bmatrix} \cos\theta_i & \sin\theta_i \\ -\sin\theta_i & \cos\theta_i \end{bmatrix},$$

where θ_i is the angle of each inverter. One may notice that a different dq transformation is introduced here, compared to the one used in chapter 5. This transformation is selected in this chapter, since it is more widely used in the literature. Nevertheless, the control design is not restricted to a specific rotational transformation, as long as the control parameters are accordingly selected. The dynamic equations for any of the n parallel three-phase inverters in the dq framework can be written as

$$L_i \frac{di_{id}}{dt} = v_{id} - v_{Lid} + \omega_i L_i i_{iq} \tag{6.1}$$

$$L_i \frac{di_{iq}}{dt} = v_{iq} - v_{Liq} - \omega_i L_i i_{id} \tag{6.2}$$

$$C_i \frac{dv_{Lid}}{dt} = i_{id} - i_{Lid} + \omega_i C_i v_{Liq} \tag{6.3}$$

$$C_i \frac{dv_{Liq}}{dt} = i_{iq} - i_{Liq} - \omega_i C_i v_{Lid}, \tag{6.4}$$

where ω_i is the angular frequency of each inverter and the inverter voltages v_{id} and v_{iq} represent the control inputs.

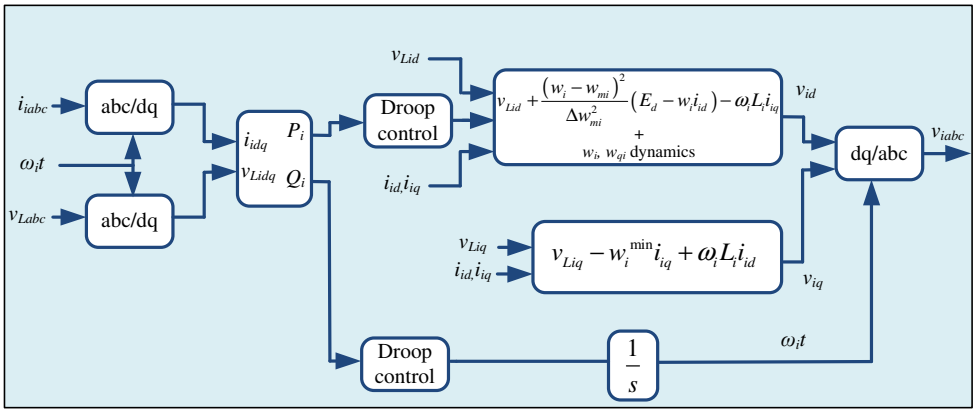

Figure 6.2: The proposed controller

6.2.2 The proposed controller design

The proposed controller for each inverter operating in parallel takes the form

$$v_{id} = v_{Lid} + \frac{(w_i - w_{mi})^2}{\Delta w_{mi}^2}(E_d - w_i i_{id}) - \omega_i L_i i_{iq} \tag{6.5}$$

$$v_{iq} = v_{Liq} - w_i^{min} i_{iq} + \omega_i L_i i_{id} \tag{6.6}$$

where E_d is the nominal load voltage on d axis which for the used SRF transformation ($\theta_\alpha = 90^o$) is derived as $E_d = \sqrt{2}E_{rms}$, with E_{rms} being a constant representing the nominal RMS load voltage. The term $\frac{(w_i - w_{mi})^2}{\Delta w_{mi}^2}$ is used in order to achieve a smooth connection thus avoiding any possible overvoltage that could arise due to the constant parameter $E_{d.}$ The terms $\omega_i L_i i_{iq}$ and $\omega_i L_i i_{id}$ represent the decoupling terms and w_i^{min} is the minimum value of the virtual resistance w_i applied to the d axis, which changes according to the nonlinear expressions

$$\dot{w}_i = -c_{wi} f_i(P_i) w_{qi}^2 \tag{6.7}$$

$$\dot{w_{qi}} = \frac{c_{wi}(w_i - w_{mi})w_{qi}}{\Delta w_{mi}^2} f_i(P_i) - k_w \left(\frac{(w_i - w_{mi})^2}{\Delta w_{mi}^2} + w_{qi}^2 - 1 \right) w_{qi} \tag{6.8}$$

where c_{wi} and k_w are positive constants. As it has been highlighted, through this structure, $w_i \in [w_i^{min}, w_i^{max}] = [w_{mi} - \Delta w_{mi}, w_{mi} + \Delta w_{mi}]$, while $w_{mi} = \frac{w_i^{min} + w_i^{max}}{2}$ and $\Delta w_{mi} = \frac{w_i^{max} - w_i^{min}}{2}$. The function $f_i(P_i)$ inherits the real power droop control expression, which is applied in the proposed controller through the virtual resistance

dynamics and takes the form

$$f_i(P_i) \;=\; E_{rms} - V_L - n_{pi}P_i \tag{6.9}$$

where $P_i = \frac{3}{2}\left(v_{Lid}i_{id} + v_{Liq}i_{iq}\right)$. The reactive power droop control is applied through the SRF transformation and is described from

$$\omega_i = \omega^* + m_{qi}Q_i \tag{6.10}$$

where $Q_i = \frac{3}{2}\left(v_{Liq}i_{id} - v_{Lid}i_{iq}\right)$. In the droop expressions, n_{pi} represents the real power droop coefficient, m_{qi} represents the reactive power droop coefficient, while V_L is the RMS load voltage which is calculated from $\sqrt{2}V_L = \sqrt{v_{Lid}^2 + v_{Liq}^2}$ and ω^* is the nominal angular frequency. One can see that real power droop control is applied through the d component of the inverter voltage (which is a control input of the system) and reactive power droop is applied through the angular frequency dynamics. The $P \sim V, Q \backsim -\omega$ droop expressions are used in this controller since the universal droop controller from [79] is adopted. The implementation of the proposed controller is shown in Fig. 6.2. As highlighted before, for the virtual resistance dynamics in (6.7)-(6.8), the BIC setup from [56] is employed to guarantee the boundedness of the virtual resistance w_i. This property will lead to the boundedness of the inverter current for every three-phase inverter as it will be analytically shown in the analysis that follows.

6.2.3 Stability analysis

6.2.3.1 Current-limiting property

Applying the proposed controller (6.5)-(6.6) into the system dynamics (6.1)-(6.4), the closed-loop system takes the form depicted in Fig. 6.3. The inverter current dynamics are

$$L_i\frac{di_{id}}{dt} \;=\; \frac{\left(w_i - w_{mi}\right)^2}{\Delta w_{mi}^2}\left(E_d - w_i i_{id}\right) \tag{6.11}$$

$$L_i\frac{di_{iq}}{dt} \;=\; -w_i^{min} i_{iq}. \tag{6.12}$$

This also verifies that the steady-state currents take the values $i_{ide} = \frac{E_d}{w_i}$ and $i_{iqe} = 0$. Now, let us consider the Lyapunov function candidate

$$V = \frac{1}{2}L_i i_{id}^2 + \frac{1}{2}L_i i_{iq}^2,$$

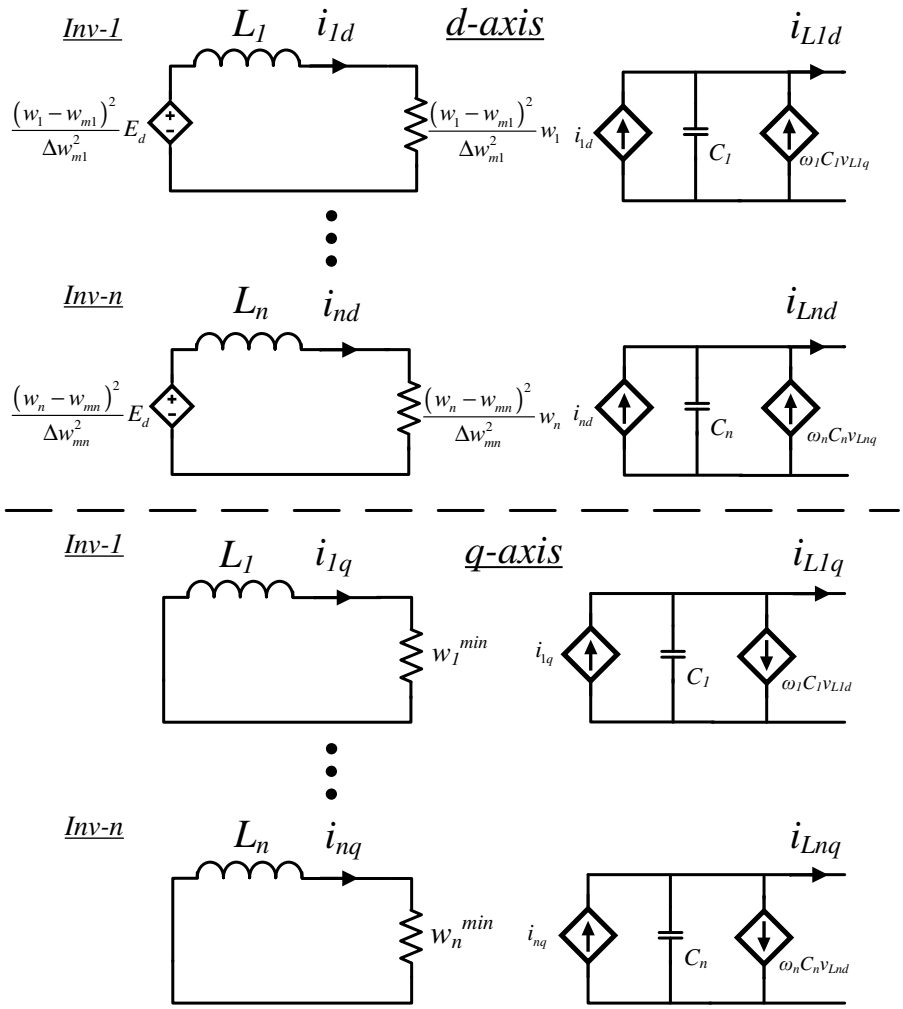

Figure 6.3: Equivalent circuit of the closed-loop system

which represents the energy stored in each inductor. Its time derivative takes the form

$$\begin{aligned}
\dot{V} &= \frac{(w_i - w_{mi})^2}{\Delta w_{mi}^2}\left(E_d i_{id} - w_i i_{id}^2\right) - w_i^{min} i_{iq}^2 \\
&\leq \frac{(w_i - w_{mi})^2}{\Delta w_{mi}^2}\left([E_d\, 0]\begin{bmatrix} i_{id} \\ i_{iq} \end{bmatrix} - w_i^{min}\left(i_{id}^2 + i_{iq}^2\right)\right) \\
&\leq \frac{(w_i - w_{mi})^2}{\Delta w_{mi}^2}\left(-w_i^{min}\left\|I_i\right\|_2^2 + \left\|E\right\|_2\left\|I_i\right\|_2\right)
\end{aligned}$$

where $I_i = [i_{id}\ i_{iq}]^T$ and $E = [E_d\ 0]^T$. Thus, it is concluded that

$$\dot{V} < 0, \forall \left\|I_i\right\|_2 > \frac{\left\|E\right\|_2}{w_i^{min}}. \tag{6.13}$$

Furthermore, taking into account the relation between the dq quantities and the RMS values

$$\begin{aligned} \|I_i\|_2 &= \sqrt{i_{id}^2 + i_{iq}^2} = \sqrt{2} I_{irms} \\ \|E\|_2 &= \sqrt{E_d^2} = E_d = \sqrt{2} E_{rms} \end{aligned}$$

and since (6.13) holds true, if initially $I_{irms}(0) \leq \frac{E_{rms}}{w_{min}}$, then

$$I_{irms}(t) \leq \frac{E_{rms}}{w_i^{min}}, \forall t \geq 0. \tag{6.14}$$

By selecting $w_i^{min} = \frac{E_{rms}}{I_{irms}^{max}}$ then $I_{irms}(t) \leq I_{irms}^{max}$, $\forall t \geq 0$ for a given maximum value of the RMS current I_{irms}^{max}. Since the boundedness in (6.14) is proven independently from the load voltage or frequency, the RMS inverter current can reach but never exceed its set maximum value, for any $t > 0$. According to this, the controller variable I_{irms}^{max} can be selected by the control operator in order to ensure a current limitation under this threshold value at all times, even under transients and for any type of load.

6.2.3.2 Small-signal stability analysis

Although a current-limiting property is guaranteed for every inverter, the stability of multiple inverters operating in parallel has not been proven yet. In order to evaluate the proposed controller in terms of the closed-loop system stability, an exemplary case of two three-phase inverters operating in parallel is considered for simplicity, although the same approach can be extended to multiple parallel inverters. The state vector of the closed-loop system when considering two parallel three-phase inverters feeding a resistive load is $x = [i_{1d}\, i_{2d}\, i_{1q}\, i_{2q}\, v_{Ld}\, v_{Lq}\, w_1\, w_2\, w_{q1}\, w_{q2}]^T$. Note that, as shown in Fig. 6.1, both inverters have access to the common load voltage and additionally i_{iqe} becomes zero at the steady-state. This means that at the steady-state, when power sharing is achieved and all frequencies have been synchronized, the dq axes of every inverter will be aligned to each other and will have an angle difference δ_e compared to the global reference frame, where v_{Ld} and v_{Lq} is calculated. At this global reference frame, the capacitor voltage is aligned on d axis ($v_{Lqe} = 0$). Then, the Jacobian matrix of the closed-loop system takes the form

$$A = \begin{bmatrix} A_T & 0_{8\times 1} & 0_{8\times 1} \\ A_1 & -2k_w w_{q1e}^2 & 0 \\ A_2 & 0 & -2k_w w_{q2e}^2 \end{bmatrix}.$$

However, since in the bounded range of operation it holds $w_i \in (w_i^{min}, w_i^{max})$, then for any equilibrium point x_e with $w_{q1e}, w_{q2e} \in (0, 1]$, the values $-2k_w w_{q1e}^2$ and $-2k_w w_{q2e}^2$ are always negative. Thus, all the eigenvalues of the closed-loop system will be negative if all the eigenvalues of the matrix A_T, analytically shown in

$$A_T = \begin{bmatrix} -\frac{\epsilon^2 w_{1e}}{\Delta w_{m1}^2 L_1} & 0 & 0 & 0 & 0 & 0 & -\frac{\epsilon^2 i_{1de}}{\Delta w_{m1}^2 L_1} & 0 \\ 0 & -\frac{\zeta^2 w_{2e}}{\Delta w_{m2}^2 L_2} & 0 & 0 & 0 & 0 & 0 & -\frac{\zeta^2 i_{2de}}{\Delta w_{m2}^2 L_2} \\ 0 & 0 & -\frac{w_1^{min}}{L_1} & 0 & 0 & 0 & 0 & 0 \\ 0 & 0 & 0 & -\frac{w_2^{min}}{L_2} & 0 & 0 & 0 & 0 \\ \frac{\cos\delta_e}{C_1+C_2} & \frac{\cos\delta_e}{C_1+C_2} & -\frac{\sin\delta_e}{C_1+C_2} & -\frac{\sin\delta_e}{C_1+C_2} & -\frac{1}{R(C_1+C_2)} & \omega_0 & 0 & 0 \\ \frac{\sin\delta_e}{C_1+C_2} & \frac{\sin\delta_e}{C_1+C_2} & \frac{\cos\delta_e}{C_1+C_2} & \frac{\cos\delta_e}{C_1+C_2} & -\omega_0 & -\frac{1}{R(C_1+C_2)} & 0 & 0 \\ \frac{3}{2}c_{w1}n_{p1}\gamma w_{q1e}^2 & 0 & \frac{3}{2}c_{w1}n_{p1}\sigma w_{q1e}^2 & 0 & \alpha_1 c_{w1} w_{q1e}^2 & \beta_1 c_{w1} w_{q1e}^2 & 0 & 0 \\ 0 & \frac{3}{2}c_{w2}n_{p2}\gamma w_{q2e}^2 & 0 & \frac{3}{2}c_{w2}n_{p2}\sigma w_{q2e}^2 & \alpha_2 c_{w2} w_{q2e}^2 & \beta_2 c_{w2} w_{q2e}^2 & 0 & 0 \end{bmatrix} \tag{6.15}$$

(6.15), have negative real parts. To facilitate the representation of A_T, the following notations are considered: $\alpha_i = \frac{3}{2}n_{pi}i_{ide}\cos\delta_e + 1/\sqrt{2}$, $\beta_i = \frac{3}{2}n_{pi}i_{ide}\sin\delta_e$, $\gamma = v_{Lde}\cos\delta_e$, $\sigma = -v_{Lde}\sin\delta_e$, $\epsilon = (w_{1e} - w_{m1})$ and $\zeta = (w_{2e} - w_{m2})$. In order to perform a root-locus analysis for the matrix A_T, the equilibrium point of the closed-loop system, $x_e = [i_{1de}\, i_{2de}\, i_{1qe}\, i_{2qe}\, v_{Lde}\, v_{Lqe}\, w_{1e}\, w_{2e}\, w_{q1e}\, w_{q2e}]^T$ needs to be identified. This is possible through solving the system of equations (6.3)-(6.4) and (6.7)-(6.12), while ω_0 represents the system steady-state frequency at each equilibrium point when considering that synchronization has been achieved. The droop coefficients are calculated from the formulas $n_{pi} = 0.09\frac{E_{rms}}{S_{maxi}}$ and $m_{qi} = 0.01\frac{\omega^*}{S_{maxi}}$. Therefore through root-locus analysis, the closed-loop system stability for the case of two parallel inverters feeding a resistive load and equipped with the proposed controller can be examined, while the considered system parameters are given in Tab. 6.1.

In Fig. 6.4a, the eigenvalues of the closed-loop system for a resistive load with $R = 10\,\Omega$ are depicted for a real power droop percentage (n_{pi}) between 3% and 30%. Since all the eigenvalues have negative real part, from Theorem 1 in sec. 3.1, it is concluded that the closed-loop system is stable around the considered equilibrium point. Furthermore, in Fig. 6.4b, the trajectory of the eigenvalues that are closer to the imaginary axis is depicted, where it can be understood that as n_{pi} gets lower values, eigenvalues tend more close to the unstable region.

Table 6.1: System and controller parameters for simulation results

Parameters	Values	Parameters	Values
L_1, L_2	1.1 mH	C_1, C_2	10 μF
S_{max1}	3300 VA	S_{max2}	1650 VA
ω^*	314.15 rad/s	E_{rms}	110 V
n_{p1}	0.003	m_{q1}	0.000952
n_{p2}	0.006	m_{q2}	0.0019
I_{1rms}^{max}	10 A	I_{2rms}^{max}	5 A
I_{1rms}^{min}-I_{2rms}^{min}	0.14 A	k_w	1000
w_{m1}	394 Ω	w_{m2}	399 Ω

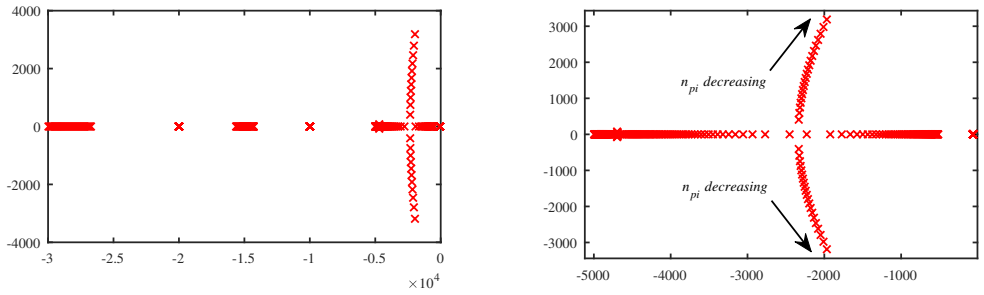

(a) Full spectrum of the eigenvalues

(b) Spectrum of the eigenvalues close to the imaginary axis

Figure 6.4: Spectrum of the closed-loop system eigenvalues as a function of n_{pi} : $\frac{0.03E_{rms}}{S_{maxi}} < n_{pi} < \frac{0.3E_{rms}}{S_{maxi}}$

6.2.4 Verification through simulation results

To validate the performance of the proposed controller, two parallel three-phase inverters connected to a common load bus, as depicted in Fig. 6.1, are simulated in the Matlab/Simulink environment. The system and controller parameters are given in Tab. 6.1. Initially both inverters do not feed the load since their switches are open while at 0.1 s, the first inverter is connected to the load which initially has the value $R = 18\,\Omega$. As it can be seen in Fig. 6.5a, the first inverter quickly regulates its output real power P_1 in order to achieve a load voltage close to its nominal value through droop control. Similarly, in Fig. 6.5b, it is shown that reactive power is accordingly injected to regulate load frequency close to the nominal frequency. The load bus voltage V_L and frequency f are regulated close to their nominal values as depicted in Figures 6.5e and 6.5f, respectively. At 2 s, the second inverter is connected to the common load bus and since a $2:1$ power sharing ratio is desired according to the capacity of the inverters, both real and reactive power are shared proportionally so that $P_1 = 2P_2$ and $Q_1 = 2Q_2$, as it can be observed in Figures 6.5a and 6.5b. To accomplish this, P_1 is reduced, so that both power inverters are stressed equally, whilst as shown in Fig. 6.5e, V_L is now regulated to a higher value which can be understood from (6.9). At 5 s, a load change is experienced and the total load is driven to $R = 10\,\Omega$. As shown in Figures 6.5a and 6.5b, the inverters modify their response, while the power sharing remains accurate. At 7 s, an even higher demand occurs leading the common load to $R = 6\,\Omega$, which requires a power greater than the total capacity of the two parallel inverters $S_{max1} + S_{max2}$. However, according to the controller theoretic analysis, at that time both controller states w_1 and w_2 are driven to their minimum values (11 Ω and 22 Ω respectively, as shown in Fig. 6.5d) thus, limiting the inverter currents I_{1rms} and I_{2rms} to their maximum values as shown in Fig. 6.5c. Hence, the DERs are protected from overcurrents while the load bus voltage V_L drops significantly, since priority is given to protecting the inverter devices. The presented simulation results verify the proportional power sharing and current-limiting capabilities of the proposed controller.

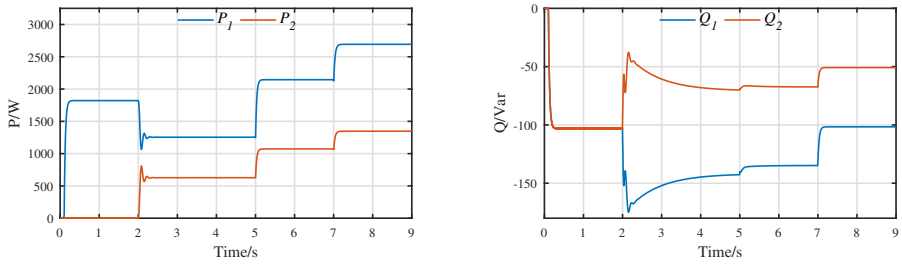

(a) Real Power

(b) Reactive Power

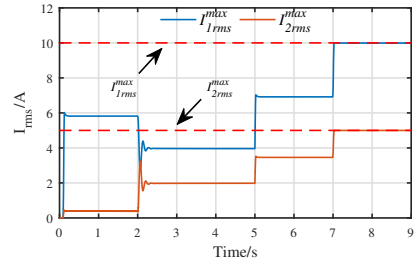

(c) Inverter currents

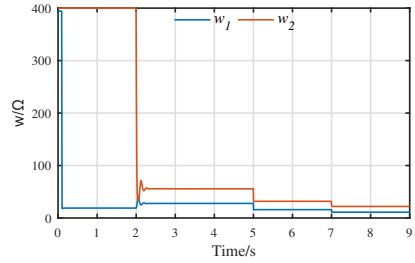

(d) Controller states w_1 and w_2

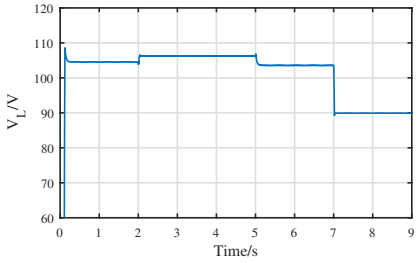

(e) Load RMS voltage

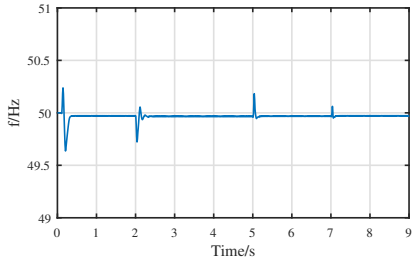

(f) Load frequency

Figure 6.5: Response of two three-phases inverters operating in parallel

6.3 Inverter-based microgrids with inherent current limitation under extreme load conditions

In the previous section, a new current-limiting droop control approach was proposed for three-phase inverters operating in parallel. However, a more realistic microgrid topology should be considered and the microgrid small-signal stability analysis should not investigate a specific setup with two parallel inverters. Thus, in this section, a new droop control approach is proposed for inverter-based microgrids, that guarantees an inverter current limitation and ensures stability for the entire microgrid, under extreme load conditions. This is accomplished by aligning the inverter current on the d axis of the local (inverter) dq framework, in contrast to conventional droop control approaches that align the output voltage on the d axis [6]. In particular, it is analytically proven that the proposed control structure guar-

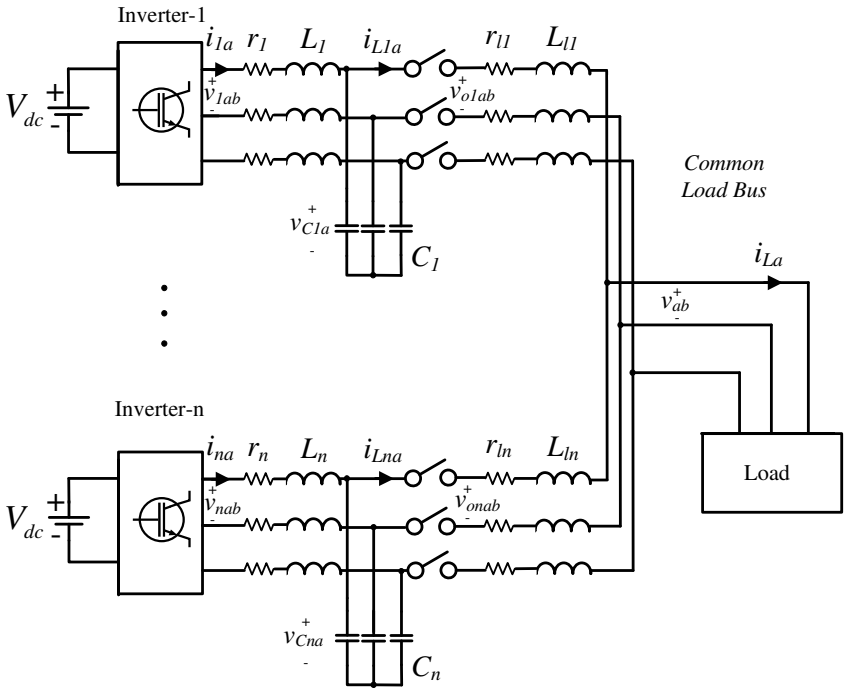

Figure 6.6: Microgrid under consideration

antees an inverter RMS current limitation without the need of adaptive saturation units to fully utilize the inverter capacity and that it further simplifies the Jacobian matrix, the eigenvalues of which should be computed in order to investigate the stability properties of an inverter-based microgrid.

6.3.1 Microgrid modeling

The system under consideration is an inverter-based microgrid consisting of n three-phase inverters connected to a common load bus through an LC filter and an RL line, as depicted in Fig. 6.6. This microgrid configuration is commonly considered in power system stability studies [76, 100, 141], while as highlighted in [100], it represents a special case of a meshed microgrid. The power system components and variables are defined as follows: the inductance of the filter is denoted as L_i with its parasitic resistance being r_i, the filter capacitor is denoted as C_i, where i indicates the number of the inverter with $i \in [1, \ldots, n]$. The line inductance and resistance are represented as L_{li} and r_{li}, respectively. The inverter voltage in the natural reference frame is defined as v_{iabc}, the inverter current is given as i_{iabc}, while the capacitor voltage, load voltage, line current and load current are represented as $v_{Ciabc}, v_{abc}, i_{Liabc}$ and i_{Labc}, respectively. Each inverter can measure its inverter current i_{iabc} and its point of common coupling voltage v_{oabc}. As it is clear from Fig. 6.6, when the inverter switches are open $v_{oiabc} = v_{abc}$, while when the switches close, $v_{oiabc} = v_{Ciabc}$. Following the SRF transformation described in sec. 6.2, the dynamics of each inverter can be described in the synchronously rotating

dq reference frame using θ_i as the angle of each inverter. Since in an inverter-based microgrid each individual inverter may have its own angle and hence, its own dq frame alignment, the local dq reference frame quantities (e.g. f_{dq}) of each DER with angular frequency ω_i, can be transformed into the global DQ reference frame quantities (e.g. f_{DQ}) with angular frequency ω_{com}, through the transformation

$$f_{DQ} = \begin{bmatrix} \cos\delta_i & -\sin\delta_i \\ \sin\delta_i & \cos\delta_i \end{bmatrix} f_{dq},$$

where δ_i is the rotational angle difference between the local reference frame of each DER and the global reference frame, given by

$$\dot{\delta}_i = \omega_i - \omega_{com}. \tag{6.16}$$

To facilitate the modeling, the angular frequency of one of the inverters can be selected as the global reference frame [6]. Following the above methodology, the considered microgrid can be modeled in the synchronous reference frame, where the dynamic equations for any of the n three-phase inverters of the microgrid are obtained as

$$L_i \frac{di_{id}}{dt} = v_{id} - v_{Cid} - r_i i_{id} + \omega_i L_i i_{iq} \tag{6.17}$$

$$L_i \frac{di_{iq}}{dt} = v_{iq} - v_{Ciq} - r_i i_{iq} - \omega_i L_i i_{id}, \tag{6.18}$$

where the inverter voltage components v_{id} and v_{iq} represent the control inputs. Note that the inverter real and reactive powers P_i and Q_i can be calculated from $P_i = 1.5\left(v_{Cid} i_{id} + v_{Ciq} i_{iq}\right)$ and $Q_i = 1.5\left(v_{Ciq} i_{id} - v_{Cid} i_{iq}\right)$. For the filter capacitors and each line that connects each PCC with the common load bus, the dynamics at the global reference frame rotating with ω_{com} [6, 95], take the form

$$C_i \frac{dv_{CiD}}{dt} = i_{iD} - i_{LiD} + \omega_{com} C_i v_{CiQ} \tag{6.19}$$

$$C_i \frac{dv_{CiQ}}{dt} = i_{iQ} - i_{LiQ} - \omega_{com} C_i v_{CiD} \tag{6.20}$$

$$L_{li} \frac{di_{LiD}}{dt} = v_{CiD} - v_D - r_{li} i_{LiD} + \omega_{com} L_{li} i_{LiQ} \tag{6.21}$$

$$L_{li} \frac{di_{LiQ}}{dt} = v_{CiQ} - v_Q - r_{li} i_{LiQ} - \omega_{com} L_{li} i_{LiD}. \tag{6.22}$$

6.3.2 The Proposed Controller: Control design and current-limiting property

6.3.2.1 Control Design

In order to accomplish the desired tasks highlighted in sec. 6.1, the proposed controller is suitably designed to align the inverter current on the d axis of each inverter local dq framework, to guarantee an inherent current limitation. To this end, the inverter voltage (which is the control input) consists of two parts: i) a voltage feedforward term implemented in the abc reference frame and ii) a dynamic control part implemented in the dq reference frame. The proposed controller takes the form

$$v_{iabc} = v_{oiabc} + \overline{v}_{iabc}$$

where $\overline{v}_{iabc}$ is the dq to abc transformation of the reference voltages

$$\bar{v}_{id} = E_i - r_{vi} i_{id} - \omega_i L_i i_{iq} \tag{6.23}$$

$$\bar{v}_{iq} = -r_{vi} i_{iq} + \omega_i L_i i_{id}, \tag{6.24}$$

where E_i is a control state representing a virtual voltage, r_{vi} is a constant virtual resistance and $\omega_i L_i i_{iq}$ and $\omega_i L_i i_{id}$ are decoupling terms. The state E_i changes according to the nonlinear expressions

$$\dot{E}_i = c_i f_i(P_i, V_i) E_{qi}^2 \tag{6.25}$$

$$\dot{E_{qi}} = -\frac{c_i E_i E_{qi}}{E_{maxi}^2} f_i(P_i, V_i) - k_i \left(\frac{E_i^2}{E_{mi}^2} + E_{qi}^2 - 1 \right) E_{qi} \tag{6.26}$$

proposed in [56] while E_{qi} is an extra control state, c_i, k_i are positive constant gains and the control states initial conditions are defined as $E_{i0} = 0$, $E_{qi0} = 1$. The $P \sim V$,$Q \backsim -\omega$ droop expressions of the universal droop control scheme in [79] are considered here to provide robustness to different kinds of output impedance (i.e. resistive or capacitive). In the proposed controller, the function $f_i(P_i, V_i)$ inherits the real power droop control characteristics through the virtual voltage dynamics and takes the form

$$f_i(P_i, V_i) \;\; = \;\; E_{rms}^2 - V_i^2 - n_{pi} P_i. \tag{6.27}$$

The reactive power droop control is statically applied through the inverter local frequency ω_i with

$$\omega_i = \omega^* + m_{qi} Q_i, \tag{6.28}$$

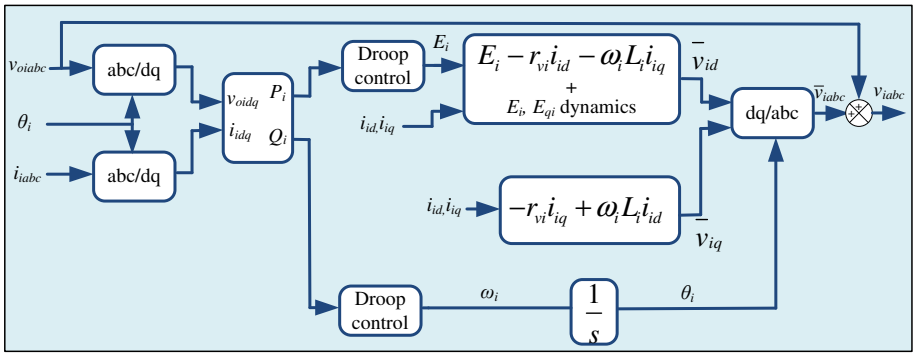

Figure 6.7: The proposed controller implementation

while n_{pi}, m_{qi} represent the real power and reactive power droop coefficients, respectively, V_i is the RMS PCC voltage and E_{rms} is the nominal RMS load voltage. The proposed controller is depicted in Fig. 6.7. The BIC structure from [56] that was adopted for the controller dynamics (6.25)-(6.26), guarantees that the controller states E_i, E_{qi} will start and remain on the ellipse $W = \left\{E_i, E_{qi} \in R : \frac{E_i^2}{E_{mi}^2} + E_{qi}^2 = 1\right\}$, based on the given initial conditions. Thus it holds that $E_i \in [-E_{mi}, E_{mi}]$, with $E_{mi} > 0$ being the absolute maximum value of the control state, which is defined by the control operator and $E_{qi} \in [0, 1]$. For more details on the boundedness of the states E_i, E_{qi}, the reader is referred to sec. 4.2. This boundedness feature is essential for the desired inverter current-limiting property of any three-phase inverter connected to a microgrid, as it will be proven through the closed-loop system analysis in the sequel.

6.3.2.2 Current-limiting property

By applying the proposed controller (6.23)-(6.24) into the inverter current dynamics (6.17)-(6.18), and considering that the switches are closed, i.e. $v_{oiabc} = v_{Ciabc}$, the closed-loop system dynamics take the form

$$L_i \frac{di_{id}}{dt} = E_i - (r_{vi} + r_i)\, i_{id} \tag{6.29}$$

$$L_i \frac{di_{iq}}{dt} = -(r_{vi} + r_i)\, i_{iq}. \tag{6.30}$$

Note that at the steady state it holds $i_{ide} = \frac{E_i}{r_{vi}+r_i}$ and $i_{iqe} = 0$, while from (6.30), it is clear that if $i_{iq}(0) = 0$, then $i_{iq}(t) = 0, \forall t \geq 0$. Now consider as Lyapunov function candidate the function

$$V = \frac{1}{2} L_i i_{id}^2 + \frac{1}{2} L_i i_{iq}^2.$$

Its time derivative takes the form

$$\dot{V} = \left(E_i i_{id} - (r_{vi} + r_i)\, i_{id}^2\right) - (r_{vi} + r_i)\, i_{iq}^2 \leq$$

$$[E_i\, 0] \begin{bmatrix} i_{id} \\ i_{iq} \end{bmatrix} - (r_{vi} + r_i)\left(i_{id}^2 + i_{iq}^2\right) \leq$$

$$-(r_{vi} + r_i)\, \|I_i\|_2^2 + \left\|\overline{E}_i\right\|_2 \|I_i\|_2\,,$$

where $I_i = [i_{id}\, i_{iq}]^T$ and $\overline{E}_i = [E_i\, 0]^T$. Furthermore taking into account the dq transformation where

$$\|I_i\|_2 = \sqrt{i_{id}^2 + i_{iq}^2} = \sqrt{2} I_{irms}$$

$$\left\|\overline{E}_i\right\|_2 = \sqrt{E_i^2} = |E_i|$$

and given that $|E_i| \leq E_{mi}$ from the BIC structure, as explained in sec. 6.3.2.1, it follows that

$$\dot{V} \leq -2\,(r_{vi} + r_i)\, I_{irms}^2 + \sqrt{2} E_{mi} I_{irms}$$

$$\dot{V} \leq -2 r_i I_{irms}^2, \forall I_{irms} \geq \frac{E_{mi}}{\sqrt{2} r_{vi}}.$$

Thus, according to the Theorem 2 in sec. 3.2, there exists a $\mathcal{KL}$ function β so that for any initial condition $I_{irms}(0)$ there is a $T \geq 0$ such that

$$I_{irms}(t) \leq \beta\left(I_{irms}(0), t\right) \quad \forall 0 \leq t \leq T$$
$$I_{irms}(t) \leq \frac{E_{mi}}{\sqrt{2} r_{vi}} \qquad \forall t \geq T,$$

proving that the solution of the RMS inverter current is uniformly ultimately bounded. Note that if initially $I_{irms}(0) \leq \frac{E_{mi}}{\sqrt{2} r_{vi}}$, then $T = 0$, i.e. it holds true that

$$I_{irms}(t) \leq \frac{E_{mi}}{\sqrt{2} r_{vi}}, \forall t \geq 0. \tag{6.31}$$

By selecting the controller parameter E_{mi} as $E_{mi} = \sqrt{2} I_{irms}^{max} r_{vi}$, (6.31) yields

$$I_{irms} \leq I_{irms}^{max}, \forall t \geq 0.$$

According to the ultimate boundedness analysis, the controller variable I_{irms}^{max} can be accordingly selected by the controller operator in order to ensure an inverter RMS current limitation at all times, even during transients. It should be highlighted that through the proposed control scheme, the maximum available current injection is achieved without requiring an adaptive limitation technique, as in conventional current-limiting approaches of dq control schemes [108, 116].

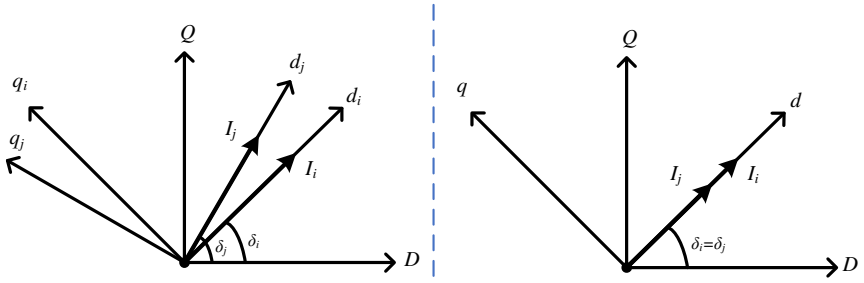

Figure 6.8: *dq* and *DQ* rotating frameworks under the proposed controller. Left: Angle transformation under generic topology. Right: Angle transformation in the case of a common load bus without lines

Remark 3: It should be noted that since the current limitation was proven independently of the microgrid structure, the inherent current-limiting capability of the proposed controller will hold under any microgrid setup (e.g. meshed microgrid) and is not limited to the common load bus structure.

6.3.3 Small-signal stability analysis of common load bus inverter-based microgrid

6.3.3.1 The case without lines between the PCC and the load bus

Although, in the previous subsection, the desired RMS current limitation was proven for each inverter, the stability analysis of the entire inverter-based microgrid is not yet guaranteed. This is a crucial problem due to the absence of a stiff grid to stabilize voltage and frequency. To investigate stability using the proposed a controller, a simple case will be initially considered where each inverter is directly connected to the load bus, i.e. without the lines shown in Fig. 6.6. This means that all inverters measure the same load voltage components in the global reference frame, i.e. by denoting any two inverters as i and j, it holds $v_{CiD} = v_{CjD} = v_D$ and $v_{CiQ} = v_{CjQ} = v_Q$. Taking into account the angle difference of each inverter from (6.16) and since it is proven in sec. 6.3.2.2 that $i_{iq} = 0$, one can rewrite the power equations as $P_i = 1.5(v_D \cos\delta_i + v_Q \sin\delta_i) i_{id}$ and $Q_i = 1.5(v_Q \cos\delta_i - v_D \sin\delta_i) i_{id}$. Since the same RMS voltage is measured by every inverter, then accurate power sharing will be achieved for both real and reactive power at the steady-state. Hence, it holds that $\frac{n_{pi}}{n_{pj}} = \frac{P_j}{P_i}$ and $\frac{m_{qi}}{m_{qj}} = \frac{Q_j}{Q_i}$, with $\frac{n_{pi}}{n_{pj}} = \frac{m_{qi}}{m_{qj}}$. Thus, at the steady-state

$$\begin{aligned} n_{pi} i_{id} \left(v_D \cos\delta_i + v_Q \sin\delta_i\right) &= n_{pj} i_{jd} \left(v_D \cos\delta_j + v_Q \sin\delta_j\right) \\ m_{qi} i_{id} \left(v_Q \cos\delta_i - v_D \sin\delta_i\right) &= m_{qj} i_{jd} \left(v_Q \cos\delta_j - v_D \sin\delta_j\right), \end{aligned}$$

which by dividing these two equations and after some mathematical manipulations results to $\left(v_D^2 + v_Q^2\right) \sin\left(\delta_j - \delta_i\right) = 0$. Under the common assumption that $\delta_i, \delta_j \in \left(-\frac{\pi}{2}, \frac{\pi}{2}\right)$ [103], it is concluded that $\delta_i = \delta_j$.

This proof shows that in the absence of lines between the PCC of each inverter and the common load bus, not only accurate power sharing is achieved without the need of hierarchical control structures but also, the rotational angle differences δ_i and δ_j are all the same and hence, by selecting the angular frequency of one inverter as the global reference frame, it holds $\delta_i = \delta_j = 0$ at the steady-state. This is also graphically explained in Fig. 6.8. However, since this represents only a special case, an analysis considering the entire microgrid with the lines, as depicted in Fig. 6.6, will be performed in the sequel.

6.3.3.2 The case with resistive-inductive lines between the PCC and the load bus

The state vector of the closed-loop system, when lines are considered between the PCC of each inverter and the common load (where δ_i, δ_j are not zero at the steady-state), as shown in Fig. 6.6, becomes $x = [i_{1d} ... i_{nd}\, E_1 ... E_n\, v_{C1D} ... v_{CnD}\, v_{C1Q} ... v_{CnQ}\, i_{L1D} ... i_{LnD}\, i_{L1Q} ... i_{LnQ}\, \delta_2 ... \delta_n\, E_{q1} ... E_{qn}\, i_{1q} ... i_{nq}]^T$, where the load is modeled as constant impedance load (RL) and the angular frequency of the first inverter is selected as the frequency of the global reference frame, i.e. $\omega_1 = \omega_{com}$. Note that when considering a constant impedance load, as commonly done in power system studies [6], the load dynamics take the form

$$\begin{aligned} L\frac{di_{LD}}{dt} &= v_D - Ri_{LD} + \omega_{com} L i_{LQ} \\ L\frac{di_{LQ}}{dt} &= v_Q - Ri_{LQ} - \omega_{com} L i_{LD}. \end{aligned}$$

For the coupling terms in the capacitor, line, load and rotational angle dynamics, the angular frequency of the global reference frame ω_{com} is selected as the steady-state microgrid frequency to simplify the analysis, as in [6, 95]. Considering an equilibrium point x_e with $x_e = [i_{1de} .. i_{nde} E_{1e} ... E_{ne} v_{C1De} .. v_{CnDe} v_{C1Qe} .. v_{CnQe} i_{L1De} .. i_{LnDe}\, i_{L1Qe} ... i_{LnQe}\, \delta_{2e} .. \delta_{ne}\, E_{q1e} ... E_{qne}\, i_{1qe} ... i_{nqe}]^T$, where $|E_{ie}| < E_{mi}$ and $E_{qie} \in (0, 1]$, the Jacobian matrix of the closed-loop system takes the form

$$A = \begin{bmatrix} A_T & 0 & A_2 \\ A_1 & -diag\left\{2k_i E_{qie}^2\right\} & A_3 \\ 0 & 0 & -diag\left\{\frac{r_{vi}+r_i}{L_i}\right\} \end{bmatrix}, \tag{6.32}$$

with

$$A_T = \begin{bmatrix} -diag\left\{\frac{r_{vi}+r_i}{L_i}\right\} & diag\left\{\frac{1}{L_i}\right\} & 0_{n\times 2n} & 0_{n\times 2n} & 0_{n\times(n-1)} \\ -diag\left\{c_i n_{pi} E_{qie}^2 \frac{3}{2}\kappa_i\right\} & 0_{n\times n} & A_{T1} & 0_{n\times 2n} & A_{T2} \\ A_{T3} & 0_{2n\times n} & \begin{bmatrix} 0_{n\times n} & diag\{\omega_{com}\} \\ -diag\{\omega_{com}\} & 0_{n\times n} \end{bmatrix} & \begin{bmatrix} -diag\left\{\frac{1}{C_i}\right\} & 0_{n\times n} \\ 0_{n\times n} & -diag\left\{\frac{1}{C_i}\right\} \end{bmatrix} & A_{T4} \\ 0_{2n\times n} & 0_{2n\times n} & A_{T5} & A_{T6} & 0_{2n\times(n-1)} \\ A_{T7} & 0_{(n-1)\times n} & A_{T8} & 0_{(n-1)\times 2n} & -diag\left\{m_{qi}\frac{3}{2} i_{ide}\lambda_i\right\} \end{bmatrix}. \tag{6.33}$$

Hence, the closed-loop system will be stable if all the eigenvalues of the matrix A_T in (6.33) have negative real parts where $\kappa_i = (v_{CiDe}\cos\delta_{ie} + v_{CiQe}\sin\delta_{ie})$, $\lambda_i = (\cos\delta_{ie} v_{CiDe} + \sin\delta_{ie} v_{CiQe})$ and the sub-matrices of the matrix A_T are given in the Appendix.

Remark 4: It should be highlighted that the dynamics of the currents i_{iq} have been decoupled under the proposed control scheme, as it is clear from (6.32). Hence, the stability investigation can be performed through a new Jacobian matrix A_T which is reduced by n states compared to conventional SRF-based droop controllers. In the conventional approaches, the voltage v_{Ciq} is regulated to zero [6] and a different timescale for the inner current controller has to be assumed in order to achieve a similar simplification in the Jacobian matrix in order to decouple the voltage dynamics. Thus, with the proposed control scheme the Jacobian matrix, and concurrently the stability analysis, is significantly simplified, without considering any timescale separation assumption.

6.3.3.3 Identifying the equilibrium point and root-locus analysis

In order to perform a root-locus analysis, first the steady-state equilibrium point of the entire microgrid needs to be identified. However, the analytic calculation of the equilibrium point is a daunting task when dealing with islanded microgrids [6, 142] and hence, many papers approximate the required equilibrium points through time-domain simulations [142, 143]. Note that an exemplary microgrid with two inverters will be considered for simplicity but a similar methodology can be followed for any number of inverters, since the microgrid modeling and the derived Jacobian matrix deal with the case of n inverters. Firstly, the first inverter's angular frequency is selected as the global reference frame. Then, only the values of I_{1rms} and ω_{com} are needed to be identified. Thus, keeping in mind that $\delta_1 = 0$, then $i_{1de} = i_{1De} = \sqrt{2} I_{1rms}$ and $i_{1qe} = i_{1Qe} = 0$. Now, the capacitor voltages of the first inverter can be calculated from the droop expressions at the steady-state as

$$\begin{aligned} v_{C1Qe} &= \frac{\omega_{com} - \omega^*}{1.5 m_{q1} i_{1De}} \\ v_{C1De} &= \sqrt{2.25 n_{p1}^2 i_{1De}^2 - v_{C1Qe}^2 + 2E_{rms}^2} - 1.5 n_{p1} i_{1De} \end{aligned}$$

and the line currents of the first inverter can be obtained from the steady-state equation of the capacitor dynamics

$$i_{LiDe} = i_{iDe} + \omega_{com} C_i v_{CiQe} \tag{6.34}$$
$$i_{LiQe} = i_{iQe} - \omega_{com} C_i v_{CiDe}. \tag{6.35}$$

Following the analysis in [100], the admittance matrix for the setup under consideration in the DQ framework takes the form

$$\begin{bmatrix} i_{L1De} \\ i_{L1Qe} \\ i_{L2De} \\ i_{L2Qe} \end{bmatrix} = \begin{bmatrix} G_{11} & -B_{11} & G_{12} & -B_{12} \\ B_{11} & G_{11} & B_{12} & G_{12} \\ G_{12} & -B_{12} & G_{22} & -B_{22} \\ B_{12} & G_{12} & B_{22} & G_{22} \end{bmatrix} \begin{bmatrix} v_{C1De} \\ v_{C1Qe} \\ v_{C2De} \\ v_{C2Qe} \end{bmatrix}.$$

Through the admittance matrix, the values of v_{C2De}, v_{C2Qe} and i_{L2De}, i_{L2Qe} can be calculated, and at the same time using the steady-state capacitor equations (6.34)-(6.35) of the second inverter, the inverter currents in the global frame can be obtained as well. Finally, since it holds that $\delta_2 = acos\left(i_{2D}/\sqrt{i_{2D}^2 + i_{2Q}^2}\right)$, the inverter currents of the second inverter in their local frame can be found as well, while it holds that $E_{ie} = i_{ide}\,(r_{vi} + r_i)$ and $E_{qie} = \sqrt{1 - (E_{ie}^2/E_{mi}^2)}$ from the BIC analysis. A specific equilibrium point for a constant RL load with $R = 12.5\,\Omega$ and $L = 20\,\text{mH}$, can now be finally obtained using the system parameters in Tab. 6.2. The state values of the equilibrium point are given in Tab. 6.3.

In Fig. 6.9, the eigenvalues of the closed-loop system, for the considered equilibrium point, are depicted for controller gains $c_1 = c_2$ ranging from 0.02 to 1.2. It is shown

Table 6.2: Power system and controllers' parameters for root-locus analysis and simulation results

Parameters	Values	Parameters	Values
Power system parameters			
L_1, L_2	2.2 mH	r_1, r_2	0.5 Ω
L_{l1}	0.028 mH	L_{l2}	0.014 mH
C_1, C_2	1 μF	r_{l1}, r_{l2}	0.04 Ω,0.02 Ω
E_{rms}	220 V	ω^*	2π50 rad/s
I_{1rms}^{max}	20 A	I_{2rms}^{max}	10 A
Proposed controller parameters			
c_1, c_2	0.9	r_{v1}, r_{v2}	20 Ω
n_{p1}, n_{p2}	0.69, 1.39	m_{q1}, m_{q2}	0.0012, 0.0024
Benchmark controller parameters			
$k_{pi}, k_{ii}, k_{pv}, k_{iv}$	4, 200, 0.3, 12	r_{v1}, r_{v2}	0.7 Ω, 1.4 Ω
n_{p1}, n_{p2}	0.0047, 0.0094	m_{q1}, m_{q2}	0.0012, 0.0024

that up to a value of $c_{critical} = 1.02$, all the eigenvalues have negative real parts and thus, according to Theorem 1 in sec. 3.1, the microgrid is stable around the considered equilibrium point using the proposed control approach. Hence, c_i can be selected according to the root-locus analysis to obtain the desired transient response and guarantee closed-loop system stability.

Table 6.3: Considered equilibrium point

Variable	Equilibrium point value
v_{C1De}, v_{C1Qe}	266.52 V,134.08 V
v_{C2De}, v_{C2Qe}	266.11 V,133.99 V
i_{1de}, i_{2de}	13.97 A,7.18 A
i_{1qe}, i_{2qe}	0 A,0 A
i_{L1De}, i_{L1Qe}	14.01 A,−0.08 A
i_{L2De}, i_{L2Qe}	7.22 A,0.01 A
ω_{com}	317.50 rad/s
δ_{2e}	0.76 ^{o}

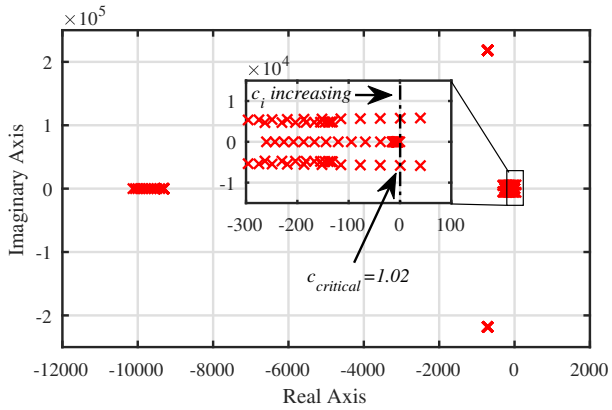

Figure 6.9: Closed-loop system eigenvalues for c_i ranging from 0.02 to 1.2

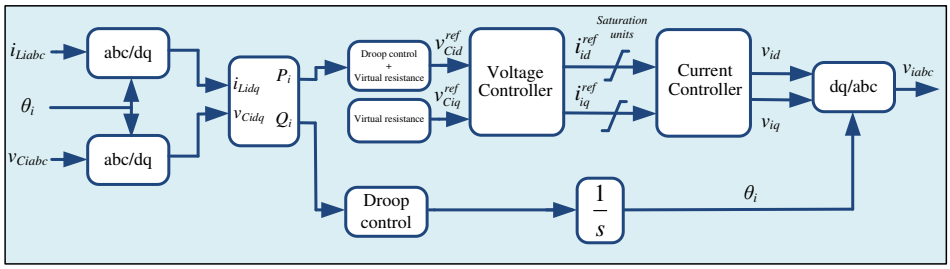

Figure 6.10: The benchmark controller implementation

6.3.4 Comparison through Simulation Results

6.3.4.1 Selection of the benchmark controller

In order to validate the properties of the proposed controller, in this section, it will be compared with a conventional virtual resistance-based droop controller [76]. The widely used *dq* framework with inner loops will be considered for the benchmark control scheme, with saturation units being applied to the reference inverter currents for current-limiting purposes, in a similar way as in [6, 52]. Finally, the selection of the droop coefficients is carried out according to the formulas in [6]. The control scheme discussed above is selected as the benchmark controller for the comparative simulations results, and is depicted in Fig. 6.10.

6.3.4.2 Simulation Results

To provide an insight into the performance of the proposed controller, compared to that of the benchmark controller, Matlab/Simulink simulation results are presented here. The exemplary case of two inverters that was used for the root-locus analysis is again considered, with Inverter #1 having twice the power rating of Inverter #2. The droop coefficients in the proposed controller can be selected as $n_{pi} = 0.19\frac{E_{rms}^2}{S_{maxi}}$ and $m_{qi} = 0.05\frac{\omega^*}{S_{maxi}}$, in order to allow a maximum of 10 % voltage deviation and 5 % frequency deviation. The power system and controller parameters are given in Tab. 6.2. For both control schemes the same scenario is examined: Initially both inverters do not feed the load since their switches are open. At 0.1 s, Inverter #1 is connected to the constant RL load which initially has the values of $R = 25\Omega$ and $L = 40$ mH, per phase. At 1.5 s, an extra load of $R = 25\,\Omega$ and $L = 40$ mH per phase is added in parallel to the initial one. At 3 s, Inverter #2 is connected and the two inverters share the common load. Finally, at 5 s, a three-phase short circuit is applied at the load bus, which is self-cleared after 150 ms.

Comparing the response of the two control schemes, depicted in Fig. 6.11, one can see that the singe inverter operation is similar for both schemes. However, at the time when Inverter #2 connects to the microgrid, the transient is much smoother using the proposed controller while using the benchmark controller, the Inverter #2 current rises close to its limit. The small difference in the power values comes from the usage of the line currents to calculate the power in the benchmark control scheme. When the three-phase short circuit is applied, using the benchmark controller, the inverter current limits are violated during the transient and reach very high values while during the steady-state, the maximum allowed current is not injected since in this certain example, i_{iq} takes very small values. For this issue to be solved, an adaptive saturation technique would be required which, however, would further complicate the control implementation. On the other hand, using the proposed controller, both RMS inverter currents are driven to their maximum values without violating this threshold value, even during the transient. The simulation results verify the superiority of the proposed controller in terms of its current-limiting capability and the smooth connection.

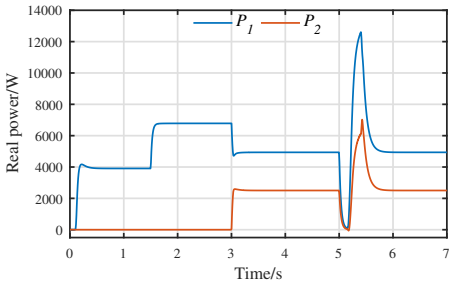

(a) Real power: Benchmark controller

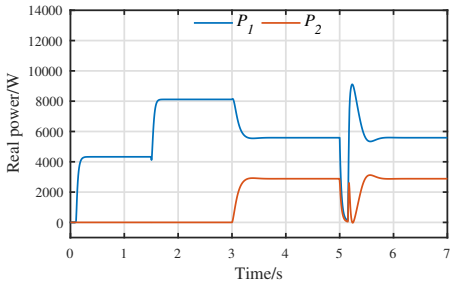

(b) Real power: Proposed controller

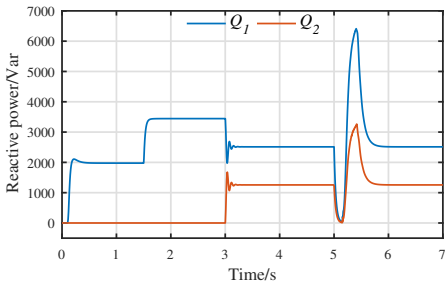

(c) Reactive power: Benchmark controller

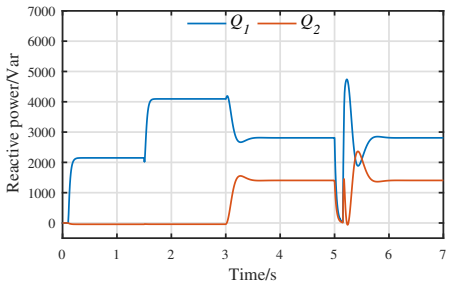

(d) Reactive power: Proposed controller

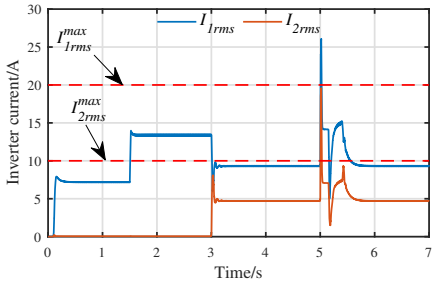

(e) Inverter currents: Benchmark controller

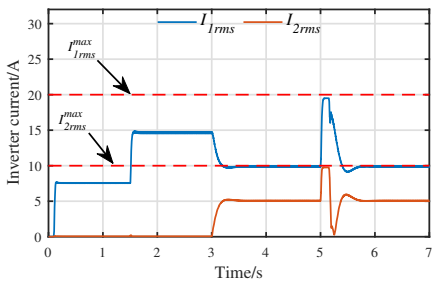

(f) Inverter currents: Proposed controller

Figure 6.11: Comparative simulation results

Table 6.4: System parameters for experimental results

Parameters	Values	Parameters	Values
L_1, L_2	3.5 mH,5.7 mH	L_{l1}, L_{l2}	4.4 mH,1 mH
r_1, r_2	0.4 Ω,0.8 Ω	r_{l1}, r_{l2}	0.9 Ω,0.4 Ω
C_1, C_2	1 μF	c_1, c_2	0.6
E_{rms}	90 V	ω^*	$2\pi 50$ rad/s
I^{max}_{1rms}	2 A	I^{max}_{2rms}	1 A
k_1,k_2	1000	r_{v1}, r_{v2}	50 Ω, 10 Ω

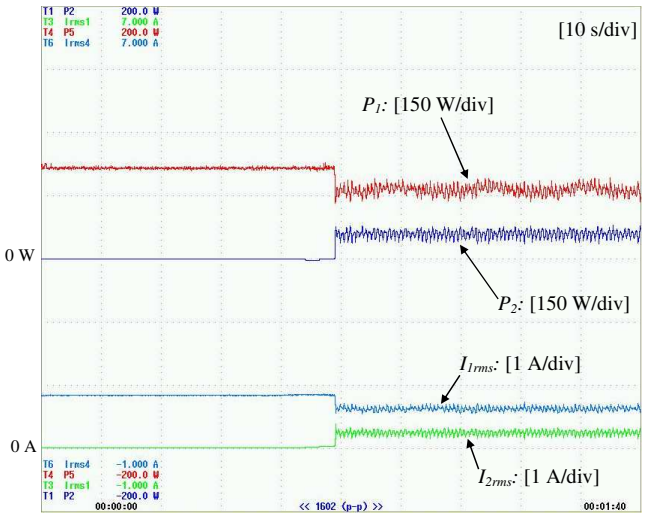

Figure 6.12: Initial operation of Inverter #1 and connection of Inverter #2

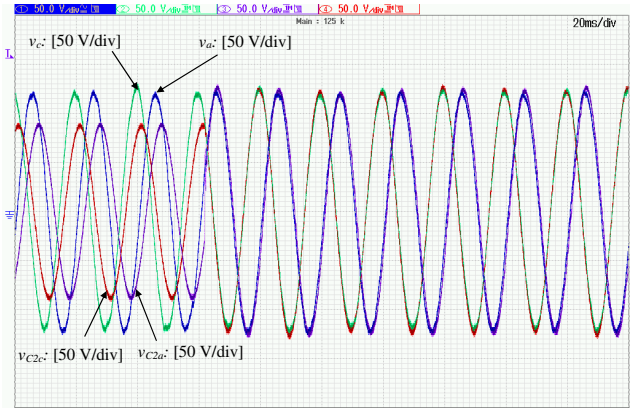

Figure 6.13: Synchronization process of Inverter #2

6.3.5 Experimental Validation

A 90 V, 50 Hz prototype lab-scale microgrid was built in order to experimentally verify the proposed controller. The microgrid consists of two three-phase inverters with ratings of 540 VA for the first inverter (Inverter #1) and 270 VA for the second inverter (Inverter #2). The controllers were digitally implemented through a Texas Instruments (TI) F28M379D control card for Inverter #1 and a dSpace 1104 control card for Inverter #2, with 15 kHz sampling frequency and 16 kHz switching frequency. Both inverters were connected to a three-phase resistive load (R) through an LC filter and a inductive-resistive line, as shown in Fig. 6.6, while the system and controller parameters are given in Tab. 6.4.

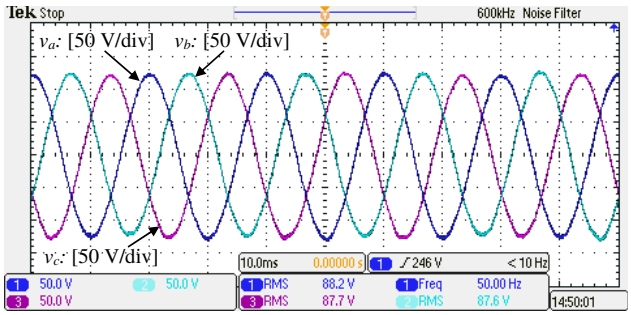

Figure 6.14: Load voltage under parallel operation of inverters

Firstly, Inverter #1 is connected to the load, which is initially $R = 100\,\Omega$. As it can bee seen in Fig. 6.12, Inverter #1 regulates its output real power to feed the load, while regulating the voltage close to its nominal value E_{rms}. I_{1rms} is also depicted in the same figure. At 44 s, Inverter #2 is switched on and at 46 s, it starts its synchronization process by feed-forwarding the PCC voltage. The synchronization process can be clearly depicted in Fig. 6.13, where at 62 ms, the voltage read at the PCC is feed-forwarded at the inverter capacitors to allow a seamless connection. When the synchronization has been completed, at 49 s in Fig. 6.12, Inverter #2 is smoothly connected to the microgrid. In Fig. 6.14 the load voltage under the parallel operation of the two inverters is shown. Since the rating of Inverter #1 is twice the rating of Inverter #2, a 2 : 1 power sharing is desired through the droop control. As it is illustrated in Fig. 6.12, the real powers and RMS currents of the two inverters are very close to the desired 2 : 1 sharing, where the small inaccuracies are expected due to the different line impedance ("line impedance effect"). Note that since the capacitors of the LC filter have small capacitance and the load is purely resistive, the reactive powers of both inverters are very close to 0 Var and thus, they are not presented here.

To verify the inherent current-limiting property (that was analytically proven in sec. 6.3.2.2), in Fig. 6.15, a load change from $R = 100\,\Omega$ to $R = 25\,\Omega$ is performed at 49 s, which represents an extreme loading demand condition. Following to the load change, I_{1rms} and I_{2rms} go very fast close to their maximum values (2 A and 1 A, respectively) without violating their limit at any time, even during the transient. Since the current provision is not enough to regulate the load voltage inside the selected 10% droop percentage, the load voltage drops to 70 V. The transient of the load voltage at the time that the load changes can be seen in Fig. 6.16, while i_{La} is also shown in the same figure. Note that the load current never exceeds the sum of the maximum RMS values of the two inverter currents, i.e. 3 A, even during the transient. This clearly demonstrates the current-limiting capability of the proposed controller for each inverter in the AC microgrid.

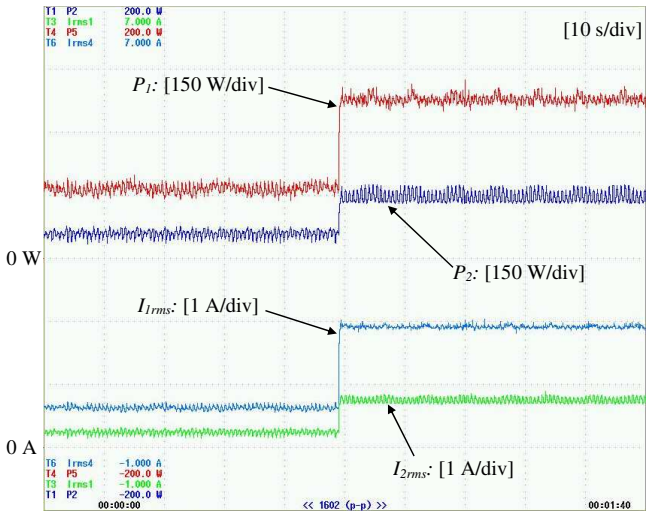

Figure 6.15: Load change and current-limiting property

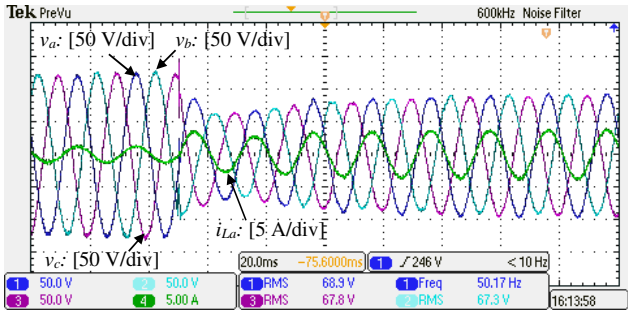

Figure 6.16: Load voltage and current transient during load change

6.4 Conclusions

In this chapter, the safe operation of inverter-based microgrids was investigated. Initially, a new current-limiting controller was proposed for three-phase inverters operating in parallel, which also guarantees the proportional power sharing between the inverters through droop control. The current-limiting property was proven through nonlinear analysis of the closed-loop system, which leads to the limitation of each inverter current under a threshold value at all times, even during transients. Moreover, the small-signal model of the closed-loop system was developed in order to evaluate the stability properties of two paralleled three-phase inverters, equipped with the proposed controller. The proposed control approach was verified through extended simulation results. In the sequel, aiming to investigate a more realistic inverter-based microgrid setup and to examine closed-loop system stability more rigorously, a new current-limiting droop controller was proposed. In contrast to conventional approaches, this novel control scheme aligns the inverter current on the d axis of the

local dq frame in order to rigorously prove the desired current limitation and the stability of the entire microgrid, under extreme load conditions. It was highlighted that the desired current limitation is ensured even during transients, while the inverter current is driven to its maximum value during faults, without requiring an online adaptation technique. Furthermore, it was shown that the proposed control scheme facilitates the stability analysis of the inverter-based microgrid. In particular, it was proven that the stability properties of the inverter-based microgrid can be investigated through a Jacobian matrix of reduced size. The proposed controller was compared to a conventional droop controller under extreme load conditions through simulation results, while its effectiveness was also verified experimentally in a lab-scale microgrid.

7 Conclusions and future work

7.1 Conclusions

The aim of this thesis was to develop advanced control schemes for grid-connected inverter-interfaced DERs and for inverter-interfaced DERs that form inverter-based microgrids. These control schemes should mathematically ensure the safe and stable operation of the system under consideration, while complying with the most recent Grid Code requirements for inverter-interfaced DERs. The development of such control schemes, that mathematically guarantee the desired response of inverter-interfaced DERs during normal and abnormal grid conditions, is expected to pave the way towards environment-friendly future smart grids.

Motivated by the bounded integral control theory, a framework was developed in this thesis for designing control systems of inverter-interfaced DERs that ensure closed-loop system asymptotic stability and protection of the inverter devices. Moreover, emphasis was given in embedding the modern Grid Code requirements in the inverter operation through the proposed control schemes. The proposed control approaches covered a wide range of inverter-interfaced DERs applications, i.e. single-phase and three-phase grid-connected inverters and three-phase inverter-based microgrids. The key novel contributions of this thesis are briefly summarized below.

In chapter 4, a new CLD controller was initially proposed for single-phase grid-connected inverters to guarantee the maximum power utilization of the inverter under grid faults and closed-loop system stability. By addressing all limitations of the original CLD, the proposed enhanced CLD version facilitates a rigorous asymptotic stability proof of any equilibrium point within a given range. The proposed controller structure was further extended to provide voltage support under grid faults. Extensive simulation and experimental results verified the proposed control approach under normal and faulty grid conditions. Then, a redesigned version of the enhanced CLD control scheme was proposed, which apart from the current-limiting and maximum power utilization properties, is further able to operate without a PLL device and at the same time to introduce a virtual inertia property to the grid-connected DER. Extensive simulation results were presented to verify this modified enhanced CLD scheme.

In chapter 5, a new droop controller was initially proposed for three-phase grid-connected inverters, introduced in a multi-loop (cascaded) control structure based on dq modeling. The proposed controller was proven to inherit a current-limiting

property for the grid-side inverter current and guarantee asymptotic stability for the closed-loop system. Moreover, the proposed design enables a simple switch between PQ-set and PQ-droop control modes to either control the injected real and reactive powers to their reference values or support the grid through droop control. Using nonlinear analysis of the closed-loop system, it was shown that the desired grid current limitation is maintained even when faults occur at the grid voltage, offering a unified control structure for both normal and abnormal grid conditions. The effectiveness of the proposed control approach was verified through extended real-time simulation results. Later on, a new control concept was proposed, which offers an inherent current limitation for three-phase grid-tied droop-controlled inverters. The proposed controller complies with the latest grid code requirements and furthermore, voltage support through maximum power injection is achieved under both balanced and unbalanced grid faults. To accomplish this, two novel outer-loop controllers are applied to both positive and negative sequences, while the boundedness of the grid current is inherently achieved without the need of saturation units, as required. A new way of dividing the maximum available current into the positive and the negative sequence current components under unbalanced grid faults was proposed, so that the positive sequence voltage is increased and the negative sequence voltage is eliminated. Finally, asymptotic stability of any equilibrium point of the closed-loop system within the bounded operating range was proven without assuming knowledge of the system parameters. The proposed control approach was verified through extensive real-time simulation results.

In chapter 6, a new current-limiting droop controller was initially proposed for three-phase inverters operating in parallel. The proportional power sharing between the parallel inverters was guaranteed through droop control, while the desired current-limiting property was proven through nonlinear analysis of the closed-loop system, which leads to the boundedness of each inverter current under a threshold value at all times, even under transients. Moreover, the stable operation of two inverters operating in parallel was guaranteed through the performed small-signal stability analysis. The proposed control approach was further validated through extended simulation results. In the sequel, in the last contribution of this thesis, aiming to investigate a more realistic inverter-based microgrid setup where lines are considered between each inverter's PCC and the load, a new droop controller was proposed to inherently guarantee RMS inverter current limitation and microgrid stability. The proposed control scheme aligns the inverter current on the d axis of the local dq frame in order to prove the desired current limitation during transients and the stability of the entire microgrid. Furthermore, it was shown that through the proposed controller, the microgrid stability properties can be investigated through a Jacobian matrix of reduced size. The proposed control approach was compared to a conventional droop control scheme under extreme load conditions through simulation results, while its effectiveness was also verified experimentally in a prototype microgrid.

7.2 Future work

Challenging and interesting topics can be investigated based on the results of this thesis. In the sequel of this section, a summary of research tasks is given to motivate future research in the area of advanced current-limiting control of inverter-interfaced DERs. These tasks include: improvements in the control design, further controller analysis, alternative approaches for the stability analysis of inverter-dominated networks and supplementary experimental verification of the proposed control schemes.

- The extension of the enhanced CLD scheme that introduces a virtual inertia property to the inverter-interfaced DER in chapter 4, has been proven to guarantee the inverter current limitation regardless of variations in the grid voltage and frequency. Nevertheless, its virtual inertia property could be further validated based on the recent frequency support requirements. Particularly, it would be of great interest to investigate the performance of this control scheme under frequency deviations, where the virtual inertia property could provide significant benefits. Furthermore, the asymptotic stability proof for the closed-loop system of the grid-connected inverter under this control scheme is still missing and should be investigated.
- In sec. 5.3, a novel control scheme was proposed to deal with the challenging task of voltage support and current limitation during unbalanced grid faults. However, in the low-voltage distribution system, unbalanced conditions may occur even during the normal operation of the power system, i.e. due to slightly unbalanced loading. Hence, it would be of interest to redesign the proposed control scheme so that its voltage support capability (in terms of decreasing the negative sequence voltage) is not limited to the case of grid faults.
- The analytical calculation of the equilibrium point of an inverter-based microgrid with an arbitrary number of inverters is indeed a daunting task. Similarly to the majority of microgrid stability analyses in the literature, the analysis of the controller regarding inverter-based microgrids in chapter 6 has utilized some information from time-domain simulations to approximate the equilibrium point. Very recently, some algorithmic approaches have been proposed for the load flow analysis of islanded microgrids, which present some similarities with the conventional load flow algorithms of large power networks. Hence, it would be of interest to approximate the desired equilibrium point through one of these algorithmic approaches instead of using time-domain simulations, in order to simplify the root-locus analysis of the microgrid stability study.
- As it was discussed in the literature review of chapter 2, the concept of deriving conditions for stability is more rigorous than the root-locus analysis, which refers to a certain microgrid application. However, due to the complexity of the dynamics of inverter-based microgrids, restricting assumptions are usually required to analytically derive conditions for stability of inverter-based microgrids. Hence, similarly to the majority of stability analyses in the lit-

erature, the stability analyses in chapter 6 employed a root-locus analysis of the small-signal model to verify the microgrid stability properties under the proposed control schemes. Even if in sec. 6.3, emphasis was given in the simplification of the Jacobian matrix, offered by the proposed controller, a great challenge arises in deriving conditions for asymptotic stability of inverter-based microgrids (that adopt the proposed controller), without considering restricting assumptions.

- Throughout this thesis, the dynamics of the DC bus of the considered inverter-interfaced DERs were ignored, i.e. a constant DC voltage was considered at the inverter input. This is a common assumption when developing control schemes for inverter-interfaced DERs. In practice though this is not always true, since the DC input power is governed by the prime mover (e.g. a photovoltaic unit or a wind turbine), which can not guarantee a constant output voltage at all times. Hence, the DC bus voltage stabilization should be considered in the inverter control system and analysis [144, 145].

- In the the proposed controllers of this thesis, the universal droop control (UDC) scheme from [79] was utilized to provide robustness against different types of output impedance. Nevertheless, it is unclear how a UDC-controlled inverter would operate in parallel to a synchronous machine [8]. Hence, an interesting task would be to redesign the advanced current-limiting droop control schemes of this thesis so that they adopt the conventional droop control relations. Indeed, even if the scenario of inverter-based microgrids raises a great challenge regarding the inverter control system design, a realistic microgrid could host synchronous machine-based DERs too. Hence, the investigation of microgrids with both inverter-interfaced and synchronous machine-based DERs would be an intriguing task.

- In the proposed schemes of chapter 4 and chapter 6, the approach of designing a power controller with inherited synchronization and voltage regulation capabilities was employed [15], while in the control schemes of chapter 5, the conventional approach with inner PI or PR voltage and current controllers was considered. Note that in this thesis, emphasis was given in designing power control schemes by employing the BIC structure to guarantee the safety and the stability of the inverter-interfaced DERs. Aiming to combine the benefits of the cascaded control structure (i.e. improved power quality) and the stability properties of the BIC structure, it would be of great interest to design a cascaded droop controller where all power, voltage and current control loops adopt the BIC structure.

- The experimental validation of the enhanced current-limiting droop controller in sec. 4.2 showed that good voltage and current quality can be achieved through the proposed control design. However, in cases where an even lower THD is required for the grid current, a redesign of the proposed controller considering a cascaded design with inner current and voltage control loops would

be required. This controller structure would further help in optimizing the design of the LCL filter, which is used to filter out the undesired harmonic components. The same remark holds for the controller regarding inverter-based microgrids in chapter 6, where adoption of inner loop controllers would improve the current and power quality.

Bibliography

[1] Q.-C. Zhong and T. Hornik, *Control of Power Inverters in Renewable Energy and Smart Grid Integration*. New York, NY, USA: Wiley-IEEE Press, 2013.

[2] Bundesverband der Energie und Wasserwirtschaft (BDEW), "Technical guideline: Generating plants connected to the medium-voltage network," 2008.

[3] Y. Xue and J. M. Guerrero, "Smart inverters for utility and industry applications," in *Proceedings of PCIM Europe 2015; International Exhibition and Conference for Power Electronics, Intelligent Motion, Renewable Energy and Energy Management*, pp. 1–8, May 2015.

[4] ENTSO-E, "Nework code for requirements for grid connection - applicable to all generators," 2013.

[5] A. Ulbig, T. S. Borsche, and G. Andersson, "Impact of low rotational inertia on power system stability and operation," *IFAC Proceedings Volumes*, vol. 47, no. 3, pp. 7290 – 7297, 2014. 19th IFAC World Congress.

[6] N. Pogaku, M. Prodanovic, and T. Green, "Modeling, Analysis and Testing of Autonomous Operation of an Inverter-Based Microgrid," *IEEE Trans. Power Electron.*, vol. 22, no. 2, pp. 613–625, 2007.

[7] National Grid, "2014 electricity ten year statement," 2014.

[8] D. E. Olivares, A. Mehrizi-Sani, A. H. Etemadi, C. A. Canizares, R. Iravani, M. Kazerani, A. H. Hajimiragha, O. Gomis-Bellmunt, M. Saeedifard, R. Palma-Behnke, G. A. Jimenez-Estevez, and N. D. Hatziargyriou, "Trends in microgrid control," *IEEE Transactions on Smart Grid*, vol. 5, pp. 1905–1919, July 2014.

[9] IEEE PES Task Force on Microgrid Stability Analysis and Modeling, "Microgrid stability definitions, analysis, and modeling," 2018.

[10] J. Fang, P. Lin, H. Li, Y. Yang, and Y. Tang, "An improved virtual inertia control for three-phase voltage source converters connected to a weak grid," *IEEE Transactions on Power Electronics*, vol. 34, no. 9, pp. 8660–8670, 2019.

[11] E. Waffenschmidt and R. S. Y. Hui, "Virtual inertia with pv inverters using dc-link capacitors," in *2016 18th European Conference on Power Electronics and Applications (EPE'16 ECCE Europe)*, pp. 1–10, 2016.

[12] M. Ashabani, F. D. Freijedo, S. Golestan, and J. M. Guerrero, "Inducverters: Pll-less converters with auto-synchronization and emulated inertia capability," *IEEE Transactions on Smart Grid*, vol. 7, pp. 1660–1674, May 2016.

[13] S. Wang, J. Hu, X. Yuan, and L. Sun, "On inertial dynamics of virtual-synchronous-controlled dfig-based wind turbines," *IEEE Transactions on Energy Conversion*, vol. 30, no. 4, pp. 1691–1702, 2015.

[14] W. Zhang, D. Remon, and P. Rodriguez, "Frequency support characteristics of grid-interactive power converters based on the synchronous power controller," *IET Renewable Power Generation*, vol. 11, no. 4, pp. 470–479, 2017.

[15] Q. C. Zhong, P. L. Nguyen, Z. Ma, and W. Sheng, "Self-synchronized synchronverters: Inverters without a dedicated synchronization unit," *IEEE Transactions on Power Electronics*, vol. 29, pp. 617–630, Feb 2014.

[16] Q.-C. Zhong and T. Hornik, *Synchronverters: Grid-Friendly Inverters That Mimic Synchronous Generators*, pp. 277–296. Wiley-IEEE Press, 2012.

[17] L. Xiong, Y. Li, Y. Zhu, P. Yang, and Z. Xu, "Coordinated control schemes of super-capacitor and kinetic energy of dfig for system frequency support," *Energies*, vol. 11, no. 1, 2018.

[18] R. Zhang, J. Fang, and Y. Tang, "Inertia emulation through supercapacitor energy storage systems," in *2019 10th International Conference on Power Electronics and ECCE Asia (ICPE 2019 - ECCE Asia)*, pp. 1365–1370, May 2019.

[19] B. K. Poolla, S. Bolognani, and F. Dorfler, "Optimal placement of virtual inertia in power grids," *IEEE Transactions on Automatic Control*, vol. 62, pp. 6209–6220, Dec 2017.

[20] T. S. Borsche, T. Liu, and D. J. Hill, "Effects of rotational inertia on power system damping and frequency transients," in *2015 54th IEEE Conference on Decision and Control (CDC)*, pp. 5940–5946, Dec 2015.

[21] I.-T. Theologitis, E. Troester, and T. Ackermann, "Aspects of a generic photovoltaic model examined under the gemran grid code for medium voltage," in *1st International Workshop on Integration of Solar Power*, 2011.

[22] Y. Yang, F. Blaabjerg, and H. Wang, "Low-voltage ride-through of single-phase transformerless photovoltaic inverters," *IEEE Transactions on Industry Applications*, vol. 50, pp. 1942–1952, May 2014.

[23] Y. Yang, F. Blaabjerg, and Z. Zou, "Benchmarking of grid fault modes in single-phase grid-connected photovoltaic systems," *IEEE Transactions on Industry Applications*, vol. 49, pp. 2167–2176, Sept 2013.

[24] J. Miret, A. Camacho, M. Castilla, L. G. de Vicuna, and J. Matas, "Control scheme with voltage support capability for distributed generation inverters under voltage sags," *IEEE Transactions on Power Electronics*, vol. 28, pp. 5252–5262, Nov 2013.

[25] A. Camacho, M. Castilla, J. Miret, R. Guzman, and A. Borrell, "Reactive power control for distributed generation power plants to comply with voltage

limits during grid faults," *IEEE Transactions on Power Electronics*, vol. 29, pp. 6224–6234, Nov 2014.

[26] B. Weise, "Impact of k-factor and active current reduction during fault-ride-through of generating units connected via voltage-sourced converters on power system stability," *IET Renewable Power Generation*, vol. 9, no. 1, pp. 25–36, 2015.

[27] H. M. Hasanien, "An adaptive control strategy for low voltage ride through capability enhancement of grid-connected photovoltaic power plants," *IEEE Transactions on Power Systems*, vol. 31, pp. 3230–3237, July 2016.

[28] J. L. Sosa, M. Castilla, J. Miret, J. Matas, and Y. A. Al-Turki, "Control strategy to maximize the power capability of pv three-phase inverters during voltage sags," *IEEE Transactions on Power Electronics*, vol. 31, pp. 3314–3323, April 2016.

[29] R. Teodorescu, M. Liserre, and P. Rodriguez, *Grid Converters for Photovoltaic and Wind Power Systems*. John Wiley & Sons, LTD, 2011.

[30] P. Piya, M. Ebrahimi, M. Karimi-Ghartemani, and S. A. Khajehoddin, "Fault ride-through capability of voltage-controlled inverters," *IEEE Transactions on Industrial Electronics*, vol. 65, pp. 7933–7943, Oct 2018.

[31] B. Popadic, B. Dumnic, D. Milicevic, V. Katic, and D. Sljivac, "Grid-connected converter control during unbalanced grid conditions based on delay signal cancellation," *International Transactions on Electrical Energy Systems*, 2018.

[32] A. Camacho, M. Castilla, J. Miret, L. G. de Vicuna, and R. Guzman, "Positive and negative sequence control strategies to maximize the voltage support in resistive-inductive grids during grid faults," *IEEE Transactions on Power Electronics*, vol. 33, pp. 5362–5373, June 2018.

[33] X. Zhao, J. M. Guerrero, M. Savaghebi, J. C. Vasquez, X. Wu, and K. Sun, "Low-voltage ride-through operation of power converters in grid-interactive microgrids by using negative-sequence droop control," *IEEE Transactions on Power Electronics*, vol. 32, pp. 3128–3142, April 2017.

[34] T. Wijnhoven, G. Deconinck, T. Neumann, and I. Erlich, "Control aspects of the dynamic negative sequence current injection of type 4 wind turbines," in *2014 IEEE PES General Meeting — Conference Exposition*, pp. 1–5, July 2014.

[35] J. Jia, G. Yang, and A. H. Nielsen, "A review on grid-connected converter control for short-circuit power provision under grid unbalanced faults," *IEEE Transactions on Power Delivery*, vol. 33, pp. 649–661, April 2018.

[36] P. Kundur, *Power System Stability and Control*. McGraw-Hill, Inc, 1994.

[37] H. Athari, M. Niroomand, and M. Ataei, "Review and classification of control systems in grid-tied inverters," *Renewable and Sustainable Energy Reviews*, vol. 72, pp. 1167 – 1176, 2017.

[38] M. Chandorkar, D. Divan, and R. Adapa, "Control of parallel connected inverters in standalone ac supply systems," *IEEE Transactions on Industry Applications*, vol. 29, pp. 136–143, Jan. 1993.

[39] J. Driesen and K. Visscher, "Virtual synchronous generators," in *2008 IEEE Power and Energy Society General Meeting - Conversion and Delivery of Electrical Energy in the 21st Century*, pp. 1–3, July 2008.

[40] H. Beck and R. Hesse, "Virtual synchronous machine," in *2007 9th International Conference on Electrical Power Quality and Utilisation*, pp. 1–6, 2007.

[41] P. Rodriguez, I. Candela, and A. Luna, "Control of pv generation systems using the synchronous power controller," in *2013 IEEE Energy Conversion Congress and Exposition*, pp. 993–998, Sep. 2013.

[42] Y. Deng, Y. Tao, G. Chen, G. Li, and X. He, "Enhanced power flow control for grid-connected droop-controlled inverters with improved stability," *IEEE Transactions on Industrial Electronics*, vol. 64, pp. 5919–5929, July 2017.

[43] G. C. Konstantopoulos, Q.-C. Zhong, and W.-L. Ming, "PLL-less nonlinear current-limiting controller for single-phase grid-tied inverters: Design, stability analysis and operation under grid faults," *IEEE Trans. Ind. Electron.*, vol. 63, pp. 5582–5591, Sept 2016.

[44] M. Karimi-Ghartemani, "Universal integrated synchronization and control for single-phase dc/ac converters," *IEEE Transactions on Power Electronics*, vol. 30, pp. 1544–1557, March 2015.

[45] Q. C. Zhong and G. C. Konstantopoulos, "Current-limiting droop control of grid-connected inverters," *IEEE Transactions on Industrial Electronics*, vol. 64, pp. 5963–5973, July 2017.

[46] N. Bottrell and T. C. Green, "Comparison of current-limiting strategies during fault ride-through of inverters to prevent latch-up and wind-up," *IEEE Trans. Power Electron.*, vol. 29, no. 7, pp. 3786–3797, 2014.

[47] A. Gkountaras, S. Dieckerhoff, and T. Sezi, "Evaluation of current limiting methods for grid forming inverters in medium voltage microgrids," in *2015 IEEE Energy Conversion Congress and Exposition (ECCE)*, pp. 1223–1230, Sep. 2015.

[48] C. T. Rim, D. Y. Hu, and G. H. Cho, "Transformers as equivalent circuits for switches: general proofs and d-q transformation-based analyses," *IEEE Transactions on Industry Applications*, vol. 26, pp. 777–785, Jul 1990.

[49] B. K. Bose, *Modern Power Electronics and AC Drives*. Prentice Hall PTR, 2002.

[50] S. Golestan, J. M. Guerrero, and G. B. Gharehpetian, "Five approaches to deal with problem of dc offset in phase-locked loop algorithms: Design considerations and performance evaluations," *IEEE Transactions on Power Electronics*, vol. 31, no. 1, pp. 648–661, 2016.

[51] L. Zaccarian and A. R. Teel, "Nonlinear scheduled anti-windup design for linear systems," *IEEE Trans. Autom. Control*, vol. 49, no. 11, pp. 2055–2061, 2004.

[52] A. D. Paquette and D. M. Divan, "Virtual impedance current limiting for inverters in microgrids with synchronous generators," *IEEE Transactions on Industry Applications*, vol. 51, pp. 1630–1638, March 2015.

[53] L. Zaccarian and A. R. Teel, "A common framework for anti-windup, bumpless transfer and reliable designs," *Automatica*, vol. 38, no. 10, pp. 1735 – 1744, 2002.

[54] Youbin Peng, D. Vrancic, and R. Hanus, "Anti-windup, bumpless, and conditioned transfer techniques for pid controllers," *IEEE Control Systems Magazine*, vol. 16, no. 4, pp. 48–57, 1996.

[55] M. A. A. Murad, B. Hayes, and F. Milano, "Application of filippov theory to the ieee standard 421.5-2016 anti-windup pi controller," in *2019 IEEE Milan PowerTech*, pp. 1–6, June 2019.

[56] G. C. Konstantopoulos, Q. . Zhong, B. Ren, and M. Krstic, "Bounded integral control of input-to-state practically stable nonlinear systems to guarantee closed-loop stability," *IEEE Transactions on Automatic Control*, vol. 61, no. 12, pp. 4196–4202, 2016.

[57] G. C. Konstantopoulos, "Enhanced bounded integral control of input-to-state stable nonlinear systems," *IFAC-PapersOnLine*, vol. 50, no. 1, pp. 8151 – 8156, 2017. 20th IFAC World Congress.

[58] N. Hatziargyriou, *Microgrids: Architecture and Control*. 2015.

[59] R. H. Lasseter and P. Paigi, "Microgrid: a conceptual solution," in *2004 IEEE 35th Annual Power Electronics Specialists Conference (IEEE Cat. No.04CH37551)*, vol. 6, pp. 4285–4290 Vol.6, June 2004.

[60] W. Issa, S. Sharkh, and M. Abusara, "Hybrid generators-based ac microgrid performance assessment in island mode," *IET Power Electronics*, vol. 12, no. 8, pp. 1973–1980, 2019.

[61] Z. Shi, J. Li, H. I. Nurdin, and J. E. Fletcher, "Comparison of virtual oscillator and droop controlled islanded three-phase microgrids," *IEEE Transactions on Energy Conversion*, vol. 34, pp. 1769–1780, Dec 2019.

[62] D. Gross, M. Colombino, J. Brouillon, and F. Dorfler, "The effect of transmission-line dynamics on grid-forming dispatchable virtual oscillator control," *IEEE Transactions on Control of Network Systems*, vol. 6, pp. 1148–1160, Sep. 2019.

[63] S. D'Arco and J. A. Suul, "Equivalence of virtual synchronous machines and frequency-droops for converter-based microgrids," *IEEE Transactions on Smart Grid*, vol. 5, pp. 394–395, Jan 2014.

[64] D. Gross and F. Dorfler, "Projected grid-forming control for current-limiting of power converters," in *2019 57th Annual Allerton Conference on Communication, Control, and Computing (Allerton)*, pp. 326–333, Sep. 2019.

[65] J. A. Martinez and J. Martin-Arnedo, "Impact of distributed generation on distribution protection and power quality," in *2009 IEEE Power Energy Society General Meeting*, pp. 1–6, July 2009.

[66] J. M. Guerrero, J. C. Vasquez, J. Matas, L. G. de Vicuna, and M. Castilla, "Hierarchical control of droop-controlled ac and dc microgrids - a general approach toward standardization," *IEEE Transactions on Industrial Electronics*, vol. 58, pp. 158–172, Jan 2011.

[67] J. Schiffer, T. Seel, J. Raisch, and T. Sezi, "Voltage stability and reactive power sharing in inverter-based microgrids with consensus-based distributed voltage control," *IEEE Transactions on Control Systems Technology*, vol. 24, pp. 96–109, Jan 2016.

[68] J. W. Simpson-Porco, Q. Shafiee, F. Dorfler, J. C. Vasquez, J. M. Guerrero, and F. Bullo, "Secondary frequency and voltage control of islanded microgrids via distributed averaging," *IEEE Transactions on Industrial Electronics*, vol. 62, pp. 7025–7038, Nov 2015.

[69] J. Guerrero, M. Chandorkar, T. Lee, and P. Loh, "Advanced control architectures for intelligent microgrids-Part I: Decentralized and hierarchical control," *IEEE Trans. Ind. Electron.*, vol. 60, pp. 1254–1262, Apr. 2013.

[70] C. N. Papadimitriou, V. A. Kleftakis, and N. D. Hatziargyriou, "Control strategy for seamless transition from islanded to interconnected operation mode of microgrids," *Journal of Modern Power Systems and Clean Energy*, vol. 5, pp. 169–176, Mar 2017.

[71] C. Jin, M. Gao, X. Lv, and M. Chen, "A seamless transfer strategy of islanded and grid-connected mode switching for microgrid based on droop control," in *2012 IEEE Energy Conversion Congress and Exposition (ECCE)*, pp. 969–973, Sep. 2012.

[72] M. Karimi-Ghartemani, S. A. Khajehoddin, P. Piya, and M. Ebrahimi, "Universal controller for three-phase inverters in a microgrid," *IEEE Journal of Emerging and Selected Topics in Power Electronics*, vol. 4, pp. 1342–1353, Dec 2016.

[73] W. Bai and K. Lee, "Distributed generation system control strategies in microgrid operation," *IFAC Proceedings Volumes*, vol. 47, no. 3, pp. 11938 – 11943, 2014. 19th IFAC World Congress.

[74] National Grid Electricity Transmission plc, "The grid code," 2016.

[75] X. Yu, C. Cecati, T. Dillon, and M. G. Simoes, "The new frontier of smart grids," *IEEE Industrial Electronics Magazine*, vol. 5, pp. 49–63, Sep. 2011.

[76] J. M. Guerrero, J. Matas, L. G. de Vicuna, M. Castilla, and J. Miret, "Decentralized control for parallel operation of distributed generation inverters using resistive output impedance," *IEEE Transactions on Industrial Electronics*, vol. 54, pp. 994–1004, April 2007.

[77] M. A. Abusara, S. M. Sharkh, and J. M. Guerrero, "Improved droop control strategy for grid-connected inverters," *Sustainable Energy, Grids and Networks*, vol. 1, pp. 10 – 19, 2015.

[78] X. Hou, Y. Sun, W. Yuan, H. Han, C. Zhong, and J. M. Guerrero, "Conventional p-omega/q-v droop control in highly resistive line of low-voltage coverter-based ac microgrid," *Energies*, vol. 9(11), no. 943, 2016.

[79] Q. C. Zhong and Y. Zeng, "Universal droop control of inverters with different types of output impedance," *IEEE Access*, vol. 4, pp. 702–712, 2016.

[80] M. S. Golsorkhi and D. D. Lu, "A decentralized control method for islanded microgrids under unbalanced conditions," *IEEE Transactions on Power Delivery*, vol. 31, pp. 1112–1121, June 2016.

[81] H. Moussa, A. Shahin, J. Martin, B. Nahid-Mobarakeh, S. Pierfederici, and N. Moubayed, "Harmonic power sharing with voltage distortion compensation of droop controlled islanded microgrids," *IEEE Transactions on Smart Grid*, vol. 9, pp. 5335–5347, Sep. 2018.

[82] M. S. Golsorkhi and D. D. C. Lu, "A control method for inverter-based islanded microgrids based on v-i droop characteristics," *IEEE Transactions on Power Delivery*, vol. 30, pp. 1196–1204, June 2015.

[83] H. Han, X. Hou, J. Yang, J. Wu, M. Su, and J. M. Guerrero, "Review of power sharing control strategies for islanding operation of ac microgrids," *IEEE Transactions on Smart Grid*, vol. 7, pp. 200–215, Jan 2016.

[84] H. Liu, Y. Yang, X. Wang, P. C. Loh, F. Blaabjerg, W. Wang, and D. Xu, "An enhanced dual droop control scheme for resilient active power sharing among paralleled two-stage converters," *IEEE Transactions on Power Electronics*, vol. 32, pp. 6091–6104, Aug 2017.

[85] A. Ketabi, S. S. Rajamand, and M. Shahidehpour, "Power sharing in parallel inverters with different types of loads," *IET Generation, Transmission Distribution*, vol. 11, no. 10, pp. 2438–2447, 2017.

[86] P. Arboleya, D. Diaz, J. Guerrero, P. Garcia, F. Briz, C. Gonzalez-Moran, and J. G. Aleixandre, "An improved control scheme based in droop characteristic for microgrid converters," *Electric Power Systems Research*, vol. 80, no. 10, pp. 1215 – 1221, 2010.

[87] Y. Kim, E. Kim, and S. Moon, "Distributed generation control method for active power sharing and self-frequency recovery in an islanded microgrid," *IEEE Transactions on Power Systems*, vol. 32, pp. 544–551, Jan 2017.

[88] M. Kosari and S. H. Hosseinian, "Decentralized reactive power sharing and frequency restoration in islanded microgrid," *IEEE Transactions on Power Systems*, vol. 32, pp. 2901–2912, July 2017.

[89] X. Sun, Y. Hao, Q. Wu, X. Guo, and B. Wang, "A multifunctional and wireless droop control for distributed energy storage units in islanded ac microgrid applications," *IEEE Transactions on Power Electronics*, vol. 32, pp. 736–751, Jan 2017.

[90] R. Majumder, B. Chaudhuri, A. Ghosh, R. Majumder, G. Ledwich, and F. Zare, "Improvement of stability and load sharing in an autonomous microgrid using supplementary droop control loop," *IEEE Transactions on Power Systems*, vol. 25, pp. 796–808, May 2010.

[91] H. Moussa, A. Shahin, J. Martin, S. Pierfederici, and N. Moubayed, "Optimal angle droop for power sharing enhancement with stability improvement in islanded microgrids," *IEEE Transactions on Smart Grid*, vol. 9, pp. 5014–5026, Sep. 2018.

[92] Y. Sun, X. Hou, J. Yang, H. Han, M. Su, and J. M. Guerrero, "New perspectives on droop control in ac microgrid," *IEEE Transactions on Industrial Electronics*, vol. 64, pp. 5741–5745, July 2017.

[93] U. Markovic, O. Stanojev, E. Vrettos, P. Aristidou, and G. Hug, "Understanding stability of low-inertia systems." Submitted for publication, 2019.

[94] E. A. A. Coelho, P. C. Cortizo, and P. F. D. Garcia, "Small-signal stability for parallel-connected inverters in stand-alone ac supply systems," *IEEE Transactions on Industry Applications*, vol. 38, pp. 533–542, March 2002.

[95] D. Baimel, J. Belikov, J. M. Guerrero, and Y. Levron, "Dynamic modeling of networks, microgrids, and renewable sources in the dq0 reference frame: A survey," *IEEE Access*, vol. 5, pp. 21323–21335, 2017.

[96] C. Spanias and I. Lestas, "A system reference frame approach for stability analysis and control of power grids," *IEEE Transactions on Power Systems*, vol. 34, pp. 1105–1115, March 2019.

[97] I. P. Nikolakakos, H. H. Zeineldin, M. S. El-Moursi, and N. D. Hatziargyriou, "Stability evaluation of interconnected multi-inverter microgrids through critical clusters," *IEEE Transactions on Power Systems*, vol. 31, pp. 3060–3072, July 2016.

[98] K. Yu, Q. Ai, S. Wang, J. Ni, and T. Lv, "Analysis and optimization of droop controller for microgrid system based on small-signal dynamic model," *IEEE Transactions on Smart Grid*, vol. 7, pp. 695–705, March 2016.

[99] H. Lin, C. Jia, J. M. Guerrero, and J. C. Vasquez, "Angle stability analysis for voltage-controlled converters," *IEEE Transactions on Industrial Electronics*, vol. 64, pp. 6265–6275, Aug 2017.

[100] E. A. A. Coelho, D. Wu, J. M. Guerrero, J. C. Vasquez, T. Dragicevic, C. Stefanovic, and P. Popovski, "Small-signal analysis of the microgrid secondary control considering a communication time delay," *IEEE Transactions on Industrial Electronics*, vol. 63, pp. 6257–6269, Oct 2016.

[101] W. R. Issa, M. A. Abusara, and S. M. Sharkh, "Impedance interaction between islanded parallel voltage source inverters and the distribution network," in *7th IET International Conference on Power Electronics, Machines and Drives (PEMD 2014)*, pp. 1–6, 2014.

[102] J. W. Simpson-Porco, F. Dörfler, and F. Bullo, "Synchronization and power sharing for droop-controlled inverters in islanded microgrids," *Automatica*, vol. 49, no. 9, pp. 2603–2611, 2013.

[103] J. Schiffer, R. Ortega, A. Astolfi, J. Raisch, and T. Sezi, "Conditions for stability of droop-controlled inverter-based microgrids," *Automatica*, vol. 50, no. 10, pp. 2457 – 2469, 2014.

[104] A. Fahima, R. Ofir, Y. Levron, and J. Belikov, "Minimal energy storage required for stability of low inertia distributed sources," in *2018 IEEE International Energy Conference (ENERGYCON)*, pp. 1–5, June 2018.

[105] J. Schiffer, A. Anta, T. D. Trung, J. Raisch, and T. Sezi, "On power sharing and stability in autonomous inverter-based microgrids," in *2012 IEEE 51st IEEE Conference on Decision and Control (CDC)*, pp. 1105–1110, Dec 2012.

[106] J. Schiffer, D. Goldin, J. Raisch, and T. Sezi, "Synchronization of droop-controlled microgrids with distributed rotational and electronic generation," in *52nd IEEE Conference on Decision and Control*, pp. 2334–2339, 2013.

[107] W. Du and R. H. Lasseter, "Overload mitigation control of droop-controlled grid-forming sources in a microgrid," in *2017 IEEE Power Energy Society General Meeting*, pp. 1–5, July 2017.

[108] L. Huang, H. Xin, Z. Wang, K. Wu, H. Wang, J. Hu, and C. Lu, "A virtual synchronous control for voltage-source converters utilizing dynamics of dc-link capacitor to realize self-synchronization," *IEEE Journal of Emerging and Selected Topics in Power Electronics*, vol. 5, pp. 1565–1577, Dec 2017.

[109] A. Camacho, M. Castilla, J. Miret, A. Borrell, and L. G. de Vicuna, "Active and reactive power strategies with peak current limitation for distributed generation inverters during unbalanced grid faults," *IEEE Transactions on Industrial Electronics*, vol. 62, pp. 1515–1525, March 2015.

[110] A. Gkountaras, *Modeling Techniques and Control Strategies for Inverter Dominated Microgrids*. Universitatsverlag der TU Berlin, 2017.

[111] N. A. Awadhi and M. S. E. Moursi, "A novel centralized pv power plant controller for reducing the voltage unbalance factor at transmission level interconnection," *IEEE Transactions on Energy Conversion*, vol. 32, pp. 233–243, March 2017.

[112] X. Lu, J. Wang, J. M. Guerrero, and D. Zhao, "Virtual-impedance-based fault current limiters for inverter dominated ac microgrids," *IEEE Transactions on Smart Grid*, vol. 9, pp. 1599–1612, May 2018.

[113] A. Camacho, M. Castilla, J. Miret, L. G. de Vicuna, and G. L. M. Andres, "Control strategy for distribution generation inverters to maximize the voltage support in the lowest phase during voltage sags," *IEEE Transactions on Industrial Electronics*, vol. 65, pp. 2346–2355, March 2018.

[114] F. Nejabatkhah, Y. W. Li, and B. Wu, "Control strategies of three-phase distributed generation inverters for grid unbalanced voltage compensation," *IEEE Transactions on Power Electronics*, vol. 31, pp. 5228–5241, July 2016.

[115] T. Neumann, T. Wijnhoven, G. Deconinck, and I. Erlich, "Enhanced dynamic voltage control of type 4 wind turbines during unbalanced grid faults," *IEEE Transactions on Energy Conversion*, vol. 30, pp. 1650–1659, Dec 2015.

[116] S. Acharya, M. S. El-Moursi, A. Al-Hinai, A. S. Al-Sumaiti, and H. H. Zeineldin, "A control strategy for voltage unbalance mitigation in an islanded microgrid considering demand side management capability," *IEEE Transactions on Smart Grid*, vol. 10, no. 3, pp. 2558–2568, 2019.

[117] A. Moawwad, M. S. E. Moursi, and W. Xiao, "A novel transient control strategy for vsc-hvdc connecting offshore wind power plant," *IEEE Transactions on Sustainable Energy*, vol. 5, pp. 1056–1069, Oct 2014.

[118] "Short-circuit currents: Information on short-circuit currents of sma pv inverters (technical information)," tech. rep., SMA, 2016.

[119] H. K. Khalil, *Nonlinear Systems*. Prentice Hall, 1996.

[120] J.-J. E. Slotine and W. LI, *Applied nonlinear control*. 1991.

[121] J. Schiffer, D. Zonetti, R. Ortega, A. M. Stankovic, T. Sezi, and J. Raisch, "A survey on modeling of microgrids - from fundamental physics to phasors and voltage sources," *Automatica*, vol. 74, pp. 135 – 150, 2016.

[122] Q.-C. Zhong and D. Boroyevich, "A droop controller is intrinsically a phase-locked loop," in *Proc. of the 39th Annual Conference of the IEEE Industrial Electronics Society, IECON 2013*, (Vienna, Austria), pp. 5916–5921, Nov. 2013.

[123] J. D. Glover, M. S. Sarma, and T. J. Overbye, *Power System Analysis and Design*. Cengage Learning, 2012.

[124] "Wind integration: International experience, wp2: Review of grid codes," tech. rep., Australian Energy Market Operator, 2011.

[125] S. Arcuri, M. Liserre, D. Ricchiuto, T. Kerekes, and F. Blaabjerg, "Stability analysis of grid inverter lcl-filter resonance in wind or photovoltaic parks," in *IECON 2011 - 37th Annual Conference of the IEEE Industrial Electronics Society*, pp. 2499–2504, Nov 2011.

[126] Q. C. Zhong and G. C. Konstantopoulos, "Current-limiting three-phase rectifiers," *IEEE Transactions on Industrial Electronics*, vol. 65, pp. 957–967, Feb 2018.

[127] Y. Ojo and J. Schiffer, "Towards a time-domain modeling framework for small-signal analysis of unbalanced microgrids," in *2017 IEEE Manchester PowerTech*, pp. 1–6, June 2017.

[128] Y. Zhou, P. Bauer, J. A. Ferreira, and J. Pierik, "Operation of grid-connected dfig under unbalanced grid voltage condition," *IEEE Transactions on Energy Conversion*, vol. 24, pp. 240–246, March 2009.

[129] A. El-Naggar and I. Erlich, "Control approach of three-phase grid connected pv inverters for voltage unbalance mitigation in low-voltage distribution grids," *IET Renewable Power Generation*, vol. 10, no. 10, pp. 1577–1586, 2016.

[130] Y. Sun, P. Li, S. Li, and L. Zhang, "Contribution determination for multiple unbalanced sources at the point of common coupling," *Energies*, vol. 10, no. 2, 2017.

[131] R. Tonkoski, L. A. C. Lopes, and T. H. M. El-Fouly, "Coordinated active power curtailment of grid connected pv inverters for overvoltage prevention," *IEEE Transactions on Sustainable Energy*, vol. 2, pp. 139–147, April 2011.

[132] S. Mishra and Y. Mishra, "Decoupled controller for single-phase grid connected rooftop pv systems to improve voltage profile in residential distribution systems," *IET Renewable Power Generation*, vol. 11, no. 2, pp. 370–377, 2017.

[133] M. Garnica, L. Garcia de Vicuna, J. Miret, A. Camacho, and R. Guzman, "Voltage support experimental analysis of a low-voltage ride-through strategy applied to grid-connected distributed inverters," *Energies*, vol. 11, p. 1949, Jul 2018.

[134] M. M. Shabestary and Y. A. I. Mohamed, "Advanced voltage support and active power flow control in grid-connected converters under unbalanced conditions," *IEEE Transactions on Power Electronics*, vol. 33, pp. 1855–1864, Feb 2018.

[135] "Grid code, high and extra high voltage," tech. rep., EON Netz, German TSO, 2016.

[136] A. Camacho, M. Castilla, F. Canziani, C. Moreira, P. Coelho, M. Gomes, and P. Mercado, "Performance comparison of grid-faulty control schemes for inverter-based industrial microgrids," *Energies*, vol. 10, p. 2096, 2017.

[137] D. P. Kothari and I. J. Nagrath, *Modern Power System Analysis*. Tata McGraw Hill Education Private Limited, 2003.

[138] I. Erlich, T. Neumann, F. Shewarega, P. Schegner, and J. Meyer, "Wind turbine negative sequence current control and its effect on power system protection," in *2013 IEEE Power Energy Society General Meeting*, pp. 1–5, July 2013.

[139] B. Li, J. Jia, and S. Xue, "Study on the current-limiting-capable control strategy for grid-connected three-phase four-leg inverter in low-voltage network," *Energies*, vol. 9, no. 9, 2016.

[140] S. Dedeoglu and G. C. Konstantopoulos, "Three-phase grid-connected inverters equipped with nonlinear current- limiting control," in *2018 UKACC 12th International Conference on Control (CONTROL)*, pp. 38–43, Sept 2018.

[141] L. He, Z. Shuai, X. Zhang, X. Liu, Z. Li, and Z. J. Shen, "Transient characteristics of synchronverters subjected to asymmetric faults," *IEEE Transactions on Power Delivery*, vol. 34, pp. 1171–1183, June 2019.

[142] X. Wu, C. Shen, M. Zhao, Z. Wang, and X. Huang, "Small signal security region of droop coefficients in autonomous microgrids," in *2014 IEEE PES General Meeting — Conference Exposition*, pp. 1–5, July 2014.

[143] D. Dheer, S. Doolla, S. Bandyopadhyay, and J. M. Guerrero, "Effect of placement of droop based generators in distribution network on small signal stability margin and network loss," *International Journal of Electrical Power & Energy Systems*, vol. 88, pp. 108 – 118, 2017.

[144] W. Issa, M. Abusara, S. Sharkh, and T. Mallick, "A small signal model of an inverter-based microgrid including dc link voltages," in *2015 17th European Conference on Power Electronics and Applications (EPE'15 ECCE-Europe)*, pp. 1–10, 2015.

[145] W. R. Issa, A. H. E. Khateb, M. A. Abusara, and T. K. Mallick, "Control strategy for uninterrupted microgrid mode transfer during unintentional islanding scenarios," *IEEE Transactions on Industrial Electronics*, vol. 65, no. 6, pp. 4831–4839, 2018.

[146] M. Kabalan, P. Singh, and D. Niebur, "Nonlinear lyapunov stability analysis of seven models of a dc/ac droop controlled inverter connected to an infinite bus," *IEEE Transactions on Smart Grid*, vol. 10, pp. 772–781, Jan 2019.

[147] I. Subotic, D. Gross, M. Colombino, and F. Dorfler, "A lyapunov framework for nested dynamical systems on multiple time scales with application to converter-based power systems," *IEEE Transactions on Automatic Control*, 2019. Submitted. Available at https://arxiv.org/abs/1911.08945.

Appendix

1. Analytical calculation of the maximum positive sequence RMS current

Initially consider the power system modeling of sec. 5.3. Furthermore, the voltage difference between the positive sequence RMS voltage at the capacitor V_C^+ and the PCC RMS voltage V^+, is denoted as $\Delta\bar{V} = V_C^+ - V^+$, while as P_C and Q_C, the real and reactive powers measured at the capacitor node are defined, respectively. By rewriting (5.45) for $\Delta\bar{V}$ it holds,

$$\Delta\bar{V} = \frac{P_C^+ r_g + Q_C^+ x_{Lg}}{3V_C^+}.$$

Nevertheless, from the analysis in [137], $\Delta\bar{V}$ can be also described from

$$\Delta\bar{V} = \frac{P^+ r_g + Q^+ x_{Lg}}{3V^+},$$

where P^+ and Q^+ are the positive sequence real and reactive powers measured at the PCC. Now, the aim is to calculate the required positive sequence RMS grid current so that during unbalanced voltage drops, it holds $V_C^+ \geq 0.9E_{rms}^+$ or $V_C^+ - V^+ \geq 0.9E_{rms}^+ - V^+$ or $\Delta\bar{V} \geq 0.9E_{rms}^+ - V^+$.

By defining the p.u. voltage drop as ρ, where $\rho = 1 - \frac{V^+}{E_{rms}^+}$, and considering that real and reactive powers are regulated to their reference values obtained from the FRT scheme in (5.46), i.e. $Q_{set}^+ = \rho k S_{max}^+$ and $P_{set}^+ = \sqrt{S_{max}^{+2} - Q_{set}^{+2}}$, it is concluded that

$$\Delta\bar{V} \geq 0.9E_{rms}^+ - V^+ \Longrightarrow \frac{S_{max}^+ \left(\sqrt{1-\rho^2k^2}r_g + \rho k x_{Lg}\right)}{3V^+} \geq 0.9E_{rms}^+ - V^+$$

$$\Longrightarrow I_{grms}^+ \geq \frac{0.9E_{rms}^+ - V^+}{\sqrt{1-\rho^2k^2}r_g + \rho k x_{Lg}} \Longrightarrow I_{grms}^+ \geq \frac{E_{rms}^+ \left(0.9 - (1-\rho)\right)}{\sqrt{1-\rho^2k^2}r_g + \rho k x_{Lg}}.$$

Thus, we can select the positive sequence maximum RMS grid current as

$$I_{grms}^{max+} = \frac{E_{rms}^{+}\left(0.9 - (1-\rho)\right)}{\sqrt{1-\rho^2 k^2} r_g + \rho k x_{Lg}}.$$

2. Different time scales approach to assume constant PCC voltage

Recently, the investigation of the closed-loop system stability of inverter-dominated power networks has been approached through the singular perturbation method [119]. Through this method, the system under consideration is separated into subsystems that operate in different time scales, aiming to simplify the closed-loop system stability analysis. This concept is analytically explained in [146, 147].

As in the case of the control scheme proposed in sec. 5.3, let us consider an inverter connected to a stiff grid through an LCL_g filter and an L_l, r_l line (feeder). Moreover, consider that a PCC voltage feed-forward and a decoupling of the cross-coupling terms are applied through the outer loop controller, while that fast inner voltage and current control loops allow us to ignore the LC system of the filter (again as in sec. 5.3). Thus, the closed-loop system can be described from the dynamic equations

$$\begin{aligned}
L_g\frac{di_{gd}}{dt} &= E_d - (r_v + r_g)\, i_{gd} \\
L_g\frac{di_{gq}}{dt} &= E_q - (r_v + r_g)\, i_{gq} \\
L_l\frac{di_{gd}}{dt} &= v_d - v_{gd} - r_l i_{gd} - \omega_g L_l i_{gq} \\
L_l\frac{di_{gq}}{dt} &= v_q - v_{gq} - r_l i_{gq} + \omega_g L_l i_{gd},
\end{aligned}$$

where E_d and E_q are control states, r_g is the parasitic resistance of the grid-side filter inductance and r_v is a constant virtual resistance, similarly to the system (5.43)-(5.44). To assume a time scale separation, we need to identify a unitless variable ϵ to transform our original system to the form of the singular perturbation method [119]. Hence, the following transformations are considered:

$$\begin{aligned}
\begin{bmatrix} i_{gd} \\ i_{gq} \end{bmatrix} &= Ix \\
\begin{bmatrix} E_d \\ E_q \end{bmatrix} &= Eu \\
\begin{bmatrix} v_d \\ v_q \end{bmatrix} - \begin{bmatrix} v_{gd} \\ v_{gq} \end{bmatrix} &= \bar{V}\,(z-d) \\
t = T\tau \Longrightarrow \frac{dx}{dt} &= \frac{1}{T}\frac{dx}{d\tau},
\end{aligned}$$

where I, T, E and $\bar{V}$ are current, time and voltage variables respectively and

$$x = \begin{bmatrix} x_d \\ x_q \end{bmatrix}, u = \begin{bmatrix} u_d \\ u_q \end{bmatrix}, (z-d) = \begin{bmatrix} z_d - d_d \\ z_q - d_q \end{bmatrix},$$

with $x_d, x_q, z_d, z_q, d_d, d_q, u_d, u_q, \tau$ being unitless scalars. Hence, the initial system can be rewritten as

$$\begin{aligned}
\frac{L_g I}{T}\frac{dx_d}{d\tau} &= Eu_d - (r_v + r_g)\, I x_d \\
\frac{L_g I}{T}\frac{dx_q}{d\tau} &= Eu_q - (r_v + r_g)\, I x_q \\
\frac{L_l I}{T}\frac{dx_d}{d\tau} &= \bar{V}\,(z_d - d_d) - r_l I x_d - \omega_g L_l I x_q \\
\frac{L_l I}{T}\frac{dx_q}{d\tau} &= \bar{V}\,(z_q - d_q) - r_l I x_q + \omega_g L_l I x_d.
\end{aligned}$$

In vector form, the system becomes

$$\begin{aligned}
\frac{L_g I}{T}\frac{dx}{d\tau} &= Eu - (r_v + r_g)\, I x \\
\frac{dx}{d\tau} &= \frac{T\bar{V}\,(z-d)}{L_l I} - \begin{bmatrix} \frac{r_l T}{L_l} & \frac{\omega L_l T}{L_l} \\ -\frac{\omega L_l T}{L_l} & \frac{r_l T}{L_l} \end{bmatrix} x,
\end{aligned}$$

or equivalently

$$\begin{aligned}
\frac{L_g}{T(r_v + r_g)}\frac{dx}{d\tau} &= \frac{Eu}{(r_v + r_g)\, I} - x \\
\frac{dx}{d\tau} &= \frac{T\bar{V}\,(z-d)}{L_l I} - \begin{bmatrix} \frac{r_l T}{L_l} & \omega T \\ -\omega T & \frac{r_l T}{L_l} \end{bmatrix} x.
\end{aligned}$$

Now, in order to bring both systems in the general form $\dot{x} = Ax + Bu$, we can define $T = \frac{L_l I}{\bar{V}}$, $\bar{V} = \omega L_l I$ and $E = (r_v + r_g)\, I$. Hence, the initial system can be finally described from

$$\epsilon\frac{dx}{d\tau} = u - x \tag{7.1}$$

$$\frac{dx}{d\tau} = (z-d) - \begin{bmatrix} \frac{r_l T}{L_l} & 1 \\ -1 & \frac{r_l T}{L_l} \end{bmatrix} x, \tag{7.2}$$

where $\epsilon = \frac{L_g}{T(r_v + r_g)}$. Thus, we can now define the unitless variable ϵ, which describes the time scale separation of systems (7.1) and (7.2) as

$$\epsilon = \frac{L_g}{T\,(r_v + r_g)} = \frac{\omega L_g}{r_v + r_g}.$$

Note that through the appropriate selection of the controller parameter r_v, ϵ takes very small values. Hence, the two dynamic systems (7.1) and (7.2) operate in a different time scale and can be studied according to the singular perturbation theory [119]. In particular, it is proven that the grid-side filter inductance dynamics operate

in a faster time scale than the line (feeder) dynamics and thus, the PCC voltage (which can be calculated from the stiff grid voltage and the line currents) can be considered as constant for the controller analysis [147].

3. Sub-matrices of the inverter-based microgrid Jacobian matrix in sec. 6.3.3

$$A_{T1} = \begin{bmatrix} c_1 E_{q1e}^2 \beta_1 & \cdots & 0 & -c_1 E_{q1e}^2 \gamma_1 & \cdots & 0 \\ \vdots & \ddots & \vdots & \vdots & \ddots & \vdots \\ 0 & \cdots & c_n E_{qne}^2 \beta_n & 0 & \cdots & -c_n E_{qne}^2 \gamma_n \end{bmatrix}$$

$\beta_i = \left(-\frac{3}{2} n_{pi} i_{ide} \cos\delta_{ie} - v_{CiDe}\right)$, $\gamma_i = \left(\frac{3}{2} n_{pi} i_{ide} \sin\delta_{ie} + v_{CiQe}\right)$.

$$A_{T2} = \begin{bmatrix} 0 & \cdots & 0 \\ c_2 n_{p2} E_{q2e}^2 \frac{3}{2} i_{2de} \eta_2 & \cdots & 0 \\ \vdots & \ddots & \vdots \\ 0 & \cdots & c_n n_{pn} E_{qne}^2 \frac{3}{2} i_{nde} \eta_n \end{bmatrix}$$

$\eta_i = (-\cos\delta_{ie} v_{CiQe} + \sin\delta_{ie} v_{CiDe})$.

$$A_{T3} = \begin{bmatrix} \frac{\cos\delta_{1e}}{C_1} & \cdots & 0 \\ \vdots & \ddots & \vdots \\ 0 & \cdots & \frac{\cos\delta_{ne}}{C_n} \\ \frac{\sin\delta_{1e}}{C_1} & \cdots & 0 \\ \vdots & \ddots & \vdots \\ 0 & \cdots & \frac{\sin\delta_{ne}}{C_n} \end{bmatrix} . A_{T4} = \begin{bmatrix} 0 & \cdots & 0 \\ -\frac{\sin\delta_{2e} i_{2de}}{C_2} & \cdots & 0 \\ \vdots & \ddots & \vdots \\ 0 & \cdots & -\frac{\sin\delta_{ne} i_{nde}}{C_n} \\ 0 & \cdots & 0 \\ \frac{\cos\delta_{2e} i_{2de}}{C_2} & \cdots & 0 \\ \vdots & \ddots & \vdots \\ 0 & \cdots & \frac{\cos\delta_{ne} i_{nde}}{C_n} \end{bmatrix}.$$

$$A_{T5} = \begin{bmatrix} \varrho_1 & \xi_{12} & \cdots & \xi_{1n} & 0 & 0 & \cdots & 0 \\ \xi_{21} & \varrho_2 & \cdots & \xi_{2n} & 0 & 0 & \cdots & 0 \\ \vdots & \vdots & \ddots & \vdots & \vdots & \vdots & \ddots & \vdots \\ \xi_{n1} & \xi_{n2} & \cdots & \varrho_n & 0 & 0 & \cdots & 0 \\ 0 & 0 & \cdots & 0 & \varrho_1 & \xi_{12} & \cdots & \xi_{1n} \\ 0 & 0 & \cdots & 0 & \xi_{21} & \varrho_2 & \cdots & \xi_{2n} \\ \vdots & \vdots & \ddots & \vdots & \vdots & \vdots & \ddots & \vdots \\ 0 & 0 & \cdots & 0 & \xi_{n1} & \xi_{n2} & \cdots\cdots & \varrho_n \end{bmatrix},$$

$\varrho_i = L_{li}^{-1} - \frac{L_{li}^{-2}}{L_{sum}^{-1}}$, $\xi_{ij} = -\frac{L_{li}^{-1} L_{lj}^{-1}}{L_{sum}^{-1}}$, $L_{sum}^{-1} = L^{-1} + \sum_{i=1}^{n} L_{li}^{-1}$.

$$A_{T6} = \begin{bmatrix} \varphi_1 & \psi_{12} & \cdots & \psi_{1n} & \omega_{com} & 0 & \cdots & 0 \\ \psi_{21} & \varphi_2 & \cdots & \psi_{2n} & 0 & \omega_{com} & \cdots & 0 \\ \vdots & \vdots & \ddots & \vdots & \vdots & \vdots & \ddots & \vdots \\ \psi_{n1} & \psi_{n2} & \cdots & \varphi_n & 0 & 0 & \cdots & \omega_{com} \\ -\omega_{com} & 0 & \cdots & 0 & \varphi_1 & \psi_{12} & \cdots & \psi_{1n} \\ 0 & -\omega_{com} & \cdots & 0 & \psi_{21} & \varphi_2 & \cdots & \psi_{2n} \\ \vdots & \vdots & \ddots & \vdots & \vdots & \vdots & \ddots & \vdots \\ 0 & 0 & \cdots & -\omega_{com} & \psi_{n1} & \psi_{n2} & \cdots & \varphi_n \end{bmatrix}$$

$\varphi_i = -L_{li}^{-1}\frac{L^{-1}R - L_{li}^{-1}r_{li}}{L_{sum}^{-1}} - L_{li}^{-1}r_{li}$, $\psi_{ij} = -L_{li}^{-1}\frac{RL^{-1} - L_{lj}^{-1}r_{lj}}{L_{sum}^{-1}}$.

$$A_{T7} = \begin{bmatrix} 0 & -m_{q2}\frac{3}{2}\eta_2 & \cdots & 0 \\ \vdots & \vdots & \ddots & \vdots \\ 0 & 0 & \cdots & -m_{qn}\frac{3}{2}\eta_n \end{bmatrix}.$$

$$A_{T8} = \begin{bmatrix} 0 & -\frac{3}{2}\zeta_2 & \cdots & 0 & 0 & \frac{3}{2}\sigma_2 & \cdots & 0 \\ \vdots & \vdots & \ddots & \vdots & \vdots & \vdots & \ddots & \vdots \\ 0 & 0 & \cdots & -\frac{3}{2}\zeta_n & 0 & 0 & \cdots & \frac{3}{2}\sigma_n \end{bmatrix},$$

$\zeta_i = m_{qi}i_{ide}\sin\delta_{ie}$, $\sigma_i = m_{qi}i_{ide}\cos\delta_{ie}$.

List of publications

In this section, the list of publications associated with this thesis, is given. The publications are separated into journal papers, conference papers, presentations and papers under review circulation.

Publications in Peer-Reviewed Journals:

1. A. Paspatis and G. Konstantopoulos, "Voltage support under grid faults with inherent current limitation for three-phase droop-controlled inverters," Energies, vol. 12, no. 6, p. 997, Mar 2019.
2. A. Paspatis, G. Konstantopoulos and J.M. Guerrero, "Enhanced Current-Limiting Droop Controller for Grid-Connected Inverters to Guarantee Stability and Maximize Power Injection under Grid Faults," IEEE Transactions on Control Systems Technology, 2019, In press.

Publications in Peer-Reviewed Conferences with Proceedings:

1. A. Paspatis, G. Konstantopoulos, M. Mayfield and V.C. Nikolaidis, "Current-Limiting Droop Controller with Fault-Ride-Through Capability for Grid-Tied Inverters," IEEE International Conference on Innovative Smart Grid Technologies Europe 2017 (ISGT Europe), 26-29 September, Torino, Italy, 2017.
2. A. Paspatis and G. Konstantopoulos, "Current-limiting Droop Control with Virtual Inertia and Self-Synchronization Properties," 43rd IEEE Industrial Electronics Society Conference (IECON), 29 October- 1 November, Beijing, China, 2017.
3. A. Paspatis and G. Konstantopoulos, "SRF-Based Current-limiting Droop Controller for Three-Phase Grid-Tied Inverters," 44th IEEE Industrial Electronics Society Conference (IECON), Washington, USA, 2018.
4. A. Paspatis and G. Konstantopoulos, "Three-Phase Current-Limiting Droop Controlled Inverters Operating in Parallel," 13th IEEE PES Powertech Conference 2019, Milano, Italy, 2019.
5. Z. Masud, A. Paspatis and G. Konstantopoulos, "Current-Limiting Droop Controller for Single-Phase Inverters Operating in Island Mode," 45th IEEE Industrial Electronics Society Conference (IECON), Lisbon, Portugal, 2019.

Presentations in Peer-Reviewed Symposia without Proceedings:

1. A. Paspatis and G. Konstantopoulos, "Advanced Current-Limiting Droop Control for Power Inverters," 18th International Symposium "TOPICAL PROBLEMS IN THE FIELD OF ELECTRICAL AND POWER ENGINEERING," 14-19 January, Toila, Estonia, 2019 (oral).

Papers under review circulation or revision:

1. A. G. Paspatis, G. C. Konstantopoulos and S. Dedeoglu, "Control Design and Small-Signal Stability Analysis of Inverter-Based Microgrids with Inherent Current Limitation under Extreme Load Conditions ," Under review (Journal paper).
2. S. Dedeoglu, G. C. Konstantopoulos and A. G. Paspatis, "Grid-Supporting Three-Phase Inverters with Inherent RMS Current Limitation Under Grid Faults," Under review (Journal paper).